UNIVERSITÀ DEGLI STUDI DI TRIESTE

XXIX CICLO DEL DOTTORATO DI RICERCA IN

Scienze della terra e meccanica dei fluidi

TITOLO DELLA TESI

"Earthquake Transients and Mechanics of Active Deformation: Case Studies from Pakistan and Italy."

Settore scientifico-disciplinare:

GEO/10 GEOFISICA DELLA TERRA SOLIDA

DOTTORANDO: Farhan Javed

COORDINATORE: Prof. Pierpaolo Omari

SUPERVISORE DI TESI: Prof. Abdelkrim Aoudia

ANNO ACCADEMICO 2015/2016

Abstract

The understanding of the dynamics of the lithosphere and dominant physical processes during the earthquake cycle is important to estimate the seismic hazard of a given region. In the present study, we rely on seismology to image the geometry of both lithosphere and seismogenic faults and on geodesy to quantify the surface deformation and then we model the time-dependent dynamics of the coupled lithosphere-fault system.

In the first part of the work, we study two earthquake transients, in which, one lasts for a few years following the 2005 Mw 7.6 Kashmir's earthquake and the second exhibits deformation for a couple of weeks before the 2009 Mw 6.3 L' Aquila earthquake in the central Apennines, and model the long term inter-seismic deformation across the Idrija fault in the Dinarides (Western Slovenia). In this part of work, we report on the dominant physical process during different phases of the earthquake cycle, namely the postseismic and preseismic phases.

In the second part of the work, we investigate the temporal change of stress state over the Dinarides and Eastern Alps through the coseismic stress changes induced by earthquakes in this region, together with the related post-seismic and interseismic changes due to relaxation processes and interseismic loading. In the last part of the work, we study the dynamics of a dense lithosphere over a weak asthenosphere beneath the Adria plate and model the present day crustal deformation in the peri-Adriatic region including the Apennines, the Alps and the Dinarides. The implications of these investigations stand in the understanding of how deformation at the plate boundary scale is transferred to active faults accounting also for transients in the system.

KeyWords: earthquake transient deformation, dynamics of lithosphere, stress evolution model, Interseismic deformation, finite element method, rate and state dependent frictional law

Publications:

1. **Javed, F**., Hainzl, S., Aoudia, A. et al., Modeling of Kashmir Aftershock Decay Based on Static Coulomb Stress Changes and Laboratory-Derived Rate-and-State Dependent Friction Law Pure Appl. Geophys. (2016) 173: 1559. doi:10.1007/s00024-015-1192-9.
2. Borghi, A. Aoudia, **F. Javed**, R. Barzaghi; Precursory slow-slip loaded the 2009 L'Aquila earthquake sequence. *Geophys J Int* 2016; 205 (2): 776-784. doi: 10.1093/gji/ggw046.

   In this context, (A.B, A.A and R.B) analyzed continuous Global Positioning System (GPS) time series, prior to the 2009 L'Aquila earthquake in search of any transient deformation. (F.J and A.A) compare evidence for a SSE from GPS data with seismological constraints and characterize the stress loading on the eventual rupture plane.
3. H.Wang, A. Aoudia, **F. Javed** and Ian Hamling, Modeling of Interseismic deformation across the Idrija fault system (Submitted Manuscript).

   In this paper, (H.W, A.A and I.H) analysed the descending and ascending interferogram tracks and produce the rate map across the Idrija fault system. They model the interseismic deformation assuming the infinite long vertical strike slip fault (Savage and Prescott, 1978). But this formulation is restricted to homogenous elastic medium. (F.J and A.A) contribute an asymmetrical modeling part in the paper, using finite element approach, which include the effect of dip and heterogeneities across the fault.
4. **F. Javed** and A. Aoudia, Time dependent stress evolution, after the occurrence of 1511 earthquake, at the junction between South-eastern Alps and western Slovenia (Manuscript in preparation).
5. H. Wang , J. Liu-Zeng , A. H.-M. Ng , L. Ge , **F. Javed** , F. Long , A. Aoudia , J. Feng and Z. Shao, Sentinel-1 observations of the 2016 Menyuan earthquake: a 2 buried reverse

event linked to the left-lateral Haiyuan fault, Int. J. Appl. Earth Obs. Geoinf (Article in Press).

Table of Contents

Chapter 1: Introduction

A seismic cycle is a time dependent process, which consists of different periods. The term “cycle” does not imply that it is regularly repeating in time, but means that earthquakes repeatedly rupture a certain portion of the fault. The seismic cycle can be divided into three phases, consisting of co-seismic, post-seismic and inter-seismic phases. Understanding dominant physical processes for each phase is of importance in assessing the seismic hazard. For example, large earthquakes and transient during the earthquake cycle alter the stress in the surrounding crust, leading to triggered earthquakes and aftershocks (Nur et al., 1972; Dieterich 1994; Harris et al., 1995; Freed et al., 1999). But still the seismic hazard assessment in continents is challenging for a couple of reasons. Firstly, we need to understand the increase in seismicity in the stress decreased region, following large earthquakes. For example, Parsons et al. (2012) observed the significant increase in seismicity in the stress shadow region, following the 2005 Mw 7.6 Kashmir’s earthquake. The authors test the secondary triggering mechanism to model the seismicity in that region, but this explains only partial aftershock activity. Secondly, we need to understand the physical mechanism that stands behind the occurrence of small magnitude earthquake sequences and their interaction with the active faults in the region in terms of seismogenic potential. For example, foreshock sequences observed in central Italy in the early 2009 and their relationship with the occurrence of the subsequent destructive earthquake in L’Aquila. Several researchers identified both repeating earthquakes in this foreshock sequence and migration of seismicity towards the hypocenter of 2009 Mw 6.3 earthquake (Valoroso et al., 2013; Sugan et al., 2014). Similarly, Vičič et al. (2017) reported the increase in seismicity during the early 2010 in the Idrija fault system, but that did not lead to a sizeable earthquake eventhough the region is in deficit of earthquakes. For example, the faults that caused the 2003 M6.5 Bam (Iran) and 2010 M7.0 Darfield (New Zealand) earthquakes could not have been identified before they ruptured the surface and this due to active sedimentation, which prevents measuring any long term deformation (Jackson et al., 2001; Wright et al., 2016). Lastly, an active deformation zone comprises many faults and particularly in areas where earthquakes are few in number with not well documented historical earthquakes. For

example, sources of Mw 6+ earthquakes in Dinarides and Eastern Alps, based on seismological and geological evidence (Burrato et al., 2008), did not report the recently discovered maximum displacement of the order of approximately 1.7m on the Rasa fault in a Dinarides (Foroutan et al., 2017). Further to a pertinent knowledge of the mechanics of the fault system and how the loading is distributed within the deformation zone, a understanding of the dynamics of the lithosphere contributes to a physics-based seismic hazard assessment. A realistic modeling of the tectonic stresses and their distribution and assessing the dominant forces which drive the plate/microplate motion are important ingredients to decipher the stress evolution of a fault system.

1.1 Main Objective of the Thesis and roadmap of the work

The research work presented in this thesis is divided in to three parts. In the first part of the work, we address the following question: how the incorporation of physical processes improve the stress interaction modeling through case studies of 2005 Mw 7.6 Kashmir aftershock sequence and 2009 Mw 6.3 L' Aquila earthquake foreshock, main shock and aftershock sequences. The former case study demonstrates the role of stress heterogeneities produced by a large earthquake and their impact on distribution of aftershocks in space and time. In this work, we also evaluate the effect of secondary triggering on the stress heterogeneities. While in the latter case study, we first analysed the foreshocks sequence prior to 2009 Mw 6.3 earthquake. During 12th February- 26th February, Borghi et al. (2016) detected a transient preseismic deformation in the form of geodetic measurements prior to the 2009 Mw 6.3 L'Aquila earthquake. In this study, we report on the existence of a decollement beneath both L'Aquila and Campotosto faults acting as mechanical discontinuity. We show that such a decollement produced a slow slip event (SSE) and at the same time accommodates miscroseismicity as reported by Valoroso et al. (2013). We also evaluate the importance of stress loading on the mainshock during the detectable pre-seismic phase and foreshock sequence and how it controls the 2009 Mw 6.3 mainshock-aftershocks distribution. The detailed description and methodology of the case studies are presented in chapter 2 and 3.

Previous studies mapped the active faults at the junction between the Southeastern Alps and external Dinarides and also documented the historical earthquakes in the region (Aoudia, 1998;

Aoudia et al., 2000; Bajc et al., 2001; Fitzko et al; 2005, Borghi et al., 2009). The slip histories and post-seismic transients of the earthquakes in northeastern Italy and western Slovenia are well modeled (Borghi et al., 2009). Wang et al. (2017) constructed the rate map across the Idrija fault system. A profile across the Idrija fault system depicts the pattern of an asymmetrical deformation. Vičič et al. (2017) reported approximately 12000 small earthquakes during 2006-2016. During the early 2010, a burst of seismic activity observed at 15 km depth on the Predjama fault. In this work, we first model the asymmetrical behavior of the interseismic velocities across the Idrija fault system and then quantify the role of unclamping on the Idrija fault system and how it consistent with the spatial distribution of small earthquakes during 2006-2016. The results are listed in chapter 4 and 5. In chapter 4, we demonstrated that the Idrija fault is locked up to 20km depth. Seismological evidence also shows that there is no seismicity along the shallow portion of the Idrija fault system. In the end, we consider all the historical large earthquakes including the recently discovered earthquake on the Rasa fault and then compute the stress evolution of an interacting fault system at the junction between the southeastern Alps and external Dinarides accounting for the deformation during the complete earthquake cycle and related transients. We discuss the implications on the earthquake hazard in northeastern Italy and western Slovenia (See chapter 5).

The last part of the work deals with the spatial variation of density (buoyancy forces) in the lithosphere-asthenosphere structure and discusses the present day surface deformation in the study region. We mainly address the following questions:

1. How buoyancy forces contribute to dynamics of Adria plate and neighboring belts?
2. What is the effect of these forces in term of distinct tectonics features in the region?

Pylith- the finite element code is used to address these questions by taking in to account the effect of density and viscosity variation within the lithosphere and the results are presented in chapter 6.

.

Chapter 2: Mechanics of the post-seismic transient: The 2005 Mw 7.6 Kashmir and physics of the aftershock sequence

We model the spatial and temporal evolution of October 8, 2005 Kashmir earthquake's aftershock activity using the rate and state dependent friction model incorporating uncertainties in computed coseismic stress perturbations. We estimated the best possible value for frictional resistance "$A\sigma_n$", background seismicity rate "r" and coefficient of stress variation "CV" using maximum log-likelihood method. For the whole Kashmir earthquake sequence, we measure a frictional resistance $A\sigma_n$ ~ 0.0185 MPa, r ~ 20 M3.7+ events/year and CV= 0.94±0.01. The spatial and temporal forecasted seismicity rate of modeled aftershocks fits well with the spatial and temporal distribution of observed aftershocks that occurred in the regions with positive static stress changes as well as in the apparent stress shadow region. To quantify the effect of secondary aftershock triggering, we have re-run the estimations for 100 stochastically declustered catalogs showing that the effect of aftershock-induced secondary stress changes are obviously minor compared to the overall uncertainties, and that the stress variability related to uncertain slip model inversions and receiver mechanisms remains the major factor to provide a reasonable data fit.

2.1 Introduction

It is well known that major shallow earthquakes are followed by increased seismic activity, known as 'aftershocks', which last for several days to several years. The temporal decay of this aftershock activity usually follows the Omori-Utsu law and the spatial distribution can be roughly modeled by static Coulomb failure stress changes (ΔCFS). As pointed out in previous studies of mainshock-aftershock sequences in different tectonic environments, seismicity models only based on ΔCFS fail to explain the observed activation in regions where stress was apparently decreased by the mainshock (Hainzl et al., 2009; Parsons et al., 2012). However, several possible mechanisms might explain the occurrence of aftershocks in those stress shadows, e.g. dynamic stresses,

secondary triggering and stress uncertainties. In particular, intrinsic variability and uncertainty of calculated stress values are shown to explain aftershock activation in regions with a negative average stress change, if laboratory-derived rate- and state-dependent friction laws are considered (Helmstetter and Shaw, 2006; Marsan 2006; Hainzl et al., 2009). We further explore this possibility by the analysis of the Mw7.6 Kashmir mainshock which occurred on 8th October, 2005 in northern Pakistan and was followed by an intense aftershock activity. In the case of Kashmir's earthquake sequence, 30% aftershocks with magnitude ranging from 3.5 to 5.5 were occurring in the stress shadow region (see figure 2.5). Parsons et al. (2012) included the uncertainties related to small scale slip variability, which is also a part of the overall uncertainties, defined by Coefficient of stress variation (CV) in our study. They analyzed the spatial aftershock locations in relation to the static CFS changes, and concluded that this will explain the occurrence of aftershocks and spatial variability near the mainshock. However, they also demonstrated that it does not affect the overall regional stress change pattern, even using different values of coefficient of friction and orientation of regional stress field. They found that half of the events that occurred in the stress shadow southwest of the mainshock can be explained by aftershock triggering, while the rest of them are ascribed to the mainshock and remained therefore unexplained. However, other factors such as the uncertainty of the mainshock source model and the receiver fault orientations are likely to dominate the overall uncertainty and variability (Cattania et al. 2014). Therefore, we compare the observed aftershock pattern with the spatiotemporal seismicity patterns predicted by the Coulomb rate- and state-dependent friction (CRS) model under consideration of involved dominant uncertainties (CV). As shown by Parsons et al. (2012), secondary triggering seems to play a role in generating the aftershocks particularly southwest of the mainshock. In this chapter, we will thus address in particular the two questions:

1) Whether the occurrence of aftershocks in stress decreased region can be explained by uncertainties of the calculated static stress changes (CV-value)?

2) How much of the stress variability can be attributed to secondary triggering?

To discuss the second point, we remove secondary aftershocks, which are obviously triggered by other aftershocks, by applying the epidemic type aftershock sequence (ETAS) model. We analyse

the model forecasts for the original catalog as well as stochastically declustered catalogs in order to evaluate the model fits and the role of secondary triggering.

2.2 Seismicity Model

The underlying physical model that has been utilized in this study to determine the aftershock decay rate is based on laboratory-derived rate-and-state dependent friction laws (Dieterich, 1994; Dieterich et al., 2000). This model incorporates the stress perturbations induced by earthquakes and the physical constitutive properties of the faults (Dieterich, 1994). The model parameters are, besides the background seismicity rate r, the frictional resistance $A\sigma_n$, and the relaxation time for the aftershocks t_a (or alternatively, the tectonic stressing rate $\dot{S}$)

Based on laboratory-derived rate-and state-dependent friction laws, the earthquake rate R for a population of faults is given by (Dieterich, 1994)

$$R = \frac{r}{\gamma \dot{S}} \qquad (2.1)$$

where γ is a state variable governed by the equation

$$d\gamma = \frac{1}{A\sigma_n}(dt - \gamma ds) \qquad (2.2)$$

Here σ_n is the effective normal stress and A is a dimensionless fault constitutive friction parameter (Dieterich, 1994; Dieterich et al., 2000). Based on this evolution equation, the time-dependence can be explicitly calculated for stress histories consisting of coseismic stress steps and constant tectonic loading. In particular, the seismicity rate after a stress step ΔS at time t = 0 is given by (Dieterich, 1994)

$$R(t) = \frac{1}{\left[1+\left(exp\left(^{-\Delta S}/_{A\sigma_n}\right)-1\right)exp\left(^{-t}/_{t_a}\right)\right]} \qquad (2.3)$$

assuming the same constant tectonic stressing rate $\dot{S}$ before and after the mainshock. This takes the form of Omori-Utsu's law, $R(t) \sim (c+t)^{-p}$, with p=1 for $t << t_a$, where the aftershock relaxation time t_a is related to the stressing rate by $t_a = {}^{A\sigma_n}/_{\dot{S}}$. Figure 2.1 shows the correlation

between the different parameters of rate and state model. It demonstrates that the same decay rate is observed for different combination of input parameters.

2.3 Static Coulomb Stress Changes

The locally predicted seismicity rate depends on the calculated stress change ΔS in the seismogenic volume under consideration. The approach which is here adopted has been previously proposed by various scientists (King et al., 1992; Reasenberg and Simpson, 1992; Harris and Simpson, 1992; Stein and Lisowski, 1983 and Stein et al., 1981). It is based on the Coulomb failure stress that involves both normal and shear stresses on the specified target faults or optimally oriented fault planes. The decisive parameter is the Coulomb Failure Stress (CFS), which is defined as

$$\Delta CFS = \Delta\tau + \mu\,(\Delta\sigma n + \Delta p), \qquad (2.4)$$

where $\Delta\tau$ and $\Delta\sigma_n$ are shear and normal stress changes, Δp is the pore pressure change and μ is the coefficient of friction which ranges from 0.6 to 0.8 for most rocks (Harris, 1998). Pore pressure modifies the co-seismic stress redistribution and for that reason they are included in the basic definition of Coulomb failure function. According to Rice and Cleary (1976), the pore pressure is related to the mean stress by Skempton coefficient B under undrained condition, $\Delta p = -B\Delta\sigma_{kk}/3$, where the Skempton coefficient can vary between 0 to 1. Alternatively, it is often assumed that for plausible fault zone rheologies, the change in pore pressure becomes proportional to normal stress on faults, $\Delta p = -B\Delta\sigma_n$ (King et al., 1992; Stein and Lisowski, 1983 and Stein et al., 1981). Substituting this relation in Eq. (2.4) leads to

$$\Delta CFS = \Delta\tau + \mu'\Delta\sigma_n\,, \qquad (2.5)$$

with $\mu' = \mu(1-B)$ being an effective friction coefficient. Stein & Lisowski (1983) and Stein et al. (1981) have used the value $\mu' = 0.4$ in many calculations, which we also adopt in our study.

To calculate ΔCFS, also the receiver mechanisms have to be defined. Two assumptions are commonly used in this context: a) fixed fault geometry and b) optimally oriented fault plane

geometry. While in the former case, focal mechanisms (i.e. strike, dip and rake) of the aftershocks are assumed to be known by e.g. well documented faults, a theoretical focal mechanism is calculated in the latter case, which is assumed to be optimal oriented to the total stress field consisting of the regional background stress and mainshock induced ΔCFS change. We follow here the latter approach, where the magnitude and orientation of the regional stress field are taken from Parsons et al. (2006).

2.4 Approximation of Uncertainties

Stress calculations are known to be subject to large uncertainties, which have to be considered in order to get reliable model fits (Hainzl et al., 2009, 2010b; Woessner et al., 2012). If the involved uncertainties and variabilities related to earthquake slip, receiver fault orientations, and crustal properties are ignored, the estimation of the model parameters is biased, and apparent stress shadow regions are expected which do not occur if intrinsic variability is considered (Hainzl et al., 2009; Helmstetter and Shaw, 2006; Marsan, 2006).

Three slip models were published in the literature so far, for October 8, 2005 earthquake. These slip models were determined by Parsons et al. (2006), Avouac et al. (2006) and Pathier et al. (2006). The first slip models were estimated from seismological data, while the last two were inverted from geodetic measurements. We use the analytic solutions of Okada (1992) for the elastic half space to calculate ΔCFS at grid points for all three slip models assuming a shear modulus of 30 GPa.

The results are shown in figure 2.3. All three slip model depict the stable stress decreased region as expected (Hainzl et al., 2009; Helmstetter and Shaw, 2006; Marsan, 2006) and also mentioned by Parsons et al. (2012). We use the mean ΔCFS value as a best estimate of the stress value at each location. The variability of the three estimated ΔCFS values represents roughly the epistemic uncertainty, is included as a part of the considered uncertainties in our analysis.

Different types of uncertainties are also associated with the stress change:

i) Local stresses vary with the crustal heterogeneity influencing the seismicity rate. Morevoer the pre-stress state influences the receiver mechanisms and geometry, and thus effects the stress

perturbations, ii) Lack of knowledge of the geometry of receiver faults at depth (Hainzl et al., 2010b), iii) The direction and amplitude of regional stress field (Hardebeck and Hauksson, 2001), iv) Incalculable small scale slip variability close to the fault which cannot be directly resolved by inversion of surface data (Helmstetter et al., 2006; Marsan 2006), and v) No uniqueness of the slip model inversions (Steacy et al., 2004).

Most of above mentioned uncertainties cannot be simply quantified in models due to lack of knowledge, while other uncertainties e.g. in the slip model can be taken directly into account, if related information are available (Woessner et al., 2012). However, the variability of the stress field, which results from the general uncertainties in slip inversions (Hartzell et al., 2007) and regional stress field (Hardebeck and Hauksson, 2001), can be taken into account in the model using simplified Gaussian distributed probability density function (Hainzl et al., 2009). All the parameters used for the estimation of stress variability are listed in Table 2A. Hainzl et al., (2009) also demonstrated that the variability of the stress estimation is, in a first approximation, linearly correlated to the value of the absolute mean stress change, indicating that the coefficient of variation $CV = \delta / abs\,(\Delta CFS)$ is approximately constant in space. Thus the CV-value is an effective parameter accounting not only for the slip model variation, but also the variability of receiver mechanisms, material parameters, stress heterogeneities, etc.

Figure 2.4a shows the stress variation is of the order of mean Coulomb stress change, which is the result of uncertainties related to different slip models and receiver fault mechanism(strike=330, dip=30, and rake=90) variations with standard deviation(20 degrees, 10 degrees and 10 degrees respectively) in the model. We also plot the stress variation corresponding to each mean stress change at the hypocenters of the aftershocks as shown in figure 2.4b. These results indicate that our assumption of a linear relation between the standard deviation and the absolute value of stress change is a reasonable first order approximation. To account for these uncertainties in the rate-and-state dependent friction model, a Gaussian distribution is assumed with the mean value being the average stress value of the different slip models and the standard deviation is the product of CV and absolute value of mean ΔCFS. The observations are compared to a number N of Monte-Carlo simulations, where the stress in each sub volume is taken randomly (in our case, we

consider M7.6 Kashmir earthquake, with N=250 realizations of the stress jump) from the Gaussian distribution.

2.5 Model Parameter

The rate-and-state dependent frictional nucleation model depends on the three parameters r, $A\sigma_n$ and t_a. It is very sensitive to background seismicity rate r, which is the rate of earthquakes in the absence of any stress perturbation. In general, the background activity is expected to be non-uniform due to rheological inhomogeneities of the crust. The model assumes that the state variable is at a steady state before the application of a stress perturbation, which means that it does not change with time (Dieterich 1994; Dieterich et al., 2000; Cocco et al., 2010; Hainzl et al., 2009; Hainzl et al., 2010). Indeed, it is assumed that this initial γ-value is equal to the inverse of the tectonic stressing rate. According to Eq. (2.1), the seismicity rate before the application of the stress perturbation is thus equal to the background rate r, associated with a temporally stationary process, which can be in principle estimated from declustered catalogs (Stiphout et al., 2010). Jouanne et al. (2011) estimated the background seismicity rate in the Kashmir region as 0.08 M3.5+ events/day. In many studies and applications of rate and state dependent model (Cocco et al., 2010; Hainzl et al., 2009; Toda and Stein, 2003), the background seismicity rate is assumed to be spatially uniform, because of the lack of sufficient data to estimate spatial variations. Although the background activity is likely inhomogeneous in reality, the estimation of its spatial variation from few historic events is difficult and would potentially introduce additional uncertainties. Thus we follow the previous approach and assume a spatially uniform background rate. In our case, the value of r is not fixed but estimated from data fitting using the maximum likelihood fit (see section 2.8). However, we will see that our result is in good agreement with the previous estimation of Jouanne et al. (2011). Furthermore, it should be noted that the value of r estimated from the non-declustered catalog contains not only the background events (i.e. definition of background rate in the strict ETAS sense) but also their triggered aftershocks, so the background rate in this case refer to the time independent smoothed seismicity rate computed from the non-declustered catalog (Catalli et al., 2008; Cocco et al., 2010).

The second important parameter in the rate-and-state dependent friction model is the frictional resistance $A\sigma_n$. While the dimensionless fault constitutive friction parameter A is approximately known from laboratory experiments to be ~0.01 (Dieterich 1994; Dieterich et al., 2000), the absolute value of the effective normal stress σn is mostly unknown. It is likely to depend on depth, regional tectonic stress, fault orientation, and pore pressure (Cocco et al., 2010; Hainzl et al., 2010). For simplicity, we assumed that $A\sigma_n$ is uniform over large volumes and estimated the value of $A\sigma_n$ by data fitting. Previous applications of this model indicated values of $A\sigma_n$ in a range between 0.01 and 0.2 MPa (Cocco et al., 2010; Hainzl et al., 2010).

The third parameter in the rate-and-state dependent constitutive frictional law is the tectonic loading rate $\dot{S}$. Alternatively, one can use the relaxation time t_a which determines the duration of the aftershock activity (Hainzl et al., 2010). This parameter is not well constrained from earthquake data as long as the aftershock decay is ongoing. Therefore, t_a is also determined by the maximization of the likelihood value for the observed Kashmir aftershock sequence.

2.6 Aftershock Data

We analyzed the aftershock events, from the International Seismological Centre (ISC catalog), that occurred between 330N and 360N latitude and 720E and 750E longitude (see Fig. 2.2a). We first selected aftershocks of magnitude ≥ 3 that occurred between the period 2005-10-08 and 2013-10-15 in the study area. According to Parsons et al. (2012), the minimum magnitude of completeness varies from 3.7 to 4.0 for the Kashmir aftershocks in the NEIC earthquake catalog as well as in the ISC catalog for the above defined study area (see Fig. 2.2b). We thus selected aftershocks of magnitude ≥ 3.7 for our analysis. However, we neglected aftershocks that occurred within the first 12 hours after the Kashmir earthquake to account for likely incomplete catalog recordings in the first time interval (Kagan, 2004). A total number of 693 events were recorded in the analyzed time and space interval. Other information related to semi major, semi minor axes and orientation of the error ellipsoid are given in the catalogs. In our analysis, we used this information to account for the location uncertainties.

2.7 Stochastic Declustering

It has been recognized that sub-clustering observed in aftershock sequences might be the result of aftershock-aftershock triggering (e.g. Ogata 1988 and Ogata 1992). We want to address the question of whether the corresponding aftershock-induced stress variations significantly contribute to the overall stress uncertainties. For that, we analyze the declustered aftershock sequence to focus only on aftershocks directly related to the mainshock. Several methods have been proposed for declustering a catalog (e.g. Gardner and Knopoff 1974; Zhuang et al., 2002; Zhuang et al., 2004) We apply the stochastic declustering methodology introduced by Zhuang et al. (2002) to obtain the aftershocks directly linked to the mainshock. The method is based on the empirical ETAS model described by

$$R(t) = \mu + \sum_{t_i}^{t} K 10^{\alpha(M-M_c)} (c + t - t_i)^{-p} f(r)$$

where parameters c and p are related to the Omori-Utsu law and K and α to the empirical productivity law (Utsu 1961), while μ is the background rate and f(r) is the normalized isotropic kernel

$$f(r) = \left({}^{q}/_{\pi}\right) {}^{d^{2q}}\Big/_{(d^2 + r^2)^{(1+q)}}$$

In the case of the mainshock, the spatial kernel is calculated by the normalized sum of f(r) for a large number of point-sources with a spacing of 1 km at the rupture plane (to account for the extension of the rupture). The parameters of f(r) have been set to the reasonable value q=0.5 (which corresponds to a r^{-3} decay in agreement with the static stress decay in the far field) and d=10 km as an approximation of the location error. To obtain stochastically declustered catalogs, we firstly estimated the ETAS parameters by a maximum likelihood fit of the M≥3.7 aftershocks within [0.5 1000] days (where preceding events are used to calculate the rate within this time interval) which yields: μ=0.013 [events/day], K=0.014, c=0.048 [day], α=1.07 and p=1.19. Then single declustered catalogs were constructed by selecting randomly events according to their probability to be not triggered by another aftershock. In this way, we have created 100 stochastically declustered catalogs based on the parameters estimated by the ETAS model fit.

2.8 Parameter Estimation Approach

The applied forecasting model consists of four free parameters: t_a, $A\sigma_n$, r, and CV. All these parameters are assumed to be constant in space and inverted from the data (i.e. ΔCFS values and aftershock data). Mean ΔCFS values were calculated for 15 different layers within 1 and 15 km depth and on a horizontal grid with spacing of 5km. As an example, figure 2.5 shows the determined stress changes at 10 km depth. We adopted the maximum likelihood method (Ogata, 1998; Daley and Vere-Jones, 2003) to fit the data. The characteristic time scale t_a for the aftershock relaxation is poorly constrained by the aftershock data, because of the ongoing aftershock decay. Our estimation of the relaxation time t_a yields a broad likelihood maximum between 40 and 70 years. To reduce the parameter space, we therefore fixed the aftershock duration time to the value of t_a = 25000 days or 65.4 years. We performed a grid search in the intervals $A\sigma_n \in [0.01, 0.2]$ MPa and CV ϵ [0.5, 1.5] to find the best fitting values for the remaining parameters $A\sigma_n$ and CV using the maximum likelihood method. For a given time interval $[t_0,t_1]$ and spatial volume $[x_0, x_1] \times [y_0, y_1] \times [z_0, z_1]$, the log-likelihood function with respect to N earthquakes that occurred at times t_i and location $\vec{x}_i$ can be defined by:

$$\ln L = \sum_{i=1}^{N} \ln R(\vec{x}_i, t_i) - \left[\int_{t_0}^{t_1} \int_{z_0}^{z_1} \int_{y_0}^{y_1} \int_{x_0}^{x_1} R(x, y, z, t)\, dxdydzdt \right]$$

(Ogata 1998; Daley and Vere-Jones 2003).

For given $A\sigma_n$ and CV, the r-value which optimizes the log-likelihood value LLmax is analytically determined by setting the derivative of the log-likelihood function with respect to r equal to zero (Hainzl et al., 2009).

$$r = N \left[\int_{t_0}^{t_1} \int_{z_0}^{z_1} \int_{y_0}^{y_1} \int_{x_0}^{x_1} \frac{R(x, y, z, t)}{r} dxdydzdt \right]^{-1}$$

In order to account the uncertainties in the calculated parameters ($A\sigma_n,\ CV\ and\ r$), we assume that the error in each parameter is normally distributed about its mean. We define the error bounds by the minimum and maximum parameter values yielding a log-likelihood value LL=LLmax-0.5, which corresponds to plus/minus one standard deviation in the case of a normal distribution.

To find these error bounds, we set the parameters to their optimal values and started to successively decrease or increase the parameter value by a small increment until the LL-value of the fit with optimized remaining parameters equaled LL=LLmax-0.5.

We evaluate the role of grid spacing in terms of model parameter estimation and found those estimated parameters are stable under sub-gridding. The results are shown in table 2.1. Our standard choice for the parameter estimation is the time window from 0.5 to 1000 days. However, the model parameters are also estimated for two smaller time windows: [0.5, 2.5] and [0.5, 10] days to check the consistency and robustness of the result. Because of the loosely constrained value of t_a, we also repeat the estimations with t_a~48 years. The results are shown in the table 2.2. A correlation between the background rate r and t_a is observed because for a fit on short times, $r^* t_a$ only is constrained and thus for smaller t_a, the estimate of r becomes larger (see Fig. 2.1).

2.9. Results for the Kashmir Aftershock Sequence

The results for the parameter estimation in the case of the Kashmir's aftershock sequence are shown in table 2.2. All parameters were found to be already quite well constrained by the early aftershocks and remain rather stable for estimations based on much longer time intervals. Furthermore, the inverted parameter values are reasonable and very close to previous estimations. Our estimated background rate is 0.055 ± 0.002 per day for M≥3.7 which is close to the estimation of Jouanne et al. (2011) estimated for M≥3.5 (their result of 0.08 per day corresponds to $0.08\ 10^{-0.2b} \approx 0.047$ M≥3.7 events per day assuming b=1.15). The estimated value of $A\sigma_n$ = 0.0185 ± 0.001 MPa is in the same order as estimations for different earthquake sequences (Toda et al., 1998; Catalli et al., 2008; Hainzl et al., 2009). In order to compare the models result with and without stress variability, we use the Akaike Information Criterion (AIC), which is defined by

$$AIC = -2\,(L) + 2K$$

Where K is the number of free parameters and L is the maximize value of the log-likelihood function for the model. A preferred model is the one with the minimum AIC value.

Note that the model accounting for stress variability significantly improves the fit which is shown by the difference between the values of the ΔAIC = -2 [LL(CV=0) – LL] - 2, provided in table 2.2.

Using the inverted parameters, we analyze the aftershock sequence of Kashmir's mainshock in more detail. According to Parsons et al. (2012), the static stress model fails to forecast the spatial distribution of those aftershocks which occurred in the stress shadow region (i.e., in the region, where the calculated stress change induced by the major event was negative). To investigate this point, we separate the aftershock activity in two different regions which experienced significant positive and negative stress changes due to the Kashmir event:

1. All subvolumes where the calculated stresses are positive and greater than 0.01 MPa.
2. All subvolumes where the calculated stresses are negative and less than -0.01 MPa.

The total number of aftershocks occurred in the stress shadow region are approximately two third of the aftershocks occurred in the region with increased stress. However, both volumes have different spatial size. The observed aftershock densities in these regions are plotted in figure 2.6 (bold lines) as a function of time. It shows that the aftershock density is significantly higher in the stressed regions than in the stress shadows. A clear Omori law decay of the aftershock activity is observed not only in the loaded regions but also in the stress shadow regions as previously observed by Mallman and Zoback (2007), indicating that activation rather than quiescence occurred. This seems to contradict the static stress-triggering hypothesis, but only if the variability of the stress calculation is ignored.

We used the inverted values $A\sigma_n$ = 0.0185 MPa, r = 0.055 (events per day), t_a = 25000 days to calculate the aftershock density with (CV = 0.94; Fig. 2.6a) and without stress field variability (CV = 0; Fig. 2.6b) in the rate-and-state model. Figure 2.6b shows that the estimated aftershocks decay in the regions with the highest stress increase can be well described by the model without accounting for stress field variability, but the same model completely fails for the stress shadows in agreement with the previous result based solely on static stress patterns (Parsons et al., 2012). On the other hand, after accounting for stress variability, the model fits all regions equally well. As

already mentioned above, the model is also self-consistent in a way that the parameter estimations are robust for different time intervals also suggests that secondary triggering does not effect on the estimation of CV. We have found that parameters which have been inverted for the first days of the aftershock are able to reproduce the aftershock decay also on longer time scales in stress shadows as well as in regions of stress concentration. However, as shown in figure 2.6, the model tends to overestimate the seismicity rate in the later stage in the region that experienced positive stress changes, while it slightly underestimates the seismicity rate in the approximately first 10 days in the region that experienced negative stress changes.

Figure 2.7 shows the spatial distribution of the forecasted earthquake rates calculated from the seismicity model. The model fail to predict the aftershocks in the region x [-60 km, -40 km] and y [-10 km, 20 km] due to occurrence of largest aftershock of magnitude Mw 6.4 at the location [-35km, 20km].This largest aftershock occurred within a twelve hours after the mainshock and redistributes the stress in its vicinity. We didn't account the effect of stress induced by the aftershocks in our analysis. These maps have been calculated by integrating the forecasted earthquake rates over the first 9.5 days for the models with CV = 0.94 and CV = 0 respectively. The comparison with the epicenters of the M ≥ 3.7 aftershocks recorded in the same time period shows that the consideration of stress variability can explain the activation of earthquake in the apparent stress shadows. We further extend our analysis to test whether the estimated model parameters, particularly CV, are biased by secondary triggering, which is supposed to play an important role as pointed out by Parsons et al. (2012). We run the simulation for the case of declustered catalogs considering the time interval [0.5 10] days. The resulting model parameters for 100 declustered aftershock catalogs are shown in the table 2.2. Results depict that parameter estimations are affected by secondary aftershock clustering. As examples for declustered catalogs leading to CV=0.9 and CV=1.3, we plot the stress variation versus mean stress value at the hypocenter of direct aftershocks as shown in the figure 2.8. The inverted values of CV from both direct aftershocks catalogs are 0.9 and 1.3 which is close to the theoretical CV as shown by the bold lines. In summary, the estimated CV-values vary from 0.8 to 1.4 meaning that removing the secondary aftershocks slightly effect the estimation of CV, but its absolute value remains significant indicating that uncertainties related to slip model and receiver mechanisms are large.

As an example, figure 2.9 and 2.10 are shown the aftershocks density in both stress increases and decreased region and spatial distribution of the forecasted earthquake rates for the case of stochastically declustered catalogs. The comparison of the model results with the observations, showing several patterns of remaining earthquakes after the declustering show that the model fit the observed data quite well.

2.10 Discussion

Rate-and-state dependent seismicity models, which incorporate only deterministic Coulomb failure stresses computed for a particular choice of model parameters and prescribed faulting mechanisms or optimally oriented fault planes, for instance, fail to predict the increased seismicity rate often observed in stress shadows (Catalli et al., 2008; Parsons et al., 2012). However, large uncertainties are associated with those stress calculations, which have to be taken into account (Hainzl et al., 2009). These uncertainties are due to weakly constrained slip distributions, receiver fault mechanisms and crustal structures. Thus accounting only for deterministic Coulomb failure stresses is not appropriate to analyze and forecast the spatiotemporal evolution of seismicity based on rate-and-state dependent frictional earthquake nucleation. According to Hainzl et al. (2009) and also shown in this chapter, the confidence intervals (standard deviation) of the calculated stress values are likely to be in the same order as of mean stress value at each location due to above mentioned uncertainties. The consideration of the broad probability distribution can explain the activation of earthquakes in the apparent stress shadow region (Helmstetter and Shaw, 2006; Marsan et al., 2006; Hainzl et al., 2009). For simplification, a Gaussian distributed probability density function defined by its mean and standard deviation is used to account for the variability of the stress field in the model. The use of the correlated uncertainties of finite-fault source models is preferable (Woessner et al., 2012), however, these information are usually not available. Anyway, uncertainties related to the slip model can only account for a part of the involved uncertainties. Thus the applied simple approach might be reasonable in our case. By accounting for the variability of stress field (CV-value), we tested whether the aftershock occurrence triggered by the M7.6 Kashmir event can be modeled by the static stress changes and rate- and state-dependent frictional earthquake nucleation. The analysis shows consistent estimations of parameters on

different time scales similar to the results of Hainzl et al. (2009) in the case of the 1992 Landers earthquake. Based on these parameters, the model is able to fit the spatiotemporal distribution of aftershocks. Furthermore, aftershocks can influence the local stress field significantly and thus lead to a non negligible number of secondary aftershocks (Ogata, 1998; Felzer et al., 2003) which might also explain apparent failures of the static stress-triggering model as pointed out by Parsons et al. (2012). Aftershock-related stress changes are partly contributing to the involved stress uncertainties incorporated in our model by the CV-value. To evaluate the contribution of aftershock-related stress changes in the estimation of CV-value, we have analyzed catalogs where secondary aftershocks are stochastically removed. Our analysis shows that role of secondary clustering seems to be negligible and other uncertainties e.g. related to slip model and receiver mechanisms, play a major role for this catalog. It is well known that the $A\sigma_n$-value together with r controls the instantaneous increase of seismicity rate: the smaller $A\sigma_n$ and/or the larger r, the larger are the seismicity rate changes (Cocco et al., 2010). Our results for the declustered catalogs show an increased $A\sigma_n$ value and a decreased r value consistent with the decrease of seismicity rate. However, it should be noted that ETAS-estimated value of the background rate is not well constrained because the background rate does not play a significant role in the fitting period [0.5 10] days, where direct and secondary triggering dominates. Furthermore, also the value estimated by the CRS model is not well constrained because of the correlation between the background value and the aftershock duration time t_a (Cocco et al. 2010). It is also noted that the CRS model underestimate the seismicity rates in the stress shadow region at shorter time period [0.5 10] days as shown in the figures 2.6 and 2.9. This might be the result of not having deterministic knowledge and ignoring dynamic stress triggering. However, the model explains the seismicity rate at longer time period [10 1000] days well. This is also indicated by Segou et al. (2013). It is important to note that a number of simplifications were made in this study, in particular, the background rate was assumed to be constant in space, because its estimation from limited catalog data can introduce large uncertainties which can lead to a worsening of the fit. This has been demonstrated for the Coulomb-Rate-State model by Cocco et al. (2010), but holds similarly for the ETAS model. However, in reality, the background rate is most likely variable in space as preexisting fault structures are associated with higher background rate than those regions without these features

(Toda and Stein, 2003; Zhuang et al., 2002; Toda et al., 2005). The estimated CV-value might thus also compensate some of the unresolvable spatial variability of background rates as well as $A\sigma_n$ and t_a parameters occurring in reality. Finally, it is important to note that the spatiotemporal distribution of aftershocks can be influenced by time dependent post-seismic processes such as induced fluid flow and afterslip (Cattania et al., 2015), which has been ignored in our study.

2.11 Conclusion

Seismicity models built on static Coulomb stress changes often fail to explain a large part of the aftershock activity. This might be explained by the large uncertainties associated with stress calculations and the nonlinear response of earthquake nucleation to stress changes. To explore this possibility for the specific aftershock sequence following the 2005 M7.6 Kashmir event, we applied the physics-based statistical model introduced by Dieterich (1994) which is built on the basis of static Coulomb stress changes and rate-and-state dependent friction laws to forecast the spatiotemporal distribution of the aftershock activity. We approximated stress uncertainties by Gaussian-distributed stress values, where the standard deviation is assumed to be equal to be CV times the absolute mean value of ΔCFS. The values of the different model parameters (i.e. $A\sigma_n$, r and CV) used in this model approach were estimated by maximum likelihood fitting to the data. The estimated value $A\sigma_n$=0.0185±0.001 MPa is in the range of previously observed values between 0.01 and 0.2 MPa for other aftershock sequences and the estimated value of the background seismicity rate is similar to the estimation by Jouanne et al. (2011). For the case of declustered catalogs, we found that estimated value of CV increases to 1.1±0.3 indicating that stress-changes induced by aftershocks contribute only a minor part to the overall uncertainties of the stress calculations which have to be considered in stress-based seismicity models. The consistency of the model is not only demonstrated by the reasonable parameter estimations, but also by the observation that the estimations are robust for different time intervals. Based on the inverted parameters, the model is found to explain most of the spatiotemporal seismicity patterns well, even the activation in apparent stress shadows. Thus our result indicates that stress heterogeneity plays an important role in the activation of aftershocks in the stress shadow region.

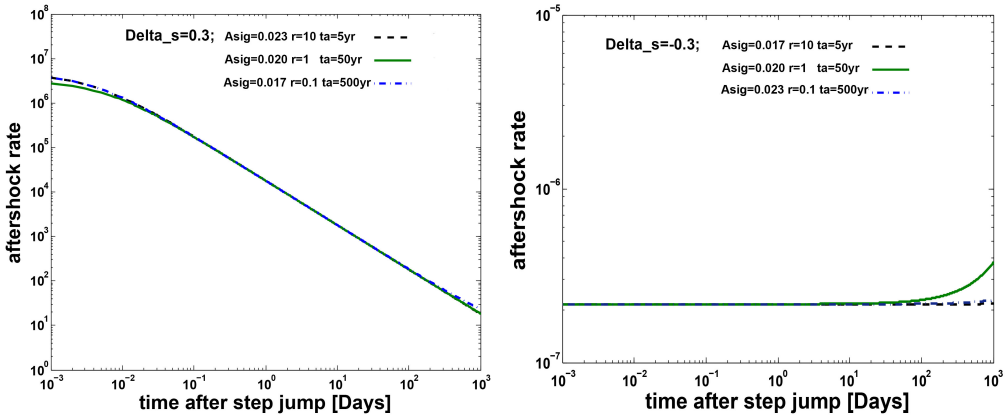

Figure 2.1: Rate of aftershock production in a log-log scale caused by (a) a positive and (b) a negative stress perturbations. Colours indicate different combinations of input parameters of the rate and state model. A same decay rate has been obtained from different combination of aftershock duration *ta*, background rate *r*, and $A\sigma_n$.

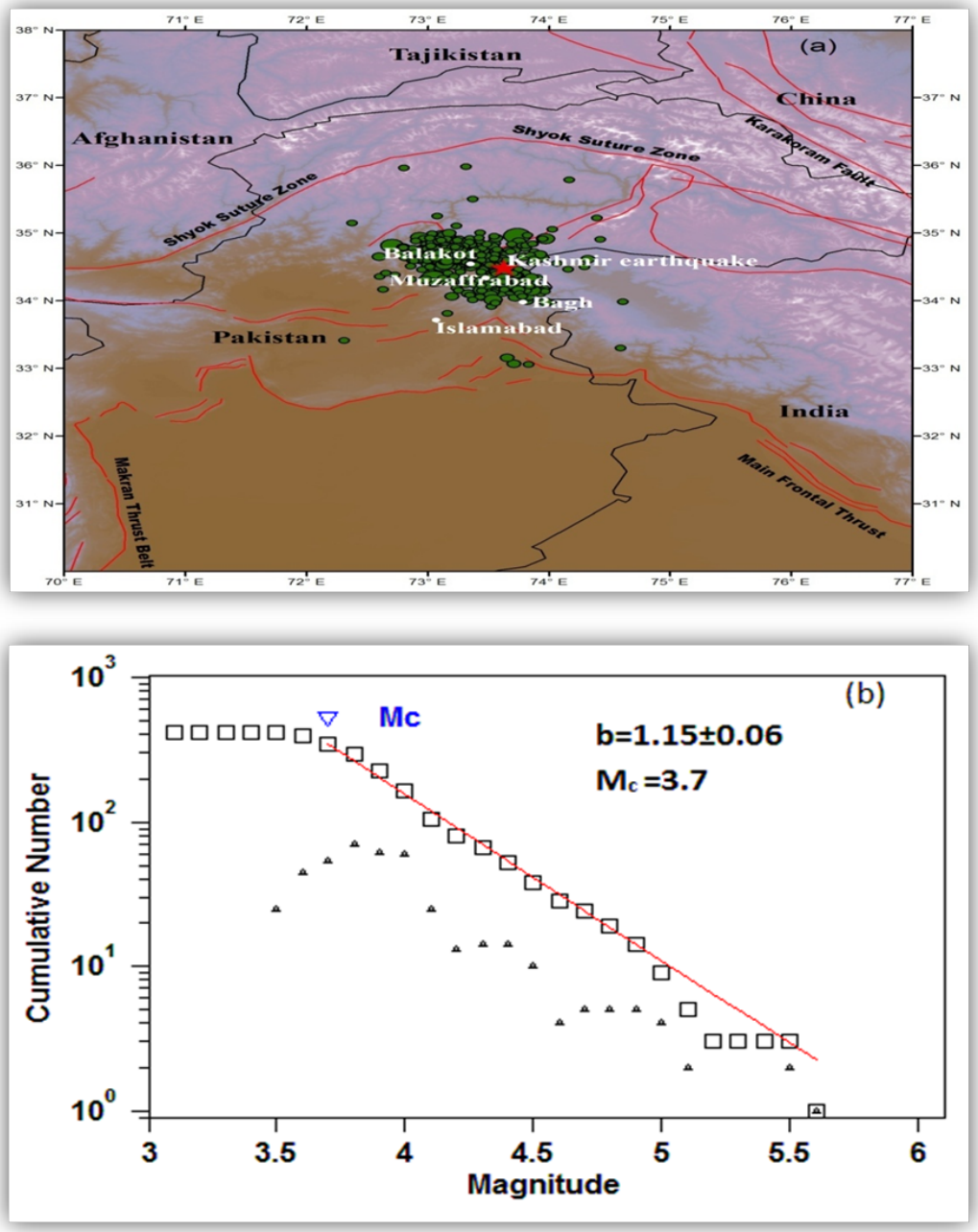

Figure 2.2: (a) Map shows the aftershocks of Oct 8, 2005 earthquake where the red star indicates the epicenter of the mainshock, (b) frequency-magnitude distribution (FMD) of aftershocks for t>0.5 days with b=1.15±0.06 and magnitude of completeness Mc=3.7. Triangles and squares represent the number and cumulative number of each individual magnitude level of earthquake, respectively. The line represents the FMD linear regression fitted with the observed data.

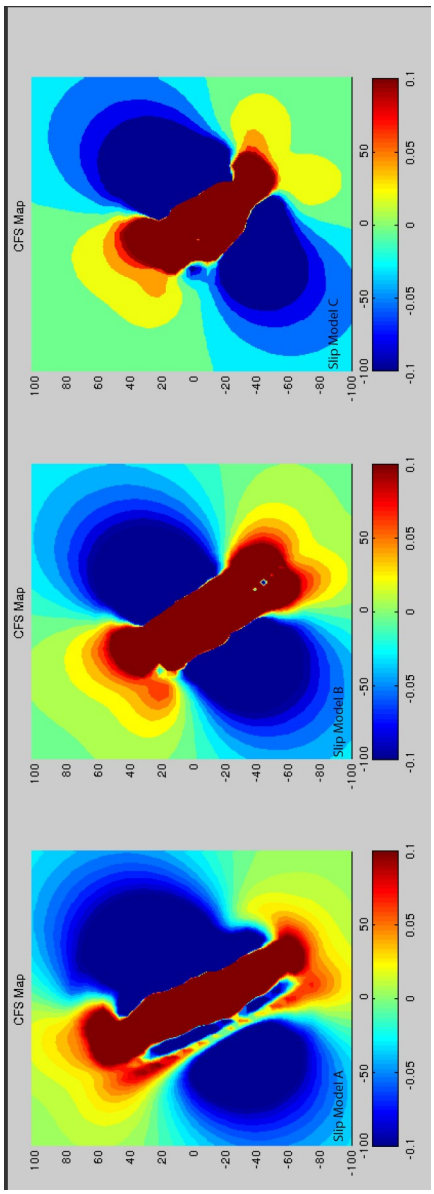

Figure 2.3 : Coulomb failure stresses computed at 10km depth using three used slip models with effective coefficient of friction $\mu' = 0.4$.

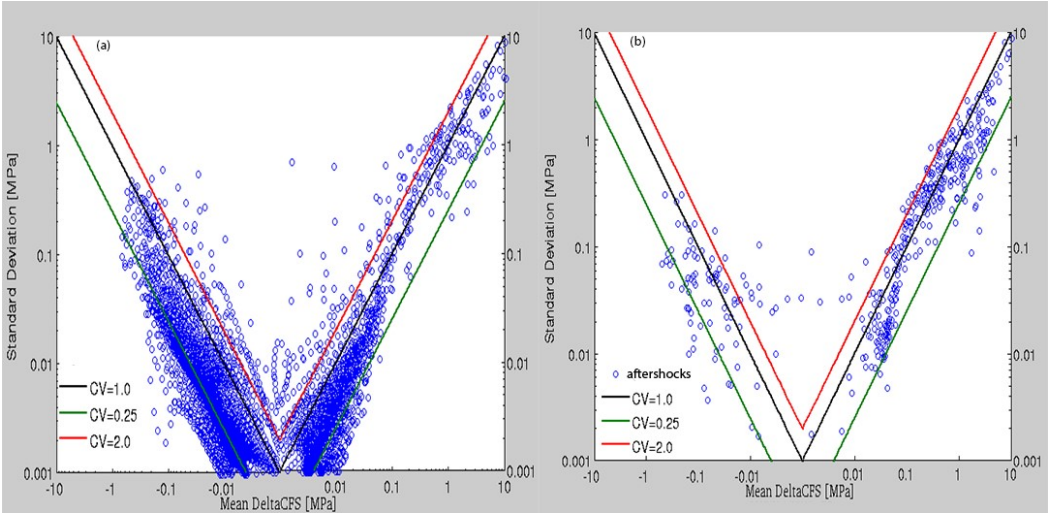

Figure 2.4: Standard deviation of calculated stress changes as a function of the mean stress change computed from three slip models. The result is plotted for the locations: a) where we have computed the stress changes at 10km depth and b) at the hypocenter of the aftershocks. The lines correspond to different values of the coefficient of variation CV.

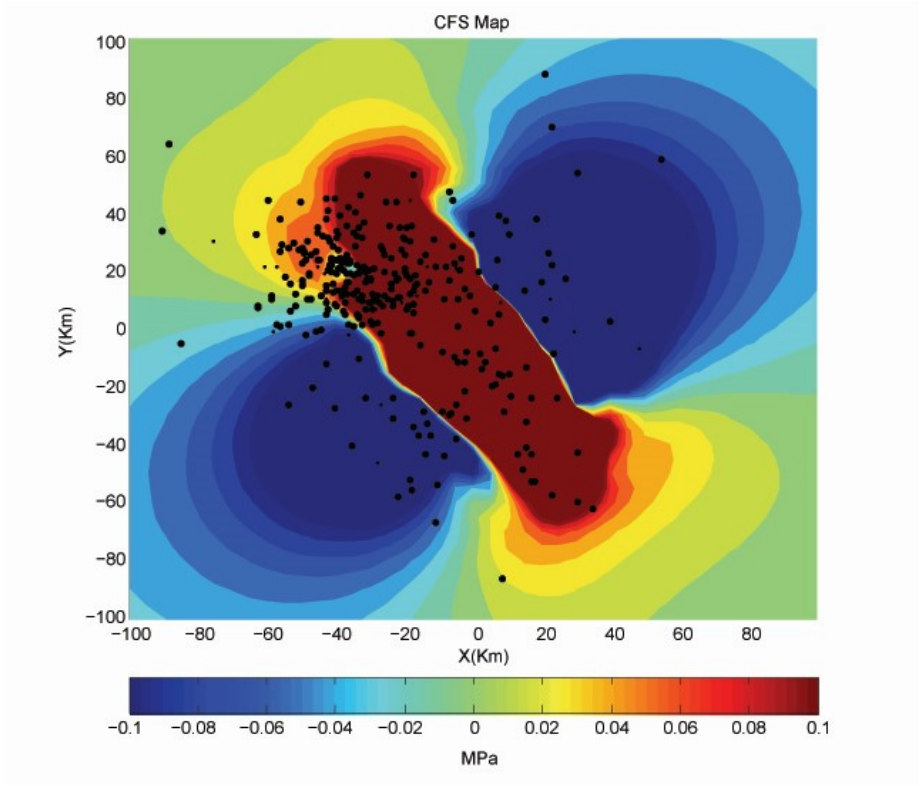

Figure 2.5: The mean Coulomb Failure Stress change (ΔCFS) calculated at 10km depth with μ'=0.4 assuming optimally oriented fault planes. Black dots refer to M≥3.7 aftershocks in the time period 0.5-10 days.

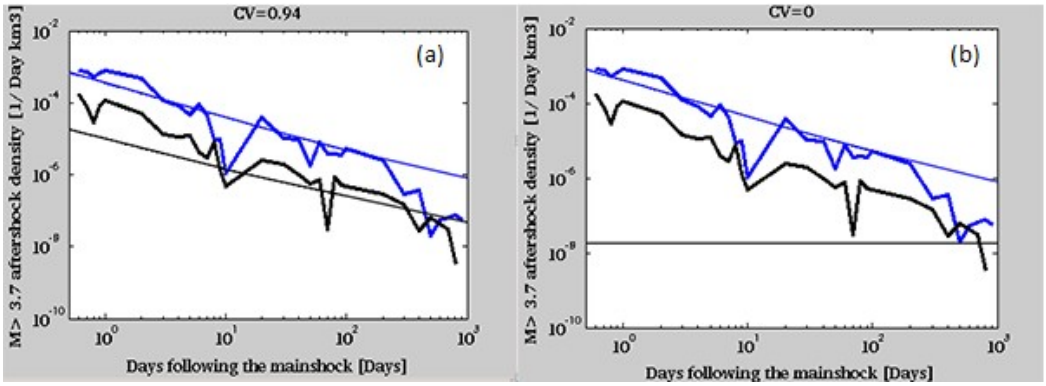

Figure 2.6: Comparison of the observed Kashmir's aftershock activity (bold lines) with that of the Coulomb rate-and-state model (thin lines): (a) with (CV=0.94) and (b) without (CV=0) consideration of stress heterogeneities. Blue and black curves are related to the earthquake density in regions with significant positive (ΔCFS>0.01 MPa) and negative (ΔCFS<-0.01MPa) stress changes, respectively. Model results were calculated with t_a =25,000 days, $A\sigma_n$=0.0185 MPa and r=0.055 events/day.

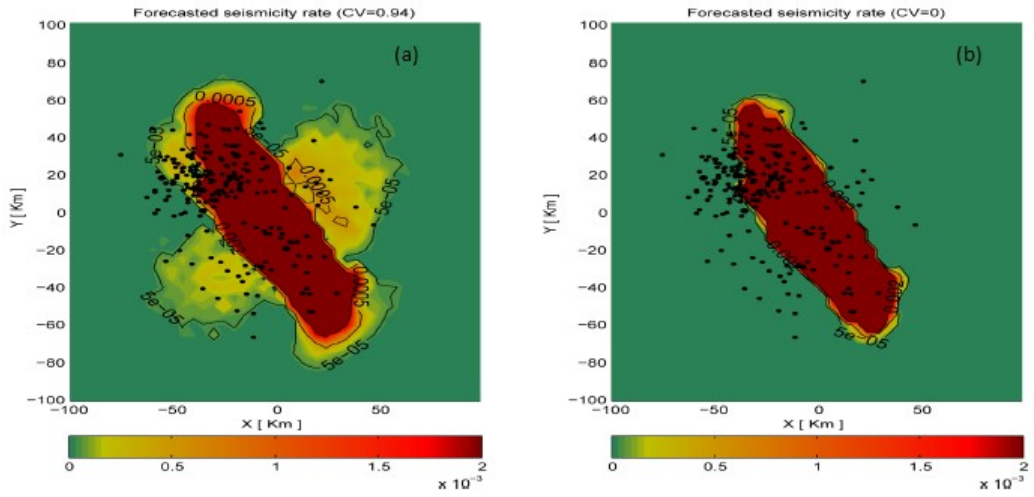

Figure 2.7: Spatial distribution of the aftershock rates (per 5km times 5km cell) forecasted by the model in comparison with the observed M≥3.7 aftershocks (dots) for the time interval [0.5, 10] days: (a) CV=0.94 and (b) CV=0. The other parameters are ta=25,000 days, $A\sigma_n$=0.0185 MPa and r=0.055 events/day.

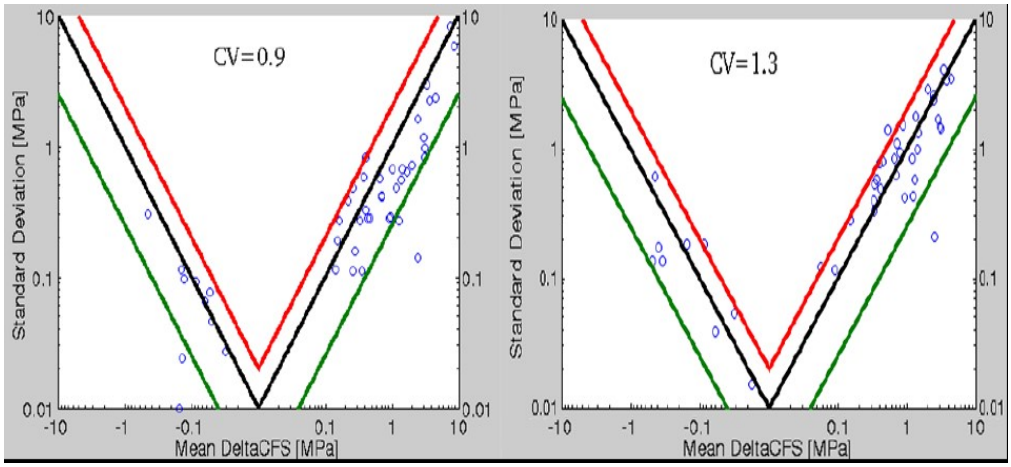

Figure 2.8: Standard deviationof calculated stress changes as a function of the mean stress change at the hypocenter of the aftershocks for the cases of direct aftershocks with estimated CV=0.9 and CV=1.3. The lines correspond to different values of the coefficient of variation CV (the values are same as that of figure 2.4).

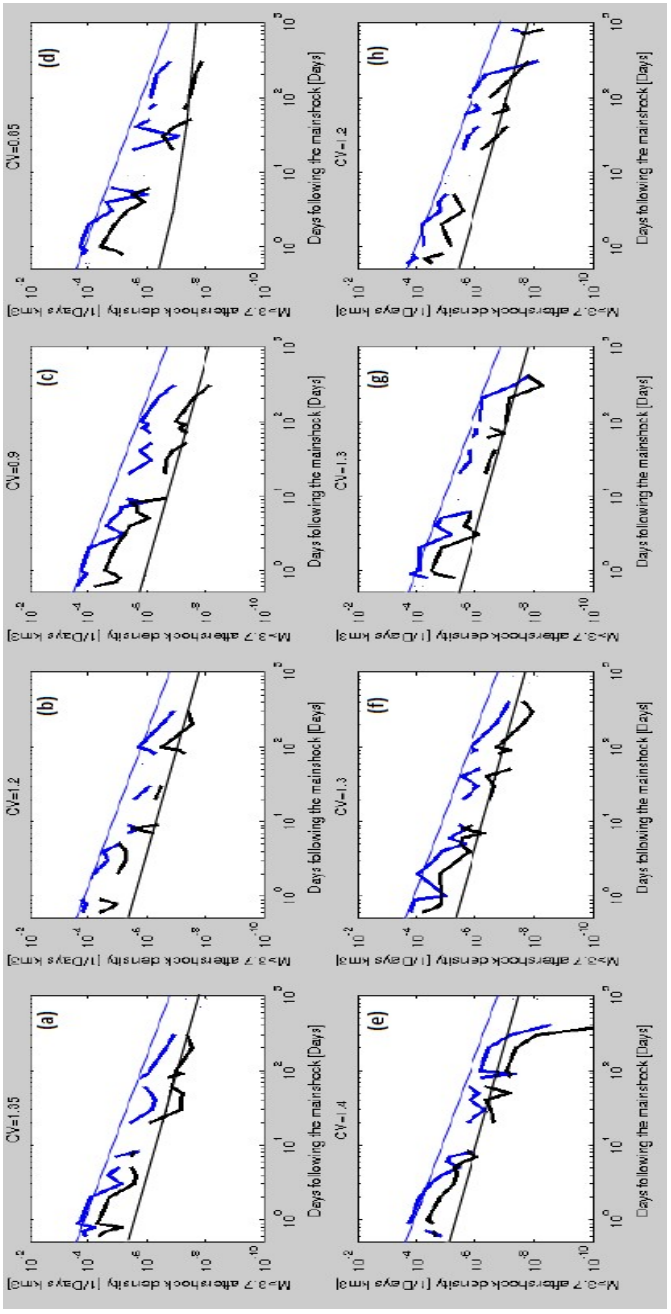

Figure 2.9: Comparison of the some stochastically declustered Kashmir aftershock activity (bold lines) with that of the Coulomb rate-and-state model (thin lines). Blue and black curves are related to the earthquake density in regions with significant positive (ΔCFS>0.01 MPa) and negative (ΔCFS<-0.01MPa) stress changes, respectively. Model results were calculated with t_a =25,000 and optimal values of Asig and r for each declustered catalog.

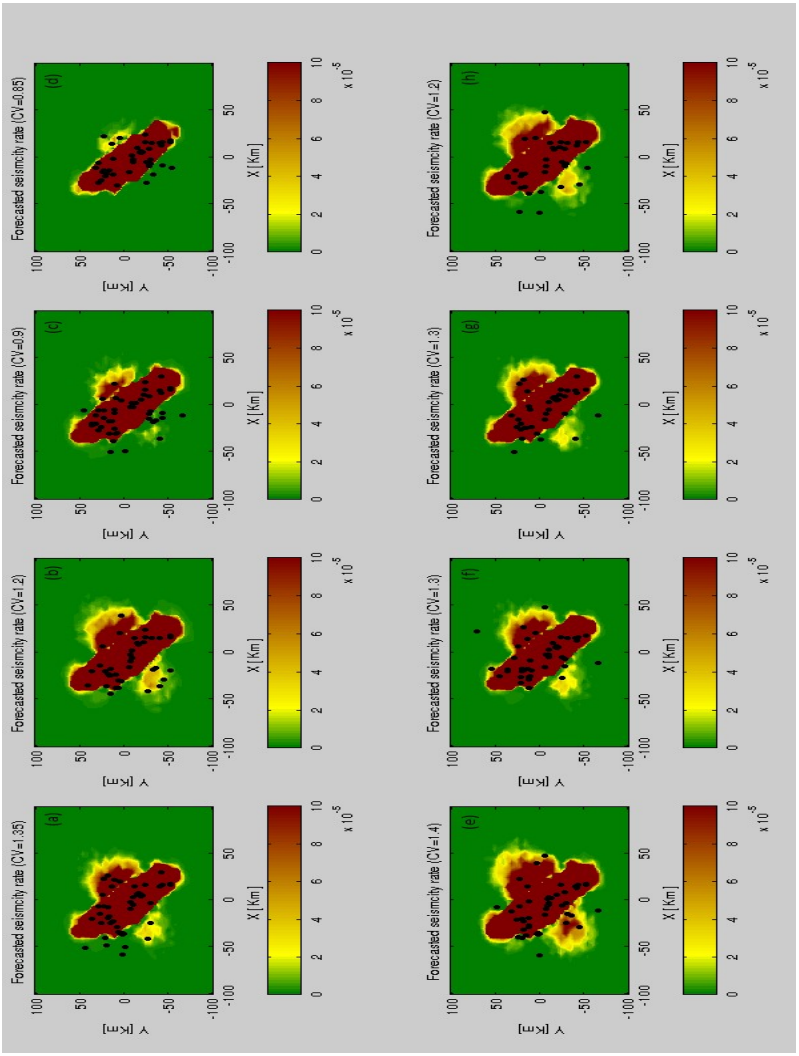

Figure 2.10: Spatial distribution of the aftershock rates (per 5km times 5km cell) forecasted by the model in comparison with the observed M≥3.7 aftershocks (dots) for the time interval [0.5, 10] days for the same stochastically declustered catalogs

Table 2.1: Estimated model parameters using 5km and 2.5km grid spacing for Coulomb stress calculation without considering uncertainties.

Aftershock time period (days) [0.5 1000]	$A\sigma_n$ (MPa)	r (events/day)	Log likelihood value
Grid-spacing: 2.5 km	0.028	0.072	-5141
Grid-spacing: 5km	0.031	0.0644	-4739

Table 2.2: Estimated model parameters using the original catalog and 100 stochastically declustered catalogs. ΔAIC refers to the difference between the value of the Akaike Information Criterion for the model without and with consideration of stress uncertainties. D refers to 100 stochastically deculstered catalogs.

t_a(Days)	Aftershock time period (days)	$A\sigma_n$ (MPa)	r (events/day)	CV	ΔAIC	Remarks
25000	[0.5 2.5]	0.012±0.001	0.1±0.002	0.95±0.02	287	Original Catalog
	[0.5 10]	0.017±0.001	0.095±0.003	0.96 ±0.03	324	
	[0.5 1000]	0.0185±0.001	0.055±0.002	0.94±0.01	360	
17500	[0.5 1000]	0.019±0.0015	0.103±0.004	0.92±0.02	349	
25000	[0.5 10]	0.0525 ±0.02	0.026±0.006	1.1±0.3	26	D

Table 2A: Summary of the input parameters for the randomized stress calculations (Hainzl et al., 2009).

	Mean	**Standard Deviation**
Compressional stress	10 Mpa	4 MPa
Uniaxial stress direction	$N7^0E$	10^0
Friction coefficient	0.3	0.1
Strike of fault segments	Defined for each model	3^0(rotation around central part)
Dip of fault segments	Defined for each model	3^0
Strike direction (rake)	Defined for each model	5^0
Slip	Defined for each model	30% relative

Chapter 3: Mechanics of the preseismic transient: The 2009 Mw 6.3 L'Aquila earthquake slow-slip and physics of the aftershocks

In general, earthquake foreshocks are not a reliable tool for predicting a main shock as they cannot be unambiguously distinguished from other sequences of small-magnitude earthquakes (e.g., Chen and Shearer, 2013; Brodsky and Lay, 2014). For example, based on the sequence of foreshock observations in Central Italy in early 2009 (ICEF, 2011), an occurrence of a strong earthquake was not anticipated in the region where the 2009 L'Aquila earthquake struck.

. This is inherent to the understanding of the mechanisms that stand behind the foreshocks and the difficulty in their identification as such in due time. Data from recent subduction zone earthquakes, the 2011 Mw 9.0 Tohoku, Japan (Kato et al., 2012), and the 2014 Mw 8.1 Iquique, North Chile (Brodsky and Lay, 2014), identified persistent nucleation of similar foreshock events migrating towards the future mainshock nucleation region that seem to be distinctive precursors for these two events. Specifically for the Tohoku earthquake the set of foreshocks that includes some repeating families of seismic events suggest the occurrence of a slow-slip event (SSE) (Kato et al., 2012). In continental regions, the 1999 Mw 7.6 Izmit, Turkey, earthquake (Bouchon et al., 2011), exhibited a phase of slow-slip at the base of the brittle crust prior to some mainshocks. Observations from Japan and Turkey, confirmed that these two types of different interplate earthquakes, subduction and transform, sometimes may exhibit slow-slip prior to the main shock. Such a behavior may have probably taken place prior to a number of interplate earthquakes (Bouchon et al., 2013).

The moderate size Mw 6.3 April 6th L'Aquila earthquake was preceded by an important foreshock sequence clustered near the base of the activated fault plane and repeaters were identified in the vicinity of the nucleation region (Chiaraluce et al., 2011; Valoroso et al., 2013). Furthermore, the seismic wave propagation yielded important changes, in the fault region, of the elastic properties of rocks prior to the earthquake (Lucente et al., 2010). Borghi et al. (2016) analysed continuous Global Positioning System (GPS) time-series, prior to the 2009 L'Aquila earthquake (see fig. 3.1a) in search of any transient deformation. The authors documented the slow slip events during 12th February – 26th February and compare evidence for a SSE from GPS data with seismological

constraints. In this chapter, we invert the average GPS deformation field into a slip model and characterize the stress loading on the 2009 Mw 6.3 rupture plane. We also compare the mainshock and aftershocks distribution with the Coulomb failure stress change, induced by SSE.

3.1 L'Aquila earthquake sequences

The Mw 6.3 L'Aquila earthquake (Fig. 3.1) caused 308 casualties and damaged a wide area. The seismic sequence (Fig. 3.1b) ruptured a NW-SE trending normal fault system in a region that has been interseismically extending NE-SW at a background rate of 2 mm yr−1 (D'Agostino et al. 2011). The main shock nucleated at a depth of 8.27 km (Valoroso et al. 2013) and ruptured an 18 km long fault (Cirella et al. 2009). The aftershock sequence (Valoroso et al. 2013) and the afterslip distribution (Anzidei et al. 2009; Gualandi et al. 2014) clearly show a much larger reactivated area, reaching 50 km of lateral extent. Aftershock data with more than 46.000 events (Chiaraluce et al. 2011; Valoroso et al. 2013) were relocated to provide an unprecedented resolution of the geometry of the faulting. These data provided a unique image of the geometry of the activated fault system, namely the L'Aquila fault to the south, the Campotosto fault to the north and associated antithetic faults. Additionally the study on the aftershock sequence increased the resolution on the foreshock distribution and allowed the identification of repeaters at the seismicity cut-off depth. At this depth a detachment has been clearly reported at the base of the high angle normal faults and likely characterized by a creeping behavior (Chiaraluce et al. 2011; Chiaraluce 2012; Valoroso et al. 2013). It is worth highlighting that the foreshocks extended far away from the main-shock fault rupture and over an area almost larger in size than the aftershock extent (Figs 3.1b and c). Furthermore, the temporal variations of seismic velocity and anisotropy revealed important changes in the elastic properties of the medium during the preparatory phase of the main shock (Lucente et al. 2010). Complementary to seismological data, GPS data sets were used to study both the coseismic (e.g. Anzidei et al. 2009) and postseismic deformation (D'Agostino et al. 2012; Gualandi et al. 2014).

3.2 Inversion Methodology and Slip model

We tested a range of possible fault slip models that best explains the observations. This in turn would lead to greater confidence in the stress modeling that is dependent on these slip distributions.

We followed a formal inversion of the derived GPS displacements and provide a metric for assessing the relative fit of models (Okada, 1985; Harris and Segall, 1987, Jonsson et al., 2002).

We solve for fault slip using linear least approach for a given surface displacement

$$D = g(M) + \epsilon \qquad (3.1)$$

in which, Okada (1985) describes the Green's function, g, that linearly relates the model vector M to the data vector D with errors ϵ. We use the Matlab parameter optimization toolbox program called lsqlin that performs a linear least-squares inversion of Green's functions to define the best-fitting set of models to describe a dataset with the pertinent errors. In order to solve for a more realistic slip model and avoid the oscillation in the fault slip, we need to constraint the interdependence between individual slip patches. Haris and Segall (1987) proposed a method to address this problem and introduced the parameter "roughness of the slip patch". This method works to minimize the 2D second-order derivative (Laplacian) of the slip surface so that large changes are constrained within a certain value. The solution roughness is the average second-order finite-difference sum of each fault patch:

$$\rho = \frac{\sum_i |p_i|}{2N} \qquad (3.2)$$

Where $p_i = DM$ and N is the number of fault patches. The constant 2 is the result of smoothing the solution both along the fault strike and across strike.

To account for the roughness vs. misfit within the inversion we had to consider fault models with at least 2 patches beneath each single fault. The number of sub-fault patches satisfies the common approach that divides the fault into a number of unknown slip patches that is less than the number of data (e.g. Thatcher, 1979; Savage et al., 1979).

We first used the four sub-fault patches without any constraint on rake beneath both L'Aquila and Campostoto faults. We tested 3 different fault geometries: one accounting for a flat decollement beneath L'Aquila and Campotosto faults as revealed by the aftershock distribution (e.g. Valoroso et

al., 2013) and two hypothetical fault models with 10 and 45-degree down-dip extensions of both faults. In our result (Fig. 3.2) we find that assumption of flat decollement beneath the 2 faults best explains the surface displacements and therefore excludes a down-dip extension of both faults as the misfit is considerably high for such models. We then tested other models by removing one of the candidate fault planes. We run the inversion with only sub-fault patches beneath either L'Aquila or Campotosto faults and see if it improves or degrade the data fit. Figure 3.3 illustrates the result of the inversion. We find higher values of misfit between predicted and observed GPS displacement, therefore degrading the data fit. Figures 3.2 & 3.3 clearly show that a flat extension beneath both L'Aquila and Campotosto faults best explains the observations. Accordingly we adopt the flat geometry with 4 sub-fault patches beneath both faults. We then test cases with and without any constraint on rake. The results depicts that there is a slight difference between misfit for both cases as shown in Figure 3.4. Although the case without any constraint on rake gives a better misfit between observed and predicted GPS displacements, the directions of slip vectors for each sub-fault patch are not consistent among them. In Figure 3.5 we plot candidate solutions picked from the misfit-roughness curve for models without any constraint on the rake. Figure 3.5a & 3.5b give the minimum values of misfit, but do not constraint coherence between individual sub-fault patches. In the work of Harris and Segall (1987) and Jonsson et al. (2002) the realistic slip model is the one which has minimum value of roughness of the slip patch and constraint coherence between individual slip patches. Models reported in Figure 3.5c &3.5d depict some coherence between the individual sub-fault patches, but still one sub-fault patch exhibits different slip direction. Figure 3.6 shows the different solutions of slip model with constraint on rake. In this case, we put constraint on the rake of the sub-fault patch adjacent to L'Aquila fault. The constraint is consistent with the aftershock focal solutions that took place on the decollement (Valoroso et al., 2013). The inverted slip distribution with minimum value of misfit as shown in Figure 3.6a &3.6b show similar slip distributions for the case without any constraint on rake shown in figure 3.5c &3.5d. The solutions shown in Figure 3.6a and 3.6b, although exhibiting smaller misfit values, seem to be under-smooth solutions in their slip values (Jonsson et al., 2002) exhibiting high roughness. The inverted slip distributions shown in Figure 3.6c & 3.6d improve the coherence

between individual slip patches and exhibit low roughness. Accordingly our preferred solutions are represented in Figure 3.6c &3.6d.

3.3 Forward Model

We then used the inversion solutions shown in figures 3.6c and d as starting models for a trial and error forward model in order to improve the misfit values without adding complexity to the fault model. Further to the dislocation surface that consists of a decollement we added antithetic faults as illustrated by the high-resolution aftershock and foreshock relocation (Chiaraluce 2012; Valoroso et al. 2013). The presence of the decollement is further confirmed by the flat nodal planes of the focal solutions as well as the existence of sparse seismicity beneath the decollement itself (Chiaraluce 2012). The slip model (Fig. 3.7) that best fits the GPS, with a misfit of 0.26 mm when compared with the computed vectors, consists then of a decollement with four patches very similar to the models represented in the figures 3.6c and d. The decollement located at 9.25 km, strikes parallel to the L'Aquila and Campostosto faults and dips 0.5 degree to the southwest. To fit the near fault GPS data we added two shallow antithetic faults and their geometry is defined by the aftershock distribution. The largest slip patch on the decollement reaches about 2 cm over an area of 160 km2 right beneath L'Aquila fault. Approximately 2860 km2 area slipped along the decollement during the SSE with an average slip of 0.9 cm. Adding to this the slip on the antithetic faults, the estimated total moment release by the SSE is equivalent to an Mw 5.9 event. The major contribution to the total moment release comes from the slip on the decollement beneath the L'Aquila fault. We interpret motion on the antithetic faults as shallow and local accommodation of the deeper slip on the decollement.

3.4 SSE and Stress Loading

We next used Coulomb 3.3.0.1 (Toda et al., 2005; Lin and Stein, 2004) to resolve stress changes (Fig. 3.8) on the L'Aquila and Campotosto faults imposed by the 12th February 2009 Mw 5.9 *SSE*. This code is designed to calculate static displacements, strains, and stresses at any depth caused by fault slip, magmatic intrusion, or dike expansion/contraction (coulomb 3.3 manual). This code

can also used to calculate displacements on GPS stations caused by fault slip. Calculations are made in an elastic halfspace approximation with a uniform isotropic elastic properties following Okada (1992).We compute the Coulomb failure stresses with an effective friction coefficient of 0.4 and resolve stress changes on L'Aquila fault that increased with 1.1 bar at the hypocenter of the main shock (8.27 km) and over 2 bars at the hypocenter of the M4.0 March 30th foreshock (9.05 km). It is worth highlighting that the unique correlation between the positive stress change and the foreshock that took place after the 12th February and specifically those located on the deeper antithetic fault (Section AB, Fig. 3.8). Regarding the Campotosto fault (Section CD, Fig. 3.8) the increased stress change mimics fairly well the distribution of the aftershocks both on the fault and on the reactivated antithetic fault. It is conceivable that the *SSE* caused substantial stress loading on the hypocenter of the L'Aquila earthquake. The stress loading caused first the rupture of the Mw 4.0 foreshock, weakening therefore part of the geometrical barrier between the decollement and the high-angle L'Aquila fault. The Mw 4.0 foreshock was then followed by a sequence of events, at the seismogenic depth, and mostly located on an antithetic fault accommodating the deformation on the geometrical barrier and favoring therefore fluid diffusion processes (Lucente et al., 2010) that contributed to the initiation of unstable dynamic rupture a week later.

We find that slip on the decollement increased the static stress at seismogenic depths. The spatial correlations between the Coulomb stress increase and the distribution of the unusual aftershock sequence are compelling. This suggests that the *SSE* loaded not only the M4.0 foreshock and Mw 6.3 main shock fault but also controlled the lateral distribution of the aftershocks that could not be otherwise explained by the stress change imposed by the L'Aquila main event.

3.5 Conclusion

In this chapter, we first demonstrate that the inversion of GPS data into a slip model reveals the existence of a decollement related to both L'Aquila and Campotosto fault planes and such a decollement accommodated SSE between 12th February and 26th February, that is equivalent to a magnitude Mw 5.9 earthquake. The SSE has caused substantial stress loading at seismogenic

depths where the magnitude Mw 4.0 foreshock and Mw 6.3 main shock nucleated. This stress loading is also spatially correlated with the lateral extent of the aftershock sequence.

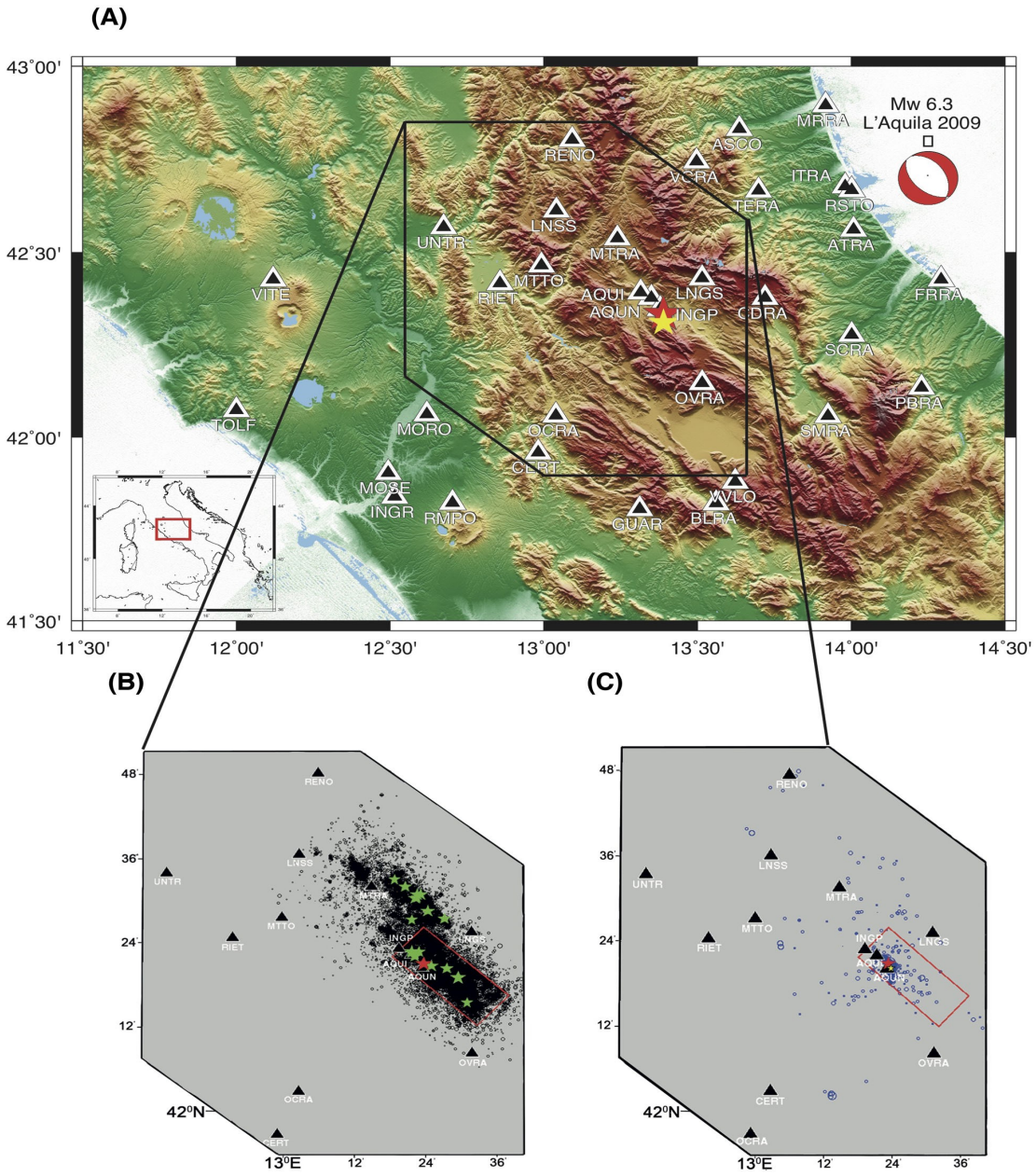

Figure 3.1: (A) The 2009 April 6 L'Aquila, Central Italy, earthquake (red star also in panels B and C; focal mechanism from Cirella et al. 2009) and March 30th magnitude 4 foreshock (yellow star also in panel C). (B,C) Zoom on the L'Aquila aftershock and foreshock sequence (Valoroso *et al.* 2013), green stars are aftershocks with magnitude equal or larger than 4, blue circles are foreshocks and the red rectangle represents the surface projection of the rupture area of the main

shock (Cirella *et al*. 2009). Black triangles are Continuous GPS stations operating since 2007. The DEM used in the plot is derived by Shuttle Radar Topography Mission (SRTM-3).

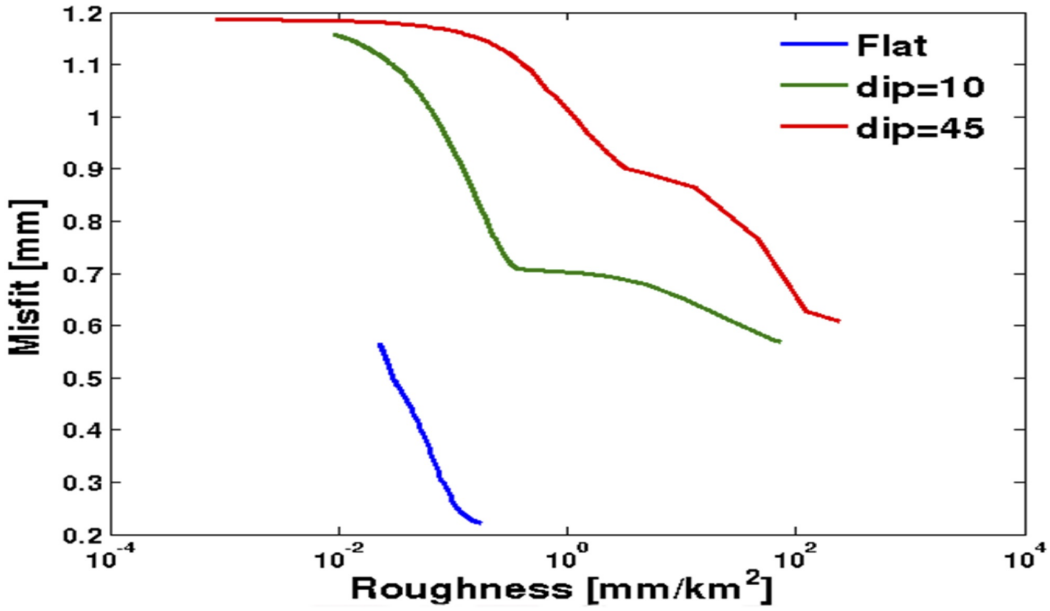

Figure 3.2: Misfit vs. roughness of slip distribution inverted from real data without any constraint on rake with the assumption of constant fault dip and flat beneath both L'Aquila and Campotosto faults.

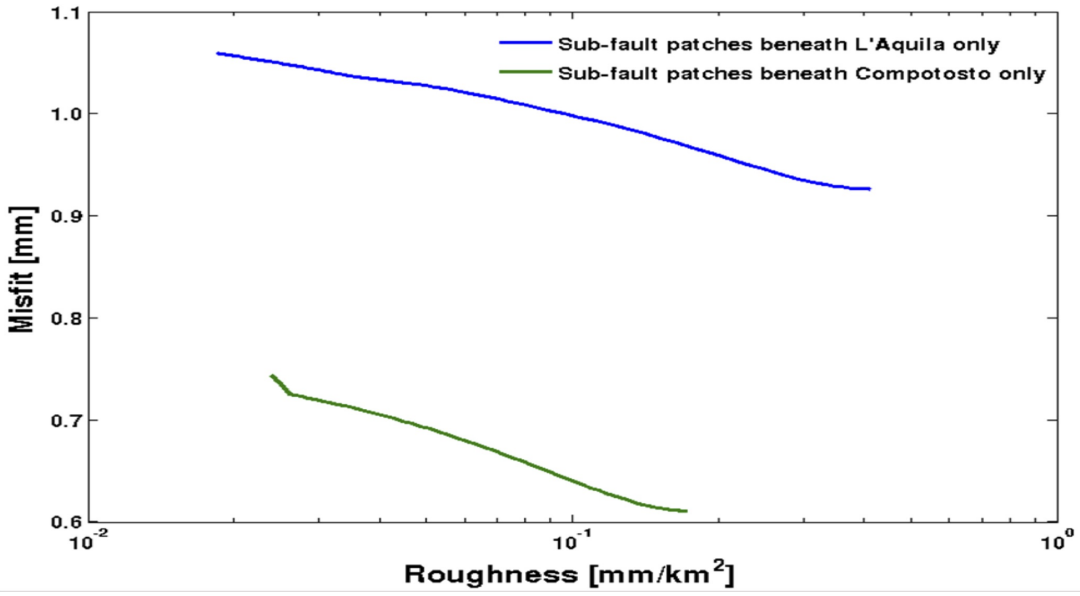

Figure 3.3: Misfit vs. roughness of slip distribution inverted from real data without any constraint on rake with sub-fault patches beneath either L'Aquila or Campotosto fault.

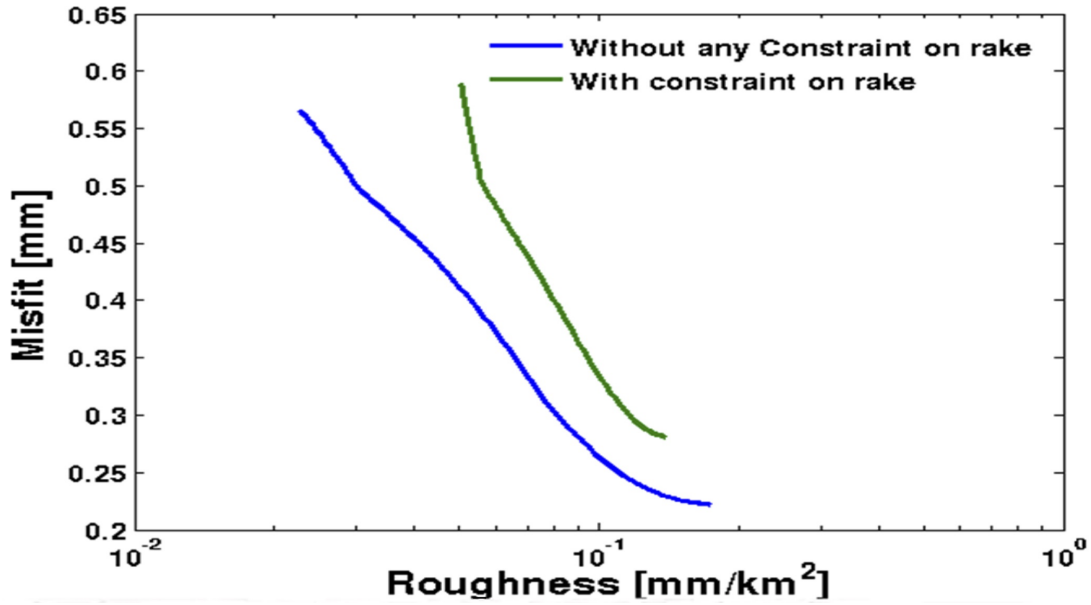

Figure 3.4: Misfit vs. roughness of slip distribution inverted from real data with and without any constraint on rake with the assumption of flat beneath the both L'Aquila and Campotosto fault.

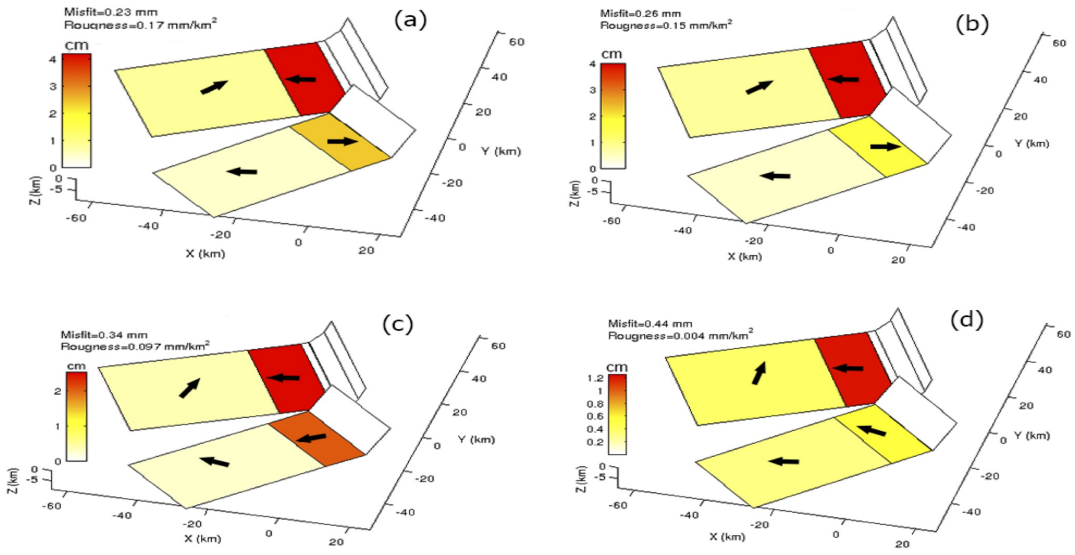

Figure 3.5: Slip distributions inverted from real data without any constraint on rake.

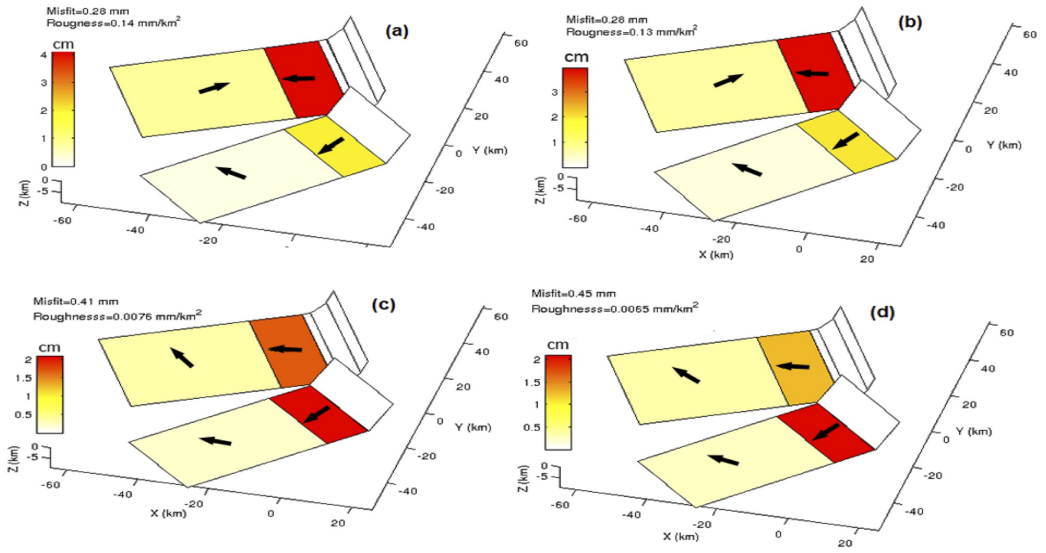

Figure 3.6: Slip distributions inverted from real data with constraint on rake, on the patch adjacent to the L'Aquila Fault.

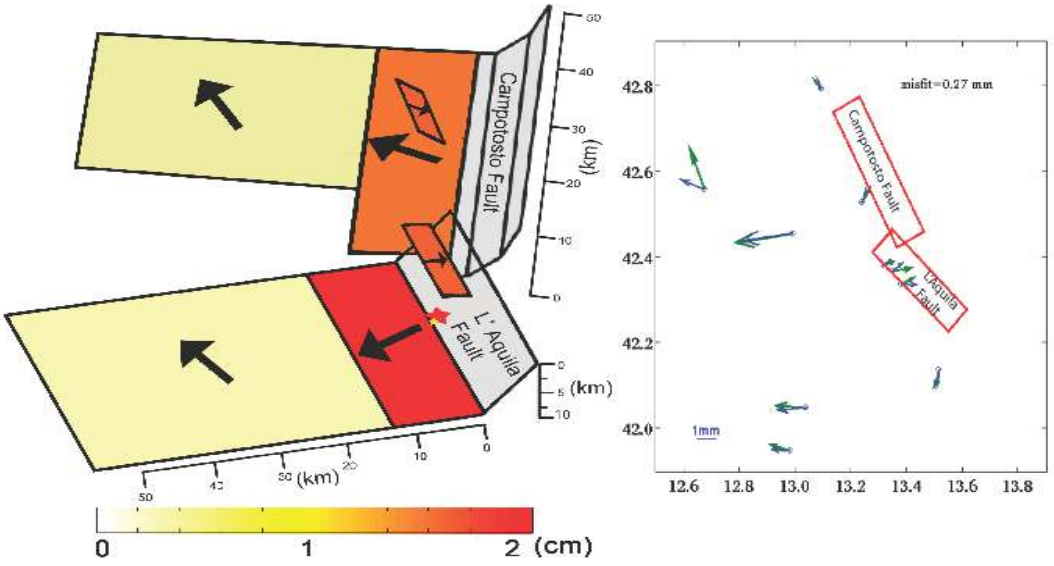

Figure 3.7: Slip model of the slow slip events (SSE), where block arrow indicates the rake direction. The green and blue arrow depicts the observed and model displacement vector. The red and yellow stars show the epicentre of mainshock and largest foreshock respectively.

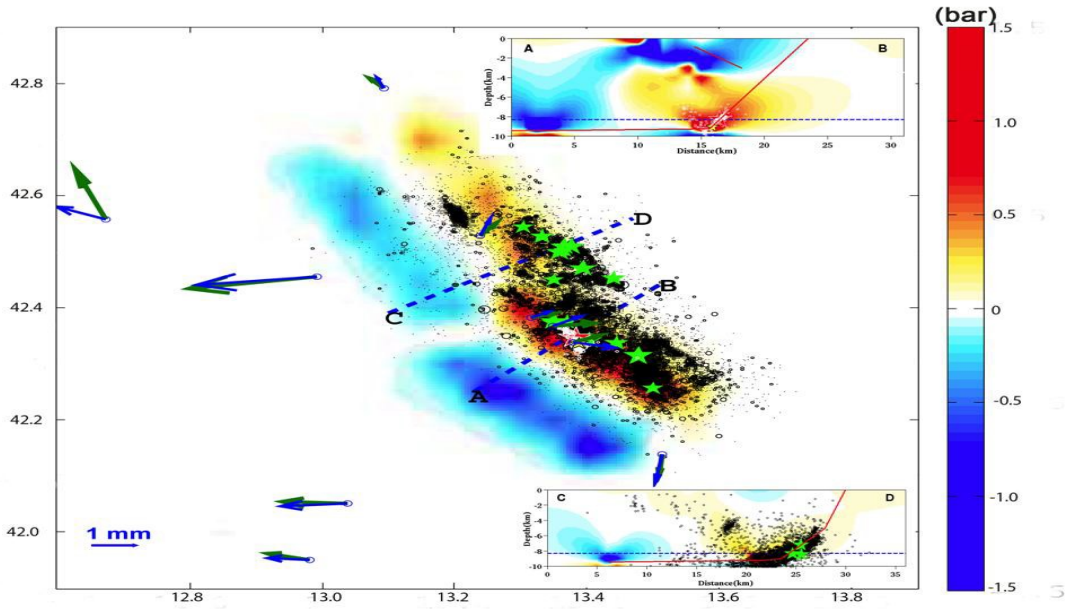

Figure 3.8: SSE Coulomb stress change and the L'Aquila main shock (in red), post February 12 foreshocks (white and the yellow star for March 30 magnitude 4) and aftershock sequence (green stars are aftershocks with magnitude equal or larger than 4). AB and CD are vertical sections across the reactivated L'Aquila and Campotosto faults, respectively. The green arrows are SSE observed GPS displacements while the blue arrows are computed using the slip model in figure 3.7.

Chapter 4: Physics of the interseismic deformation: The Idrija Fault system in Western Slovenia

Continental deformation in the Adriatic region is dominated by the continued collision between the Adriatic microplate and Eurasia at rates of 2-4 mm/yr (e.g., D'Agostino et al., 2008; Metois et al., 2015). Space geodesy, earthquake focal mechanisms andstructural data show changes of the deformation associated with this convergence, from pre-dominantly northward thrusting along the Alpine foreland in NE Italy to dextral strike-slip in Western Slovenia. Although generally low magnitude, the region is characterised by high levels of seismicity and has experienced a number of devastating earthquakes over the last 500 years (Fig. 4.1). These include the 1511 M6.9 Western Slovenia earthquake (Fitzko et al., 2005), the 1976 Ms 6.5 Friuli earthquake (Aoudia et al., 2000), the 1998 Ms 5.7 Bovec and the 2004 Mw 5.2 Krn earthquakes (Bajc et al., 2001; Borghi et al., 2009). The Ravne fault was responsible forthe 1998 and 2004 earthquakes (Bajc et al., 2001; Borghi et al., 2009) whilst the Idrija fault, a major structure in Western Slovenia, is often considered as the most probable source responsible for the largest known earthquake in the region in 1511 (Fitzko et al., 2005). Although the exact location of the earthquake is unknown, it is thought to have ruptured only a 50-kmlong section of the 100-km-long Idrija fault (Fig.4.1, Fitzko et al., 2005; Burrato et al., 2008) leading some to believe that the fault has the potential for future earthquakes of a similar magnitude (Burrato et al., 2008). In the eastern part of the region, some other faults have similar morphotectonic features as the Idrija. However, only small and intermediate earthquakes might be associated with them, such as the 1721 M6.0 Rijeka, 1895 M6.3 Slovenia, 1897 M5.6 Ljubljana, and 1926 M5.7 Slovenia earthquakes (Burrato et al., 2008). Wang et al. (2017) use 75 radar acquisitions on the descending track 79 (46 ERS-1/2 and 29 Envisat) and 45 acquisitions on the ascending track 86 (9 ERS-1/2 and 36 Envisat). The authors construct rate maps using the multi-interferogram method [Biggs et al., 2007] implemented as Poly-Interferogram Rate and Time-series Analysis (Π-RATE) software (Wang et al., 2012). All pixels in the final rate maps have at least 25 linear-independent observations and their 1σ errors

are no more than 1 mm/yr. The rate maps and profiles on both tracks show clear velocity gradient with uplift towards northeast of an Idrija fault and consistent magnitude around the Idrija fault whist relatively flat elsewhere (See Fig. 4.2). Savage and Prescott (1978) solved interseismic deformation for infinite long strike slip fault. But this formulation is restricted to homogenous elastic medium. A simple analytical solution did not explain the asymmetrical behaviour of the Interseismic velocities across the Idrija fault.

Previous studies showed the San Andreas fault (SAF) and other major active strike slip fault exhibits asymmetric pattern of interseismic velocities (Fialko et al., 2006; Fialko et al., 2002) and often related to the lateral variation in rigidity (Le Pichon.et al., 2005). The magnitude of rigidity contrast inferred from the high resolution seismic tomography could vary up to factor of 2-2.5 (Hauksson.et al., 2000; Fialko et al., 2006; Lindsey et al., 2013). For example, a 50% velocity contrast suggests a rigidity ratio of approximately 2.25 from the following relation: $.\frac{\mu_1}{\mu_2} = \frac{\rho v_1^2}{\rho v_2^2}$ in which μ is the shear modulus; v is the shear velocity and ρ is the density. Lindsey et al. (2013) demonstrated the geometry of the creep portion of the SAF play a more significant role than rigidity contrast across the fault. In order to study the deformation pattern, we model numerically the asymmetrical pattern of the interseismic velocities across the southern portion of the Idrija fault. We explore both the assumptions about the fault geometry at depth and the heterogeneous properties of the crust in order to explain the observed asymmetric strain rate pattern across the Idrija fault.

4.1 Numerical model description and computational approach

We employ a 3-D model domain V (2000 km by 1000 km by 400 km) with Dirichlet boundary conditions enforcing symmetry to approximate an infinitely long strike-slip fault. We implement the velocity boundary conditions on –x and +x faces to mimic the observed block motion on both side of the fault, giving a relative plate motion of 2.0 mm/year. We constrain the vertical displacements on the bottom of the domain to be zero. Finally, we fix the x displacements on the -y and +y faces to enforce symmetry consistent with an infinitely long strike-slip fault. Figure 4.3 shows the approximated geometry of the infinite long strike-slip fault, embedded in an elastic layer of

thickness 45km overlying a Maxwell viscoelastic half space. The upper portion (red colour) of the fault is locked up to 20km between earthquakes; while the lower portion creeps (green colour) at plate velocity depicts a simple earthquake cycle. We generate the tetrahedral meshes using Trelis software (available from www.csimsoft.com/trelis). We discretized the model space using elements of 6.7 km size in the vicinity of the fault that increase in size at a geometric rate of 1.01 toward the outer regions of the mesh. This result is in a maximum discretization size of approximately 30 km for the coarser meshes (see Fig.4.4).

We use Pylith code developed by Computational Infrastructure for Geodynamics (CIG) that uses finite-element formulation for elasticity with a domain decomposition approach (Aagaard et al., 2013) similar to the "traction at split nodes" technique (Andrews, 1976; Day, 1982; Duan and Oglesby, 2005) to model both quasi-static and dynamics crustal deformation. Implementations of various boundary conditions, discretization schemes, and bulk and fault rheologies are possible within Pylith code. The equation for elasticity including the inertial term is defined as

$$\rho \frac{\partial^2 u}{\partial t^2} - f - \nabla \cdot \sigma = 0 \; in \; V \qquad (4.1)$$

$$\sigma \cdot n = T \; on \; S_T \qquad (4.2)$$

$$u = u_0 \; on \; S_u \qquad (4.3)$$

$$d - (u_+ - u_-) = 0 \; on \; S_f \qquad (4.4)$$

Where u is the displacement vector, ρ is the mass density, f is the body force vector, σ is the Cauchy stress tensor and t is the time. The traction T is applied on surface S_T (surface with Neumann boundary conditions), displacement u_0 on surface S_u (surface with Dirichlet boundary conditions), and slip d on fault surface Sf.

Several visco-ealstic models with combinations of elastic and viscous elements have been provided within Pylith code to model both interseismic deformation and postseismic relaxation. The most common visco-elastic model is Maxwell fluid. A Maxwell fluid connects a spring and dashpot in series as shown in figure 4.5, so the spring responds to the instantaneous stress change, whereas the dashpot can be accounted for the relaxation to this stress change. The constitutive relation of a linear Maxwell fluid is,

$$\dot{\varepsilon}_{total} = \dot{\varepsilon}_{spring} + \dot{\varepsilon}_{dashp} \quad = \frac{\dot{\sigma}}{2\mu} + \frac{\sigma}{2\eta} \qquad (4.5)$$

Where $\dot{\varepsilon}$ is the strain rate, σ is stress, μ is shear modulus, and η is viscosity. To solve for the stress distribution for an earthquake like impulse, one can assume a instantaneously strain change ε_0, so stress σ is,

$$\sigma(t) = 2\mu\varepsilon_0 e^{-\frac{\mu}{\eta}t} \qquad (4.6)$$

$$\sigma(t) = 2\mu\varepsilon_0 e^{-\frac{t}{\tau}} \qquad (4.7)$$

Where τ is called characteristic relaxation time which describes how rapid the relaxation decays.

4.2 Results and Discussion

We first simulate several earthquake cycles considering the homogenous elastic layer with shear modulus 'μ' of 30GPa overlying a Maxwell material with viscosity 'η' of 2.36682e+19 Pa-s, yielding a relaxation time of 50 year. The approximation of steady state plate motion is approached after many earthquake cycles, once the transient behaviour present in the model will have nearly disappeared. We compare the simulation results with the analytical solution and found the best match between numerical and analytical solution. We then proceed the rest of the simulations with a heterogeneous medium. For the case of inhomogeneous elastic models, we fix the relaxation time to 50 year by decreasing the viscosity of the Maxwell material across the western Idrija fault. We then test several inhomogeneous elastic models and models with varying dip of the creep portion of fault in the range of 45-90 degree. We also run the simulation with different locking depth, length of the creep section and varying the slip rate along the creep portion in the range of 1-3 mm/yr. The simulation results demonstrate that model with 80 degree dip of the creep section of the fault and shear modulus ratio of μ_1/μ_2~2 improve the misfit between observed and modelled interseismic velocities as shown in the figures 4.6a and 4.6b. The model predicted interseismic

velocities fit the observation quite well as shown in figures 4.7a and 4.7b. The data and model results shown in this work demonstrate that asymmetrical interseismic velocities are related to both geometry of the creeping section and crustal heterogeneities of the upper elastic crust. The loading rate and locking depth of the fault computed from the numerical model are 2.2 mm/yr and 20km respectively is quite similar to the values, estimated from the analytical model. Our numerical results suggest that geometry of the creeping section of the Idrija fault is more dominant than the heterogeneities across the fault. Similar conclusions are reached in a relatively similar environment, with a right lateral strike-slip faulting, on the San Andreas by Lindsey et al. (2013).

The major faults such as Idrija, Predjama and Rasa in Western Slovenia have been thought to be mainly dextral strike-slip from active tectonics and seismological studies (Poljak et al., 2000). Sparse GPS measurements show the present-day regional dextral slip rate of 2-3 mm/yr across this region (D'Agostino et al., 2008; Cheloni et al., 2014; Metois et al., 2015), generally consistent with the long-term slip rate of 1-4 mm/yr on the Idrija fault from LiDAR data (Moulin et al., 2014). Besides dextral slip, Moulin et al. (2014) identified a significant vertical component with rakes ranging from 0 to 30◦ in central Idrija fault, implying uplift in the northeast side of the fault. Dip of the Idrija fault is documented as ranging between 60 and 80 degree towards the northeast (Poljak et al., 2010). In this study, we find best-fit dip value of 80 degree and μ_1/μ_2~2, constrained by descending and ascending InSAR observations. We also estimate the dip-slip rate~ 2mm/yr, which is comparable to strike-slip rates.

Several large historical earthquakes occurred in Western Slovenia, in which the largest is the 1511 M6.9 earthquake whose epicentre is most likely at the Idrija fault (Fig. 4.1). In the western part of our study region, other instrumental recorded important events are the 1976Ms 6.5 Friuli, 1998 Ms 5.7 Bovec and 2004 Mw 5.2 Krn earthquakes (Aoudia et al., 2000; Bajc et al., 2001; Borghi et al., 2009). While the eastern part is absent from large earthquakes, hence may imply substantial seismic gaps (Burrato et al., 2008). The Idrija fault was thought to be ruptured only 50 km during the 1511 earthquake, about 1/2 of its total length (Fitzko et al., 2005). According to the scaling relationship for surface displacement to rupture length (Wells and Coppersmith, 1994), the coseismic slip in the 1511 earthquake was referred as 1.2 meter. Assuming a constant slip rate as our best-fit estimate of 2 mm/yr, the accumulated slip has been 1.4 meters already since the 1511

earthquake, which corresponds to a magnitude 7 earthquake (Wells and Coppersmith, 1994). The historical earthquakes shown in Figure 4.1 only released about 20% of the whole strain accumulation, and the net deficit still corresponds to an earthquake of similar magnitude than the 1511 earthquake. Higher moment deficit was suggested in the western Adriatic region from GPS data (Cheloni et al., 2014). As discussed by Cheloni et al. (2014), such high deficit might be released by a single large earthquake or by a sequence of smaller ones like the 1976 Friuli or the 1511 Western Slovenia earthquakes. For the latter case, current moment deficit is large enough, and the Idrija fault might be approaching the end of the interseismic phase of the earthquake cycle. Considering the 1511 earthquake occurred most probably the western segment of the Idrija fault, the probability of earthquake occurrence in the east is likely higher.

4.3 Conclusion

The 3D finite element numerical model which incorporates both the dip of the creeping section and medium heterogeneities across the Idrija fault, allow us to model the asymmetrical pattern of the interseismic velocities. It also strength our point that the asymmetrical pattern due to uplift towards the northeast of Idrija fault is more likely related to the geometry of the fault. The results also show that elastic heterogeneities does not improve the fit indicating that variation in material properties are not very significant in this region.

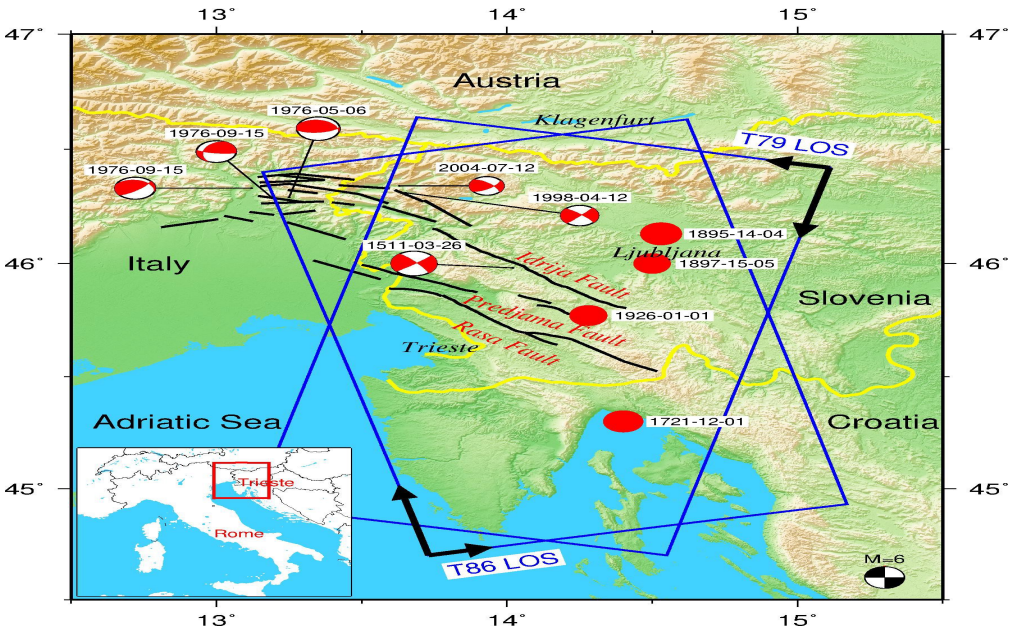

Figure 4.1: Topographic and tectonic map of the study area. The black lines represent major faults in this region. The red-white beach-balls show focal mechanisms of the major earthquakes and the large aftershocks for the 1976 Friuli earthquake. Red circles indicated probable epicentre of historical earthquakes with the same scale of the beach-balls (from Burrato et al. (2008) and references therein). The blue rectangles delimit the extents of our radar data on the descending track 79 and ascending track 86, and arrows on top of them indicate their flight and line-of-sight (LOS) directions. Red box in inset shows the area of the main figure.

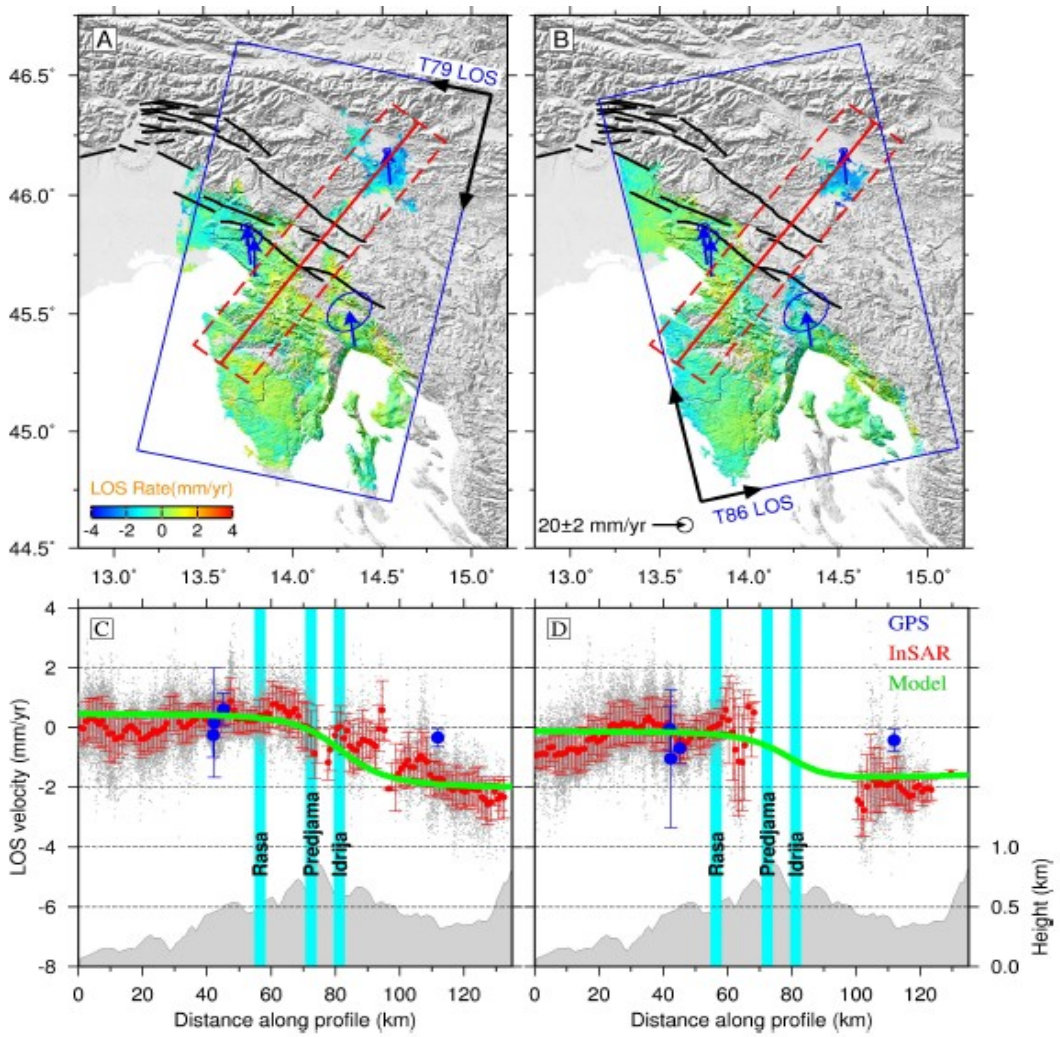

Figure 4.2: (a and b) LOS rate maps on the descending track 79 and ascending track 86 respectively. Positive values indicate away from satellite. Dashed red box shows extent of the profiles with bin width of 30 km. Blue arrows represent velocities of four GPS sites from Metois et al. (2015). The other symbols as with Figure 4.1. (c and d) LOS InSAR (red), GPS (blue) and model (green) velocities with 1σ error bars, as well as elevation (gray) along the profiles in Figures 4.2a and 4.2b respectively. Gray dots denote all InSAR observations within the profile bins. The model and GPS data are projected into InSAR LOS direction using local incidence angles. The cyan bars mark the locations of Rasa, Predjama and Idrija faults.

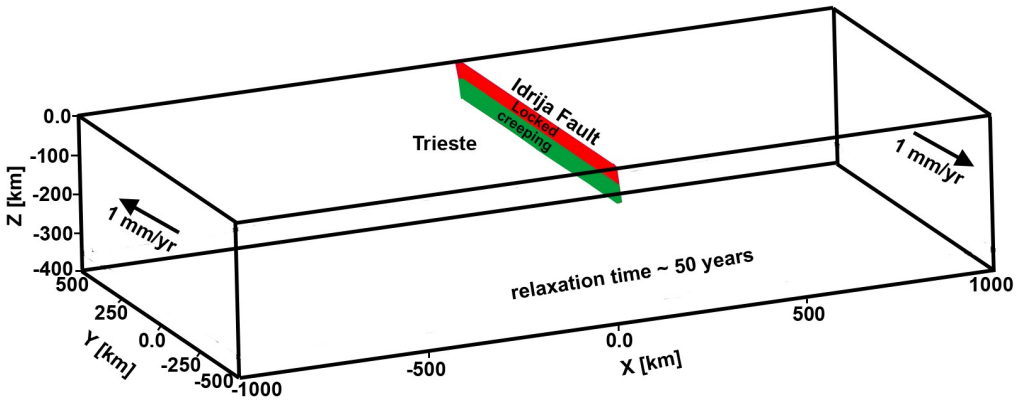

Figure 4.3: Geometry of the numerical model, where the fault is embedded in the elastic layer. Velocity boundary conditions prescribe a horizontal lateral velocity of 1mm/yr with no motion normal to boundary on two sides of the domain. We specify the slip rate ~2mm/yr on the creeping portion (i.e. green colour) of the Idrija fault. The locking depth is approximately 20km.

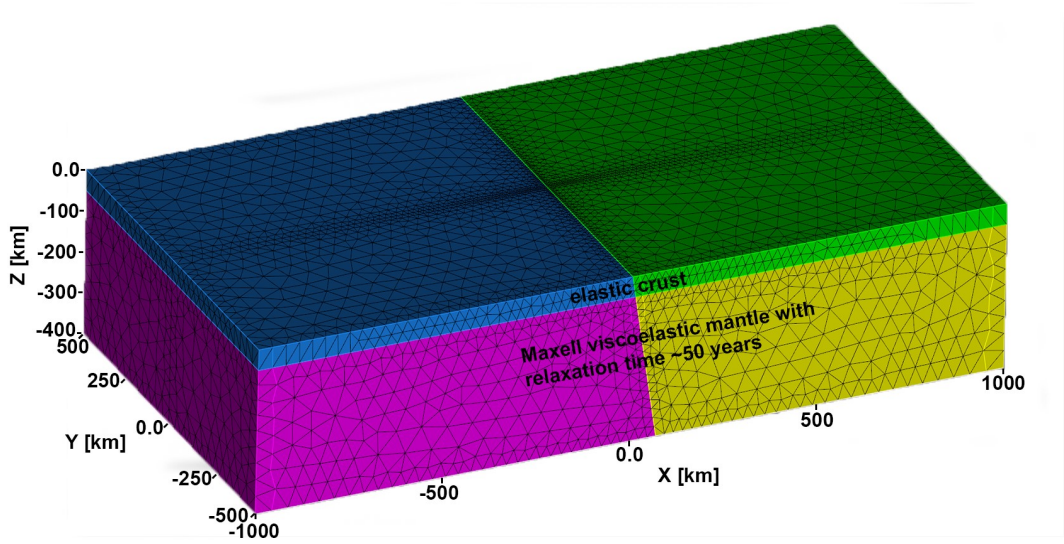

Figure 4.4: Tetrahedral finite element mesh with a discretization size of 6.7 km and increases in size with the geometric rate of 1.01 towards the sides. The colours correspond to the volumes in the Trelis geometry that are separated by the fault surfaces and boundary between elastic crust and Maxwell material with relaxation time ~50 years.

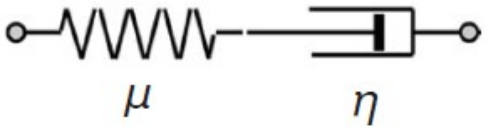

Figure 4.5: A Maxwell fluid model in which μ is the shear modulus and η is the viscosity of the material

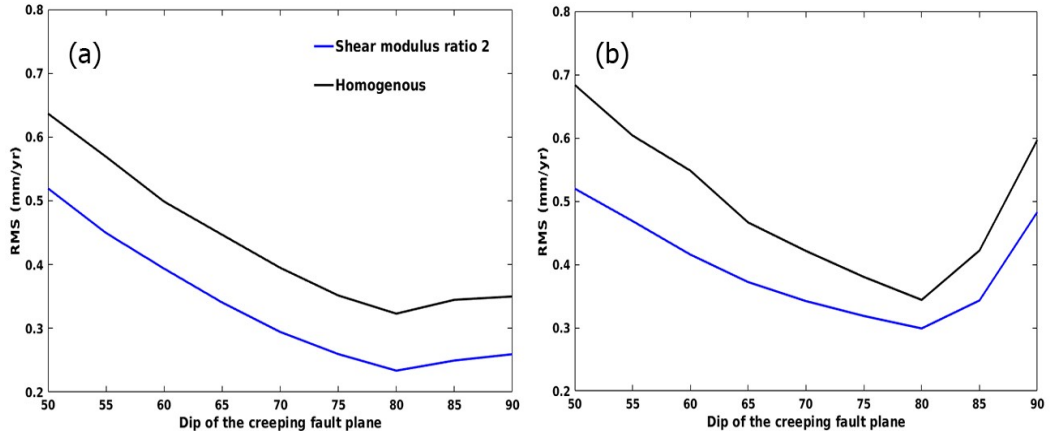

Figure 4.6: Sensitivity analysis of the geometry of creeping portion of the fault: a) ascending track and b) descending track for the case of homogenous and inhomogeneous elastic upper crust across the Idrija fault.

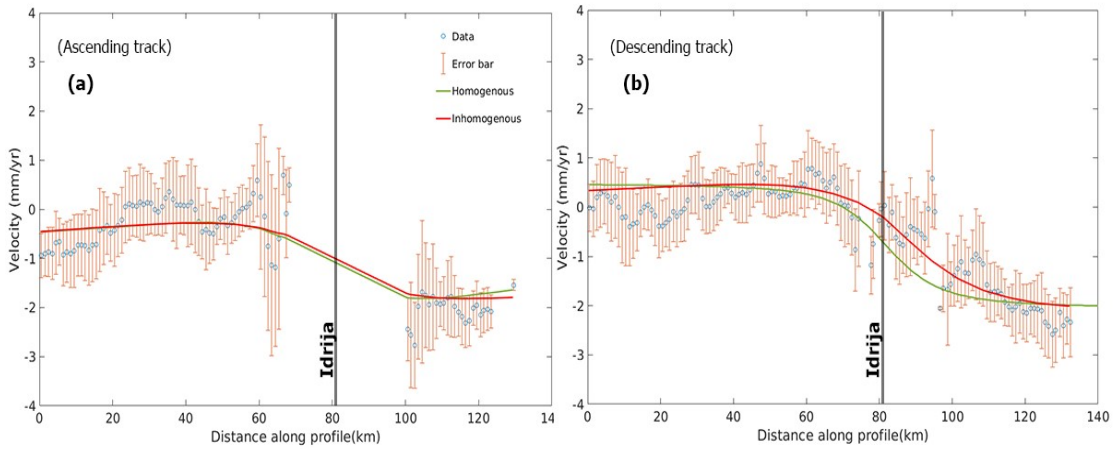

Figure 4.7: Average LOS velocities (blue circle) and vertical bar denote the errors of the point measurement. Solid vertical black line denotes the position of mapped Idrija fault. Solid red line is a theoretical model of strain accumulation due to creep along the 80 degree dipping portion of the fault at depth in the presence of lateral variation in shear modulus and solid green line is a theoretical model with 90 degree dip and homogenous elastic upper crust.

Chapter 5: Stress evolution at the junction between South-eastern Alps and western Slovenia and physics of the swarm activity in the Idrija fault system.

We model the time dependent Coulomb failure stress within the fault system in Northwestern Slovenia and Northeastern Italy including the effect of post-seismic deformation by visco-elastic relation of lower crust and mantle since the occurrence of 1511 Mw 6.8 earthquake on the Idrija fault. We use linear Maxwell rheology with Maxwell relaxation time of approximately 10 and 500 years in the lower crust and mantle respectively. Our results clearly show that 1511 earthquake loaded the central portion of the Rasa fault, which is approximately 30km away from the Idrija fault. We further demonstrate the time-dependent stresses induced by both earthquakes that ruptured on Idrija and Rasa faults are more favorable to partially load the 1976 Mw 6.5 earthquake in the Friuli region. In order to decipher the seismic hazard in this region, it is very important to include the effect of stress evolution within the fault system, as reflected by the occurrence of historical earthquakes on the major faults. On the basis of our results, we understand that the relatively high seismic strain accommodated within this slow deforming region (~2 mm/y) and the related clustering of earthquakes over a short time period of 500 years, are likely the consequence of redistribution of stresses within the fault system following the occurrence of the 1511 earthquake. We also evaluate the recent seismic activity between Idrija and Rasa faults during 2006-2016. We conclude that transients along the creeping section of the Idrija fault is the most favourable mechanism for both long and short term volumetric deformation between two locked faults.

5.1 Introduction

The 1511 Mw 6.8 western Slovenia earthquake occurred within the external Dinarides (see Fig. 4.1). The complex nature of the active tectonics of the region is mainly controlled by transpressional deformation (Moulin et al., 2016). The south-directed thrusting is dominant in the Alpine foreland of NE Italy and dextral strike deformation in western Slovenia. This region had already experienced several earthquakes with magnitude M>6 in the past 500 years. The series of earthquakes begin with a strike slip sequence in 1511. The main shock with Mw 6.8 occurred on Idrija fault (Fitzko et al., 2005). Ribaric (1979) argued about a doublet with a second earthquake of

magnitude Mw 6.5 or bigger. On May 6, 1976, an Mw 6.5 thrust fault event occurred in Friuli region (Aoudia et al., 2000). Twenty two years later, Ravne fault ruptured with magnitude Mw 5.8 (Bajc et al., 2001). The 2004 Krn earthquake with Mw 5.2 is the last moderate size event that took place in the region (Borghi et al., 2009; Ganas et al., 2008). The focal mechanism solutions of the Mw 5.8 and Mw 5.2 earthquakes were strike slip events. In chapter 4, we model the surface deformation across the Idrija fault system and demonstrate that Idrija fault is locked up to 18 km depth and accumulates strain at a rate of 2mm/yr. Vičič et al. (2017) performed a study on the microseismicity within the Idrija fault system with a high resolution detection of smaller magnitude events that occurred between 2006 and 2016. The authors detected a burst of swarm activity during the time period between October, 2009 and December, 2010 (see Fig. 5.1). Another study (Gosar et al., 2011) using extensometer measured strains with a reported subsidence of the order of 0.06 mm between late October 2009 and early January 2010, followed later on by uplift during early July 2010 (Fig. 5.1).

Stress triggering mechanisms are widely used for both triggering of aftershocks sequences and earthquakes in different tectonics setting worldwide (Reasenberg and Simpson, 1992; Stein et al., 1992; King et al., 1994; Stein et al., 1997; Harris, 1998; Toda et al., 1998; King and Cocco, 2001; Steacy et al., 2005; Javed., et al., 2015; Borghi et al., 2016). Similar works in our study region considered the instantaneous response of only 1998 Bovec event to 2004 Krn earthquake (Ganas et al., 2008) or accumulated effect of both static and visco-elastic stress transfer due to 1511 Idrija , 1976 Friuli and 1998 Bovec earthquakes on 2004 Krn earthquake (Borghi et al,. 2009). In this study, we additionally take in to account the effect of newly evident Rasa fault earthquake in the time dependent stress evolution model. We also test the Coulomb failure criterion for the recent seismic activity in the Idrija fault system.

5.2 Methodology

In recent decades, several mechanisms of earthquake triggering have been proposed to explain patterns of both far-field and near-field triggered seismicity before and after earthquakes. Here we only focus on triggering mechanisms which are relevant to this chapter.

A static stress change from large earthquake alters the stress state along the neighbouring faults, and can trigger moderate to large size earthquakes (Harris and Simpson, 1992; Stein et al., 1992; Reasenberg and Simpson, 1992; King et al., 1994). According to this theory, each earthquake releases stress on the fault that slips but transfer the stress elsewhere. In this framework, faults with certain orientation and preferential slip direction fail when Coulomb failure stress (ΔCFS) is positive.

According to eq. (2.4) and (2.5), fault clamping and unclamping which strengthens and weakens the faults respectively and will also increase with time in both cases. Therefore, fault unclamping will enhance the seismic activity and clamping will suppress it.

In addition, static stress transfer occurs instantaneously and thus cannot easily explain the time delay of subsequent triggering from years to decades without incorporating it in to rate and state dependent frictional models (Stein et al., 1997; Parsons et al., 2000). Aoyama et al. (2002) showed that spatiotemporal distribution of 1998 Hida Mountains swarm activity is correlated with the static stress changes. To model the spatiotemporal distribution of swarm activity within Idrija fault system, we estimate the changes in the stress state induced by creeping of Idrija fault at the rate of approximately 2mm/yr along the strike and dip direction and then compare the results with spatial distribution of swarm activity.

Time dependent stress transfer mechanism following a large earthquake, last from decades to hundreds of years, because of visco-ealstic relaxation of the lower crust and upper mantle. The triggered earthquake may generate diffusive visco-elastic fronts within the upper mantle that slowly increase or decrease ΔCFS in the surrounding crust. This mechanism of stress transfer has been used to explain the delayed triggering of the Hector Mine earthquake seven years after the Landers earthquake (Freed and Lin, 2001; Zeng, 2001; Pollitz and Sacks, 2002) and likewise earthquake triggering along the North Anatolian fault (Lorenzo-Martın et al., 2006; DeVries et al., 2016).

In a generalized viscoelastic body with elastic compliance tensor D_{ijkl} , the total strain rate tensor $\dot{\varepsilon}_{ij}$ is the sum of elastic strain and inelastic strain.

$$\dot{\varepsilon}_{ij} = \dot{\varepsilon}^{e}_{ij} + \dot{\varepsilon}^{i}_{ij} \quad (6.1)$$

Where dot represents the time differentiation. In case of linear elasticity, the stress-strain tensor relation can be written as

$$\dot{\varepsilon}^{e}_{ij} = D_{ijkl}\dot{\sigma}^{e}_{kl} \quad (6.2)$$

Where σ_{ij} is the Cauchy stress tensor. In case of linear Maxwell rheology, time dependent strain rate can be defined as

$$\dot{\varepsilon}^{i}_{ij} = \dot{\gamma}\frac{\dot{\sigma'_{ij}}}{\mu} \quad (6.3)$$

Where $\dot{\gamma}$ is an inverse of Maxwell relaxation time and σ'_{ij} is the deviatoric stress tensor.

Assuming infinitesimal strain, combining eq. (6.1), (6.2) and (6.3) and integrating, we can obtain the equation of stress evolution:

$$\sigma(t) = C_{ijkl}\varepsilon_{kl}(t) + \dot{\gamma}\int_0^t C_{ijkl}\dot{\varepsilon}^{i}_{kl}(t)dt \quad (6.4)$$

Where C_{ijkl} is the elastic moduli tensor.

We consider a rectangular grid with dimesnion 256 km by 256km by 128km. The computational grid is divided in to 512 nodes in the three directions. The computational domain is composed of 16km thick elastic upper crust, a visco-ealstic lower crust with 10 year Maxwell relaxation time between a depth of 16km and the Moho at 37km and a visco-ealstic mantle with 500 year Maxwell relaxation time. The domain is extended approximately 100km away from the most external point of each fault.

We have modeled co-seismic and post-seismic (visco-ealstic relaxation) stresses using open source Relax code developed for earthquake cycle modeling including co-seismic Coulomb failure stress calculation, and quasi-static stress transfer between earthquakes due to a post-seismic transient. This numerical code is based on a Fourier-domain elastic Green's function (Barbot et al., 2009b; Barbot and Fialko, 2010a) and on an equivalent body-force representation of co-seismic and post-seismic processes (Barbot et al., 2009a; Barbot and Fialko, 2010b).

5.3 Time dependent stress evolution since 1511 events

To investigate the full range of time dependent stress evolution pattern, we run several simulations with one shock, the 1511 Mw 6.8 Idrija earthquake (Model A) and two shocks, the Idrija and Rasa earthquakes (Model B) on different known receiver fault geometries. Lists of seismogenic sources used in this study are shown in Table 5.1.

5.3.1 Time dependent ΔCFS resolved on the Rasa Fault

We first compute the 1511 Mw 6.8 earthquake's induced $\Delta CFS(t = 0)$ at depth of 7km and on Rasa fault plane. We choose a fixed receiver fault geometry (Strike 310, dip 80, rake 176). Results are shown in figure 5.2. It clearly shows the increase in stress along both tips of the rupture plane and a decrease over the Predjama fault. It is also shown that ΔCFS > 0.01 MPa are observed at the centre portion of the Rasa fault. We also run the sensitivity test with varying coefficient of friction from 0.2 to 0.8. ΔCFS increases between 0.01 and 0.09 MPa immediately after the occurrence of 1511. An average 1.7m displacement with a maximum displacement reaching 2m has been recently measured along 19 km length on the Rasa Fault (Foroutan et al., 2017). Accordingly, the magnitude of the earthquake using Wells and Coppersmith scaling laws will be ~ Mw 7.0 and this relying on the average slip. An intensity map revised by Camassi et al. (2011), clearly shows the wide extent of damage in the region (see Fig. 5.3). This cannot be explained by a single event that either occurred on the Idrija or Rasa fault. On the basis of field evidence (Foroutan et al., 2017) and intensity map of the region (Camassi et al., 2011), we perform scenario based calculations extending both the fault rupture length from 19 to 70 km and magnitude between 6.5 and 7.0.

5.3.2 Time dependent ΔCFS resolved on the 1976 Friuli earthquake

In figure 5.4 and figure 5.5, we show a map of ΔCFS on faults with the same orientation and mechanism as the 1976 Friuli earthquake, due to the cumulative effect of the 1511 earthquake and also both 1511 and Rasa earthquakes. We vary the apparent coefficient of friction from 0.1 to 0.8 and find that ΔCFS estimated maximum is with $\mu' = 0 \cdot 1$. We run the rest of computations

assuming $\mu' = 0 \cdot 4$ as serveral studies use this value for earthquake triggering. The model A loads the stresses on the 1976 earthquake in the range of [-0.002, 0.002MPa]. For the case of Model B, we assume three different rupture lengths for the Rasa earthquake (i.e. 18.5km, 50km and 70km). ΔCFS estimate (~0.0004 to 0.005 MPa) with smallest rupture length, (~0.007 to 0.017MPa) with 50km length and (~0.02 to 0.06 MPa) for the largest length. For the case of largest rupture length, on average, $\Delta CFS(t = 0)$ calculates ~0.018 MPa and cumulative visco-elastic ΔCFS computes ~0.031 MPa.

5.3.3 Accumulated ΔCFS in the region since 1511 earthquake

Figure 5.6 demonstrate the estimated values of the cumulative effect of the1511 Idrija fault earthquake, the Rasa fault earthquake and the 1976 Friuli earthquake on the optimal fault plane for 1998 earthquake and also combining the effect of 1998 on 2004 earthquake's optimal fault plane. Prior to 1998 earthquake, ΔCFS is between -0.003 and 0.07 MPa with a mean value of 0.05 MPa. ΔCFS estimates on the 2004 earthquake's fault plane appear to be negative after the occurrence of 1998 earthquake.

5.4 Physics of swarm Activity in the Idrija fault system

We estimate the Idrija fault's creep induced changes in shear stress, normal stress and Coulomb stress at 15km depth. The results are shown in figures 5.7 and 5.8.

We estimate ΔCFS > 0.01 bar in the region, where swarm activity occurred. Thus, the creeping of the Idrija fault at a rate of 2mm/yr provides a ΔCFS > 0.01 bar/year. Assuming the same creeping rate ΔCFS becomes greater than 0.1 bar after a decade. Figure 5.7 depicts the shear and normal stress changes are negative and positive respectively at the location of Postojna extensometer (Gosar et al., 2011) and surrounding region indicating that unclamping of fault are the more favourable mechanism for the overall seismic activity during 2006-2016. This is also evident in the cross sections across the Idrija fault system (Figs 5.9 and 5.10). A cartoon diagram of the mechanisms is shown in figure 5.11. The Postojna extensometer recorded subsidence and uplift could be the result of downward and upward motion of the block B either along the Idrija fault or

Predjama fault at depth. The downward motion of the Block B is the consequence of the increase in vertical stress ($\sigma_v - \Delta p_h$) due to extraction of fluid at depth, in which $\sigma_v = \rho g h$ and Δp_h is the change in hydrostatic pressure. This creates a pressure gradient at depth, so the pore pressure will tend to increase in those regions where pore pressure decreased and coincides with the swarm activity. The pore pressure diminishes and vertical stress ($\sigma_v + \Delta p_h$) decreases with time and reaches equilibrium followed by an upward motion of block B.

5.5 Discussion

Since the rupture of 1511 earthquake, several patches within the fault system in the region experienced positive Coulomb failure stresses. Ribaric (1979) suggested the occurrence of two large earthquakes in the region in the same day. Paleoseismological evidence (Foroutan et al., 2017) clearly suggests that Rasa fault also ruptured at the time of 1511 earthquake as historical evidence do not mention any moderate size earthquake after a delayed time period after 1511 (Ribaric, 1979; Camassi et al., 2010). Figure 5.2b shows ruptured portion of the Rasa fault (18.5 km), which has clear field evidence of surface rupture, experienced positive stresses. Using the apparent frictional coefficient value equal to 0.4, $\Delta CFS(t = 0)$ estimates (-0.019 and 0.018MPa) with 70% positive stresses on the fault rupture length. The maximum surface displacement observed along the Rasa fault correlates well with the maximum Coulomb failure stresses. The magnitudes of a stress increase of ≥ 0.1MPa are considered reasonable values for triggering earthquakes (Harris et al., 1995; King et al., 1994). At stress changes ≥ 0.02 MPa, Reasenberg and Simpson (1992) found the largest correlation of seismicity and positive stress changes along fault segments in Central California due to Loma Prieta earthquake. However, for stress changes ≤0.01 MPa, the correlation between seismicity and positive stress changes is weak and unclear (Reasenberg and Simpson, 1992; Harris, 1998; Harris and Simpson, 1996; DeVries et al., 2016). The south-directed thrusting in the Alpine foreland of NE Italy is accommodated at a rate of ~1-2 mm/year. Such a small slip rate approximately provides ΔCFS of ~ 0.002 bar/year. During 465 years, on average ΔCFS estimates 0.09 MPa due to plate motion or local gravity heterogeneities. On the fault plane of 1976 Friuli earthquake, ΔCFS is on average estimate ~-0.0003MPa and ranges from ~0.005 (i.e. rupture length 18.5km) to 0.06 MPa (i.e. rupture length 70 km) as shown

in figure 5.4, due to Models A and B respectively. Static Coulomb failure stresses are negligible on the 1976 earthquake's fault plane using both models as the optimal fault plane is far away from the epicenter of the Idrija fault due to decay of stresses as $1/r^3$ from a finite source in an homogenous elastic half space (Okada, 1992). Visco-elastic relaxation can also increase the Coulomb failure stresses on the faults, which are far away from the main events and promote the seismic activity along it. Our results suggest that visco-elastic relaxation increase the Coulomb failure stresses of the order of 2-3 times larger than the static coulomb failure stresses on the 1976 Friuli fault plane and brought the fault close to failure (See figure 5.5). Previous studies that modeled the visco-ealstic relaxation also estimated a similar increase in Coulomb failure stresses (Pollitz et al., 2003; To et al., 2004; DeVries et al., 2016). Similar to previous fault segments, ΔCFS estimate of ~0.05 MPa along the 1998 earthquake fault also indicated that stress redistribution caused by 1511 earthquakes promote the seismic activities on nearby and far segments in this region. Assuming the simple Maxwell relaxation rheology, simulation results show that 1511 earthquakes cumulative stress change induced by both coseismic and postseismic deformations will increase the loading rate on the 1976 and 1998 earthquake's faults with 30% to 50%. On the 2004 earthquake's fault plane, the cumulative effect of all earthquakes with magnitude $M_w \geq 5.5$ since 1511 earthquake, provide positive Coulomb failure stresses prior to 1998 earthquake and becomes negative after 1998 earthquake. Woessner et al. (2012) suggested that information of correlated uncertainties of finite-fault source models can change the stress changes near the faults. Figure 5.6c clearly shows the region of increased Coulomb failure stresses along the southeast tip of the Idrija fault and our recent study also demonstrate that portion of the fault is locked and is being loaded at a rate of 2mm/year along both strike and dip direction (Figure 4.7, Chapter 4). Similarly, a lobe of increased Coulomb failure stress greater than 0.02 MPa towards the northwest direction of 1976 Friuli earthquake as shown in figure 5.6d, can cause a serious hazard in the area.

Idrija fault seems like driving much of the deformation on a long time scale and modelling of Coulomb failure stress within a short time span, induced by the creeping of Idrija fault beneath the locked portion, correlates well with the seismic activity during 2006-2016.

5.6 Conclusions

In this chapter we show that stress evolution modeling within a fault system is of paramount importance in understanding both the continental deformation and the seismogenic potential. At the scale of the earthquake cycle the interaction between active faults is controlling the earthquake distribution in space and time. Coseismic and interseismic deformations on Idrija fault system are leading the deformation within the last 500 years at the junction between the southeastern Alps and the external Dinarides. Specifically visco-elastic relaxation of the mantle following the 1511 earthquake sequence play an important role in partial loading the 1976 Friuli earthquake fault. On a short time scale creeping beneath the locked portion of Idrija is unclamping the region and this seems to be a viable mechanism that explains the occurrence of earthquake swarms in the region.

Table 5.1: Slip model of individual seismogenic sources of northeastern Italy and western Slovenia**.**

Serial No.	Name	Latitude	Longitude	Length (km)	Width (km)	Depth (km)	Strike (o)	Dip (o)	Rake (o)	Average slip (m)	Mw
1.	Idrija	46.14	13.77	50.0	12.6	1.0-13.4	310	80	176	1	6.8
2.1 2.2 2.3	Rasa	45.67	14.09	18.5 36.0 50.0	12.6	1.0-13.4	310	80	176	1	6.5 6.7 6.8
3. 3.1 3.2 3.3	Friuli Aft. 1 Aft. 2 Aft.3	46.24 46.26 46.25 46.23	13.03 13.13 13.16 13.23	16.0 10.0 8.0 6.0	9.0 6.4 5.5 4.5	2.0-6.5 6.5-10.2 2.0-5.2 2.0-4.3	290 276 274 277	33 35 35 30	105 110 90 90	1.32 0.75 0.83 0.46	6.5 6.1 6.0 5.7
4	Bovec-Krn	46.32	13.61	13	7.0	3.3-9.9	313	82	171	0.18	5.8

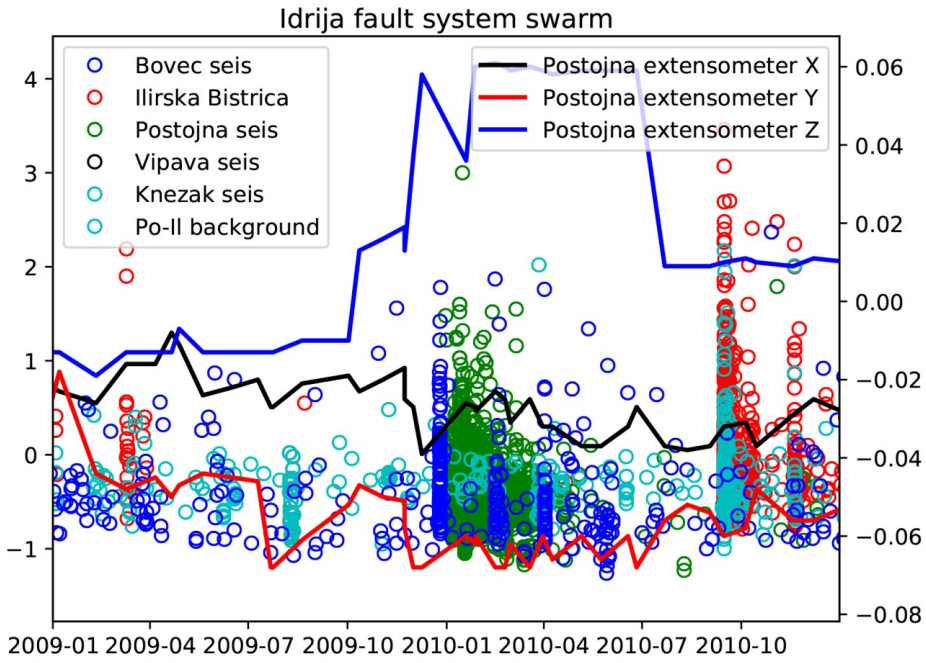

Figure 5.1: High resolution detection of the seismic activity during 2009-2010 is computed by Vičič et al. (2017). A green circles represent the swarm activity during early Jan to April 2010. The blue bold line shows the vertical displacement at the surface. The positive value depicts the subsidence.

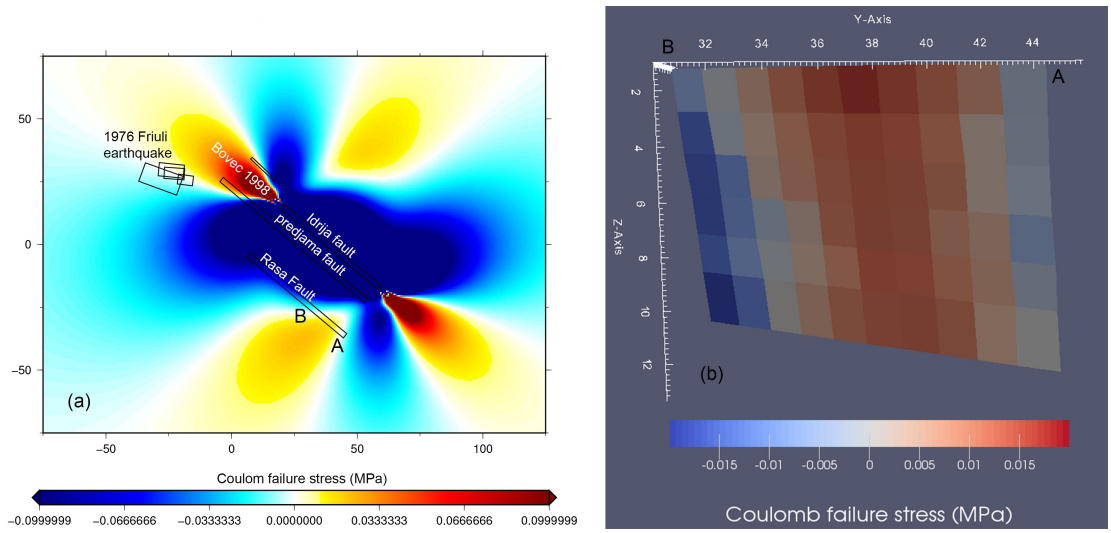

Figure 5.2: ΔCFS computed a) at 7 km depth and b) along Rasa fault plane using fixed receiver fault mechanism (Strike~310^0, dip~80^0 and rake~176^0). We assumed $\boldsymbol{\mu} = \mathbf{0} \cdot \mathbf{4}$ in this case. Here AB represents the portion of Rasa fault segment, which shows evidence of 1.7m average surface displacement (Foroutan et al., 2017).

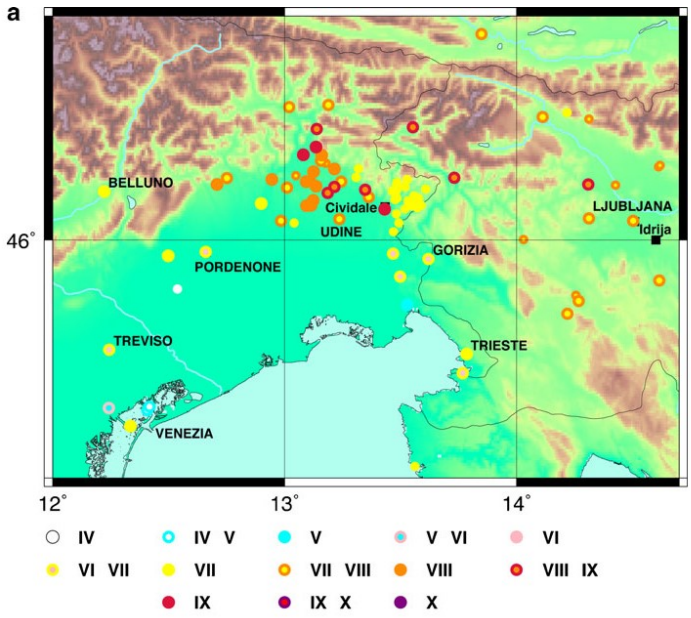

Figure 5.3: A revised intensity map of the region after the occurrence of the 1511 earthquake by Camassi et al. (2011).

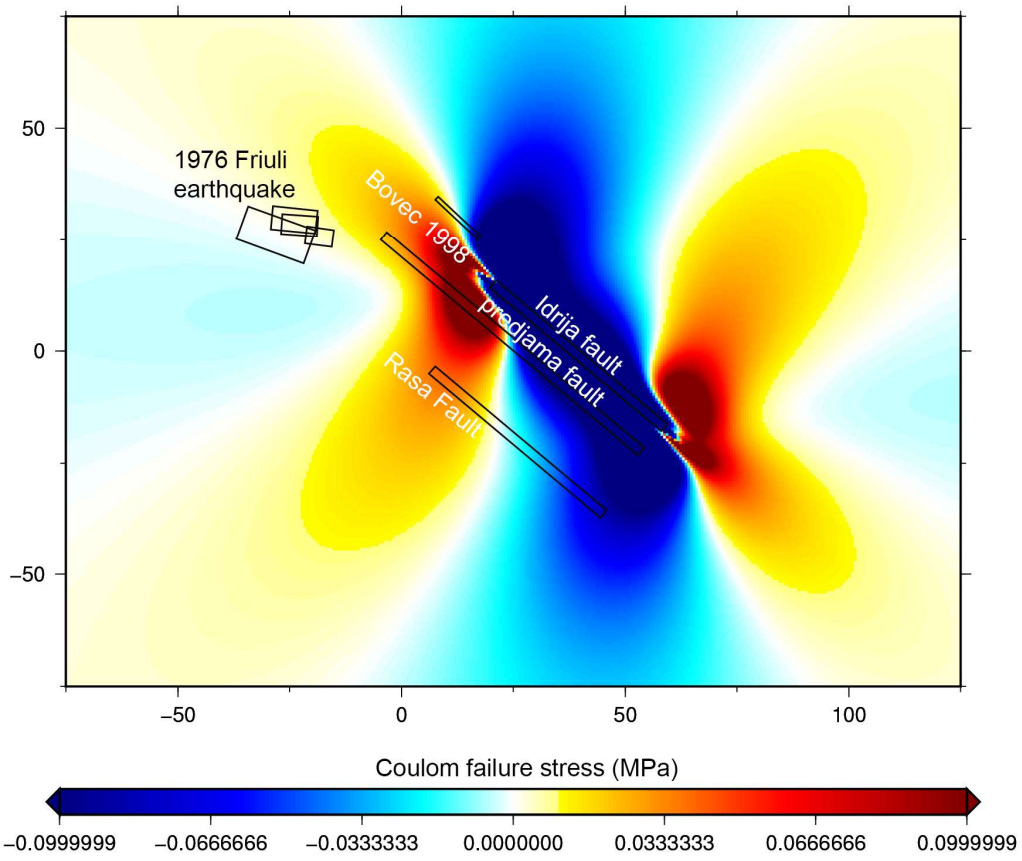

Figure 5.4: Snap shot of Cumulative ΔCFS estimated at 6km depth using 1511 earthquake on Idrija fault. Focal mechanism of 1976 earthquake is provided as a receiver fault mechanism with $\boldsymbol{\mu' = 0 \cdot 4}$. Results are shown just before the occurrence of 1976 earthquake.

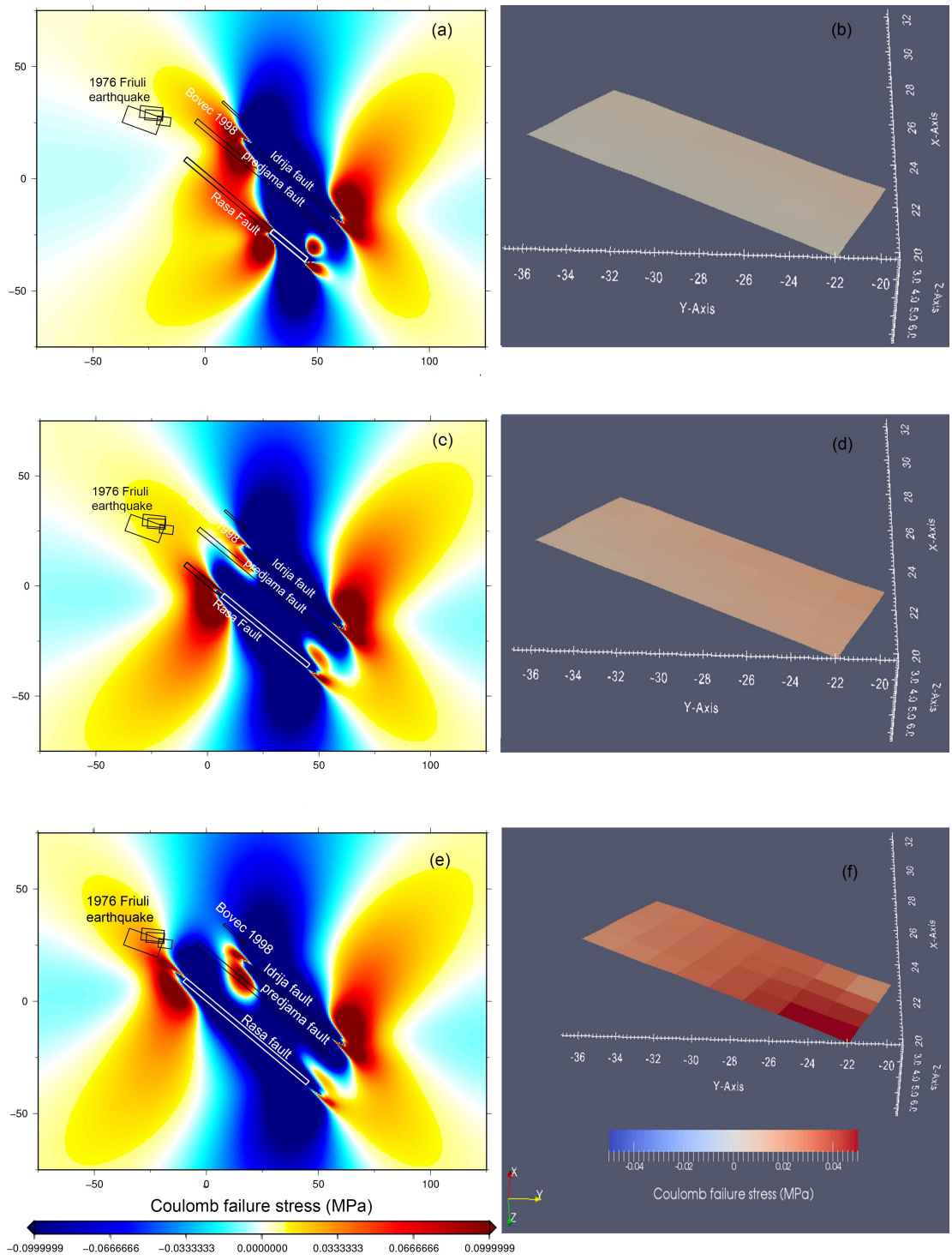

Figure 5.5: Assuming two 1511 events, one along Idrija fault and other on Rasa fault, snap shot of cumulative ΔCFS are shown at 6km depth and on the 1976 Friuli earthquake's fault plane for different lengths with different rupture lengths; a, b) L=18.5km, c,d) L=50km and e,f) L=70 km. The white rectangle shows the portion of the fault rupture.

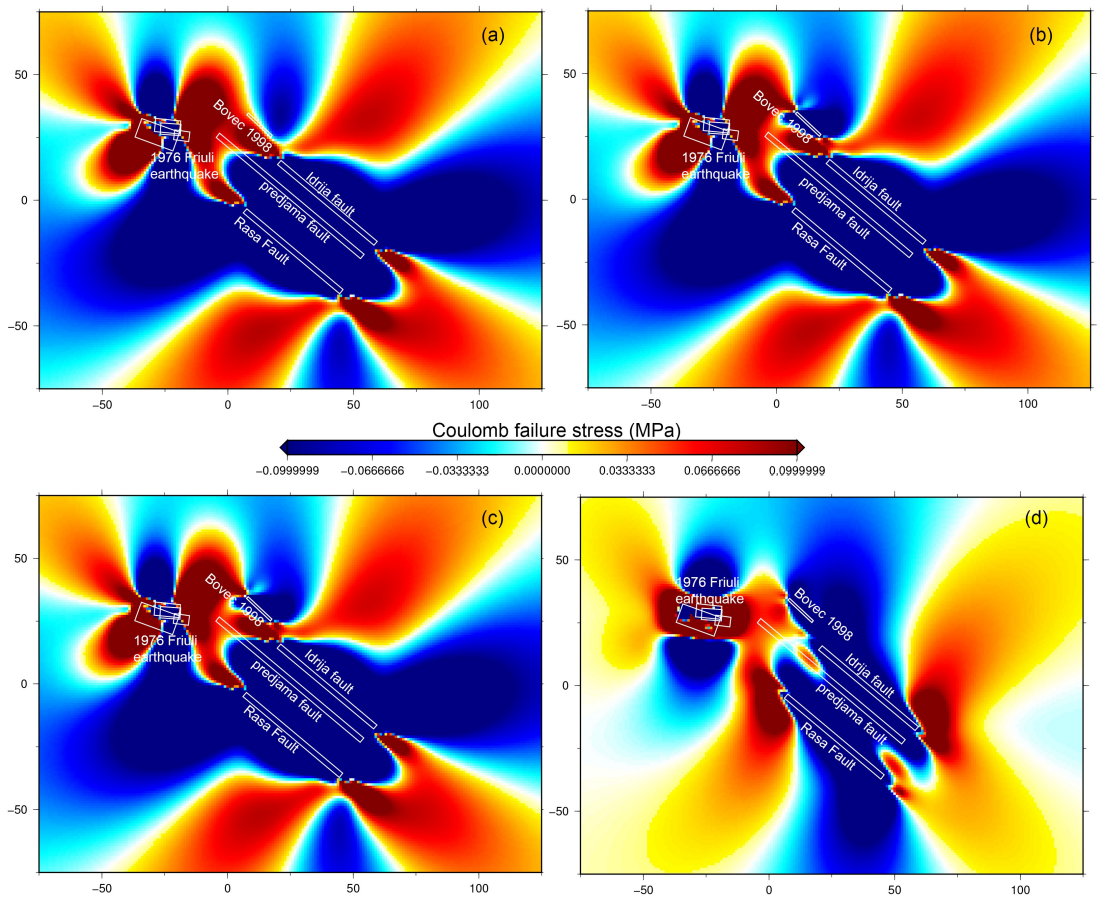

Figure 5.6: Since the occurrence of two 1511 earthquakes, snap shot of the time dependent Coulomb failure stresses are shown: a) before the 1998 Bovec earthquake, b) before 2004 Krn mountain earthquake, c) after 2030 assuming dominant fault geometry of Idrija fault system as a receiver fault, and d) after 2030 provided south-directed thrust fault with dip angle 30 degree as receiver mechanism.

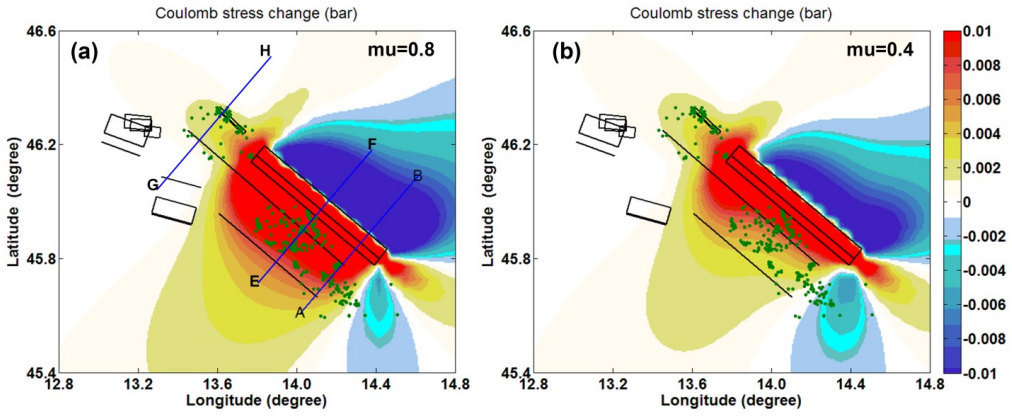

Figure 5.7: ΔCFS are computed at 15km depth assuming a) $\mu' = 0 \cdot 8$ and b) $\mu' = 0 \cdot 4$. The green dots represent the recent swarm activity during 2006-2016.

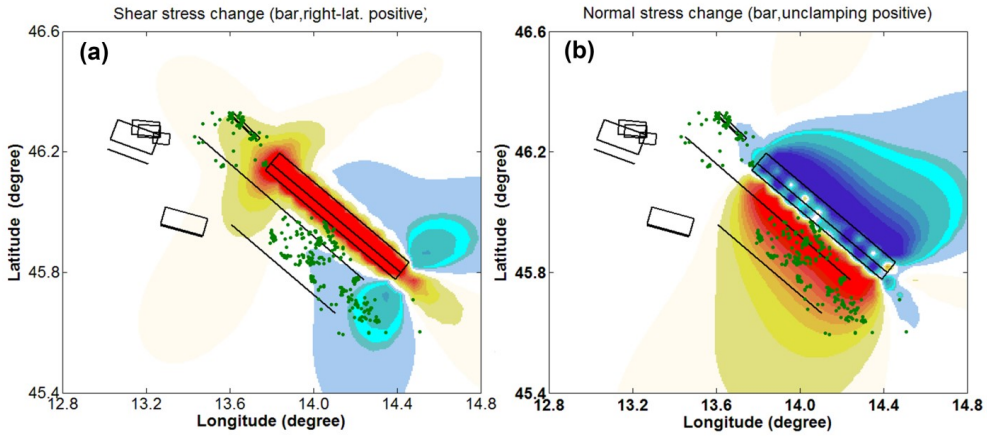

Figure 5.8:a) Shear stress changes, b) normal stress changes are computed at 15km depth, where green dots represent the recent swarm activity during 2006-2016.

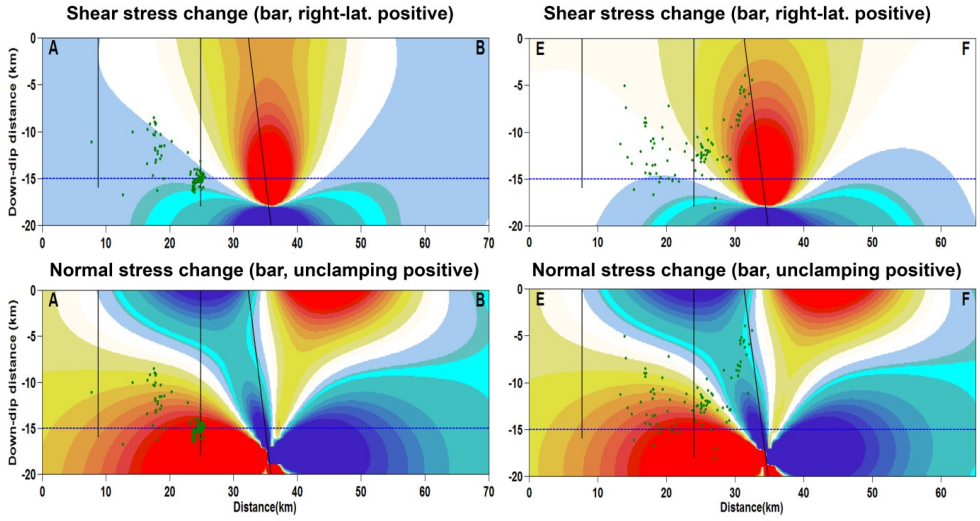

Figure 5.9: The cross sections AB and EF show the normal and shear stress changes across the Idrija fault system. The black and blue lines represent the position of the faults and computed stress changes at 15km depth respectively. The location of cross sections AB and EF are shown in figure 5.6a.

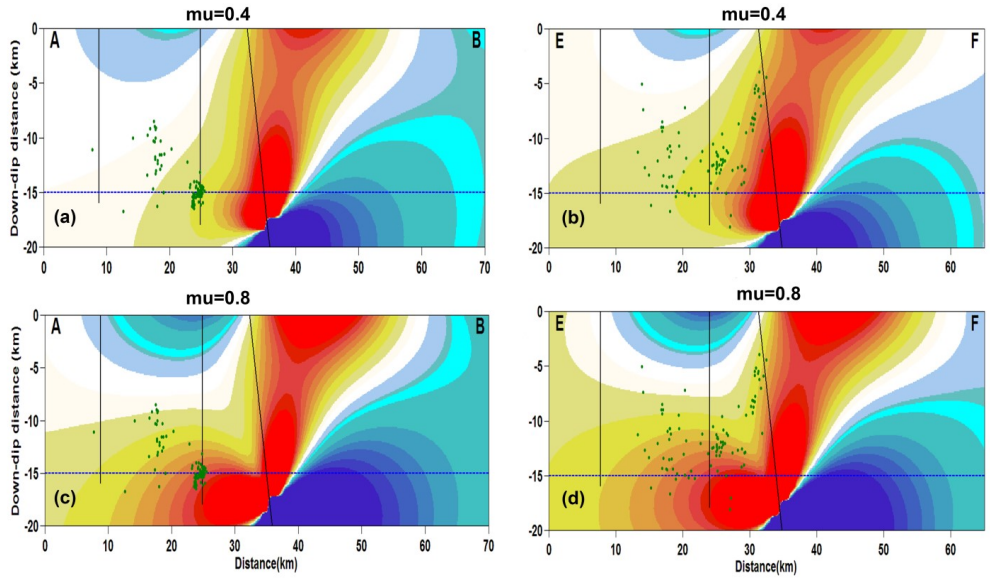

Figure 5.10: The cross sections AB and EF show the Coulomb failure stress changes across the Idrija fault system. The black and blue lines represent the position of the faults and computed stress changes at 15km depth respectively. The location of cross sections AB and EF are shown in figure 5.6a.

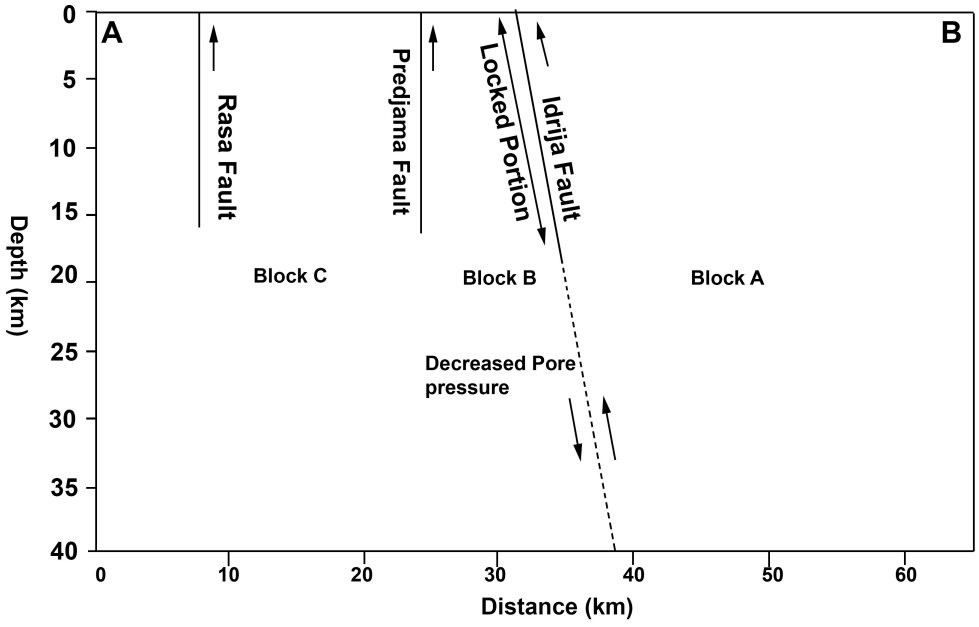

Figure 5.11: Geological Cross Section perpendicular to the average strike of the Idrija fault system along the profile AB shown in figure 5.6a. The geometry of the creeping along the Idrija fault at depth is adapted from Wang et al. (2017).

Chapter 6: Dynamics and mechanics of the lithosphere: The Adria and surrounding belts.

We model the flow field over the Adriatic microplate and surrounding belt using variable density data, converted from well resolved shear wave velocity data. Recent ambient noise seismic tomography reveals a thick lithosphere beneath the Adriatic Sea. We demonstrate that the slow E-W extension across central Italy and the contraction in the southeastern Alps are dominated by the buoyancy forces due to density contrast between thick lithosphere beneath the Adriatic Sea and the underlying asthenosphere. We did not rule out other possible mechanisms such as gravitational potential energy due to lateral density variation within the crust, and north-south convergence between Africa and Eurasia, but our numerical results demonstrate that there effects might be secondary in terms of present day deformation. We show that our model predicts the northward movement of Adria microplate beneath the Southeastern Alps. Our simple model predicts reasonably well also the GPS velocity field at the surface.

6.1 Introduction

The central Mediterranean is a part of a complex plate boundary between Africa and Eurasia (Anderson and Jackson, 1987; Nocquet and Calais, 2004)and the deformation is mainly dominated by extension in Italy and contraction in the Southeastern Alps and Dinarides. According to Anderson and Jackson (1987) the Adriatic region in the central Mediterranean is relatively aseismic, circumscribed by the Apennines, the Southern Alps, and the Dinarides. The N-S convergence between Africa and Europe is accommodated by different geodynamic processes mainly related to: i) the northward movement of Adria microplate beneath southern Alps; ii) subduction/sinking of the Adria lithosphere beneath the Apennines and Adriatic Sea; and iii) Adria microplate rotation with respect to stable Europe (Anderson and Jackson, 1987; Dewey et al., 1989; D'Agostino et al., 2008). From these previous studies based on geological, seismological and geodetic data it is still unclear how the Adriatic region affects the present day deformation rate in the central Italy and south eastern Alps. These studies likely imply that part of the motion of the

Adriatic region may be independent of the external forces imposed by the two major plates namely Africa and Eurasia. Indeed the first studies in the Mediterranean that started investigating the contribution of non-external forces to the active deformation through both a 2D section through the Italian Peninsula (Aoudia et al., 2007) as well as a 3D model of the Central Mediterranean region (Ismail-Zadeh et al., 2010) showed clearly that buoyancy forces represent an important component of the geodynamics of the region.

This study is based on a very recent Earth structure model computed for the Adriatic region using high resolution ambient noise tomography (Kherchouche, 2017).This study provides a 3D shear-wave velocity model on a grid of 0.5 x 0.5 degree cells in the study region. The main results reveal a thick and deep lithosphere beneath the Adriatic Sea as shown in the cross section along the Adriatic Sea (See figure 6.1). In this work, we use the finite-element Pylith code and include the effect of body forces on vertical direction to compute the buoyancy driven flow due to density contrast between thick lithosphere and asthenosphere. Pylith provides the option to output the weighted average of both the displacements and velocities within a cell .The weights are determined from the quadrature associated with the cells. We discuss the different geodynamical process over the central Apennines, southeastern Alps, Adriatic Sea and Dinarides. We also compare the predicted flow vector field with the observed SW-NE extension (Chiaraluce et al., 2004; D'Agostino et al., 2001; Piccardi et al., 1999) across the Appenines and N-S shortening in the Southern Alps (Benedetti et al., 2000; D'Agostino et al., 2005). Before running the full 3D simulations, we first test a 2D buoyancy driven flow due to density contrast and compare the simulation results with the results presented by Aoudia et al. (2007).

6.2 2D-Gravity driven Flow

6.2.1 Description of the Numerical Model

In the work of Aoudia et al. (2007), the authors modelled the contemporary flow and stress distribution in the lithosphere beneath Central Italy. They concluded that the present day extension and contraction in Central Italy is the result of buoyancy forces due to distribution of heterogeneous density in the lithosphere. In order to compare the result, we build a similar 2D model mesh using

Trelis software (www.csimsoft.com/trelis). Trelis is a geometry and mesh generation toolkit. It provides several commands to construct both two and three dimensional geometry of the model. We use “surface” command to create the model domain with a dimension of 437 km wide by 427 km deep. Each surface is defined by polynomial curves linking the point in both horizontal and vertical direction. We subdivide the model domain into two surfaces using “split” command. Once the dicretization size of the mesh has been defined, Trelis offers different schemes to generate the mesh, depending on the geometry of the object to mesh and different quality metrics to assess the mesh’s quality. We discretize the model domain using quadrilateral cells with a nominal cell size of 5.0 km. In order to identify the different materials of the model, we need to define the blocks within a Trelis. Each block represents a part of the model with a specific material property (e.g. elastic and Maxwell theology). At the end, we add the node on curves defining the outer boundary of the domain. Boundary conditions can be assigned to these nodes set within a Pylith. In this problem, we use a 15km thick elastic layer over a linear Maxwell viscoelastic half-space, filled by several viscous layers similar to the model of Aoudia et al. (2007). We apply Dirichlet boundary conditions to constrain the displacement normal to the boundary (i.e. zero displacement normal to the boundary). Our model is slightly different from the previous model as we did not consider the sticky air above the surface. We used 3.e+21 Pas as the viscosity of the lithosphere lid with Maxwell relaxation time equal to ~3200 years. For other principal layers, we assumed the viscosities of 5.e18 Pas (i.e. 0-150km distance and 30-50km depth) and 1e.20 Pas for a mantle wedge and mantle respectively. The Maxwell relaxation time for a mantle wedge and mantle are approximately 5 and 100 years respectively. The numerical modeling is performed with Pylith-finite element code. The description of the mathematical equations and linear Maxwell rheology is discussed in section 4.1. The initial stresses are computed from the following relation

$$\sigma_{zz} = \rho_i g h \qquad (6.1)$$

Where ρ_i represent the background densities of the layers (i.e. upper crust, lower crust and mantle etc), g is the gravitational acceleration and h is the depth of the layer. As it is mentioned in the Pylith 2.1.4 user manual (page 161), an initial hydrostatic stress equal to average lithosphere as a function of depth, is used to prevent the large initial displacement when gravity is “turned on”. We

specify ρgh as the initial stress state (i.e lithostatic) to all normal stress components, which is an appropriate condition for many tectonic problemsin the absence of tectonic stresses. This initial condition mimics the theoretical framework of McGarr (1988).

6.2.2 Model Results

We perform several simulations on 12 processors of parallel computer with different viscosities similar to Aoudia et al. (2007) and also with a simple Maxwell rheology consisting of a two layer model. For the later model, we prescribed 3.e+21 as the viscosity for both mantle wedge and lithosphere lid and 1e.20 viscosity to the mantle. We run the simulations for 10000 years. Figure 6.2 shows the snap shot at time 3200 years. The result of the former model as shown in the figure 6.2a depicts flow velocities of 4.0 cm/year in the lower crust due to the low viscosity and velocities reach 1.5 mm/year near the surface. But the flow field predicted by Aoudia et al. (2007) estimated 3.5 mm/year flow velocities within the lower crust. However, our model captures the downward flow motion due to sinking of a denser lithosphere lid and horizontal eastward flow field within the low velocity mantle wedge that decouples the crust from the mantle, similar to the results demonstrated by Aoudia et al. (2007). For the case of the 2-layer visocosity model, the flow field is of the order of 3.0 mm/year near the surface and predict others key features of the study area. The simulation result is shows in figure 6.2b. We did a sensitivity test for the initial stresses for an isotropic overburden pressure of the model.

Now, we build a 3D model as described in the next section, keeping a simple 2-layer viscosity model.

6.3 Data and Numerical Model

The study area covers the Adria microplate and surroundings with a depth of 200 km. Kherchouche (2017) computed the shear wave velocities using cross correlation of observations of 4 year time-sequences of ambient noise to extract Green's functions. Author computed the velocities on a grid (0.5^0 x 0.5^0), resolving objects with a size of less or equal 100km in the Adriatic Sea. The analysed group velocity dispersion curves range from 5s to 45s (delineate the structure up to 50km depth)

and phase velocity curves range from 20s to 100s (explore the structure from 50km to 200km), are appropriate to resolve the Shear wave velocity structure down to about 200km. 3-D shear-wave velocities are converted to densities using Nafe-Drake relation (Ludwig et al., 1970). To constrain the density data, the gravity anomalies were computed by defining the density contrast between multi-layered models. The computed anomalies are compared with observed Bougher anomalies (Barzaghi et al., 2002). The results are shown in figure 6.3a and 6.3b. Figure 6.3 shows that shear-wave velocities and the converted densities delineate the distinct geometrical features quite well. The calculated negative Bougher anomalies from the density data depict a relatively deeper Moho reaching 45 km depth in the central and northern Apennines close to the coastline of the Adriatic Sea and a shallow Moho in the southern Adriatic Sea. The concordance between the observed and predicted gravity anomalies provides a good confidence into the converted density data from shear- wave velocities. We fix the density data and develop a finite element model space with the size of 1050 km x 1050 km x 300 km, and divided it into three layers (i.e. elastic crust, lithosphere and asthenosphere) as revealed by the ambient noise study. These three layers are filled with Maxwell viscous materials with viscosity of elastic crust as 1.0e+23 Pas, a lithosphere within the range 3.0-7.0e+21Pas and an asthenosphere as 1.0e+20Pas.The choice of viscosity values used in our model is based on previous studies (Aoudia et al., 2007; Ismail-Zadeh et al., 2010;Metois et al., 2015). The Maxwell relaxation time of the lithosphere varies from 3000 to 8000 years depending of the viscosity of the lithospheric lid. We employ Dirichlet boundary conditions(that is, no motion across the boundary planes, but free boundary parallel slip) on the sides and bottom and top of the model domain.We use a 3D dimensional mesh with hexahedral elements with horizontal spacing of 21km and 5 km along depth (see fig. 6.2). We test different models with varying the viscosity of the lithosphere and asthenosphere and also introducing a low viscosity lower crust. We also did some sensitivity test for the initial stresses used for overburden pressure.

6.4 Results and Discussion

We run several simulations using 80 processors of a parallel computer. We assume the viscosity of 5.0e+21 Pas for the lithosphere. Figure 6.4 shows the time evolution of the flow field at 5km depth.

We only show the numerical results within a study region. The flow is mainly driven by buoyancy forces due to density contrast between thick lithosphere beneath Adriatic Sea and the underlying asthenosphere. The flow field indicates that the upper crust moves from southwest to northeast with a maximum velocity reaching 3-5 mm/year after a relaxation of the lithosphere as shown in figure 6.4c. This is in agreement with the result of Ismail-Zadeh et al. (2010). The simulation result does not change much by varying the viscosity of the lithosphere. For example, when using 3.0e+21 Pas as the viscosity of the lithosphere, the flow field reaches similar maximum horizontal velocity of the order of 3-5mm/year after 3200 years, indicating that density contrast between lithosphere and asthenosphere drives the flow field. We compare the predicted flow field with the regional observed GPS velocity field (Metois et al., 2015). We find that the model predicts fairly well the geodetic observations. The results are shown in figure 6.5. The geodetic data and model results are in very good agreement in Central Apennines and in southeastern Alps, suggesting the present day deformation in these regions are controlled by the thick lithosphere beneath the Adriatic Sea. It is also worth to mention that the poorly modeled displacement field close to the boundary of the study region could be the result of boundary effects or also related to N-S Africa and Eurasia convergence. Figure 6.6 shows the cross sections of the flow field across and along the Adriatic Sea. The cross section AB depicts the horizontal eastward flow field movement of Adria microplate, while the cross section CD along the Adriatic Sea clearly illustrates the northward movement of Adria microplate beneath the Southern Alps. Both cross sections show the sinking of the lithosphere beneath the Adriatic Sea, also evident in the work by Ismail-Zadeh et al. (2010). Cross section EF depicts that Central Apennines is moving from Southeast to Northwest direction and Northern Apennines is pushing towards the Southern Alps, which is opposite to the flow predicted by the Ismail-Zadeh et al. (2010). The geodetic surface deformation (i.e. black arrow, see fig. 6.5) also depicts the rotation of velocity field towards the Southern Alps.

Therefore, our 3-D numerical model, accounting only for buoyancy forces, does predict the major kinematic features of the Adria microplate and surrounding belts (See Figs 6.5 and 6.6).We then evaluate the effect of relatively shallow density heterogeneities up to 50km depth as well as a deep interaction between lithosphere and asthenospshere on the modelled flow field. Assuming the same constant density for both lithosphere and asthenosphere, with no contrast, we calculate the

flow field due to density heterogeneities from the surface to 50 km depth. This clearly depicts a poor correlation between observed and predicted geodetic deformation field and also in terms of flow direction and pattern (see Fig. 6.7). On the other hand, a density contrast of the order of 50kgm^{-3} between lithosphere and asthenosphere predicts the geodetic surface deformation very well (see Fig. 6.8), suggesting that thick lithosphere beneath the Adriatic Sea controls the kinematic of the Adria microplate and surrounding belts. It is also worth to mention that we assume several simplifications in our model. For example, we assume a same viscosity for the whole lithosphere and asthenosphere, but in reality viscosity could be varying due to presence of water or melt (Mei et al., 2002). Similarly, we assume constant density contrast between lithosphere and astnenosphere over the whole region, which significantly affect the magnitude of flow filed at the surface. Despite the uncertainties and model limitation related to density inversions, to effective viscosity estimates and to the lithosphere structure, the overall results are similar. We have shown that buoyancy forces, which result from the simple model of density contrast between the lithosphere and asthenospshere, can explain the major features of the present day deformation. Therefore, we can conclude that buoyancy driven mantle convection plays a major role in defining the current surface deformation (e.g. extension in the central Apennine, contraction in the southeastern Alps and subsidence of Adriatic Sea) in the region rather than gravitational potential energy differences within the crust.

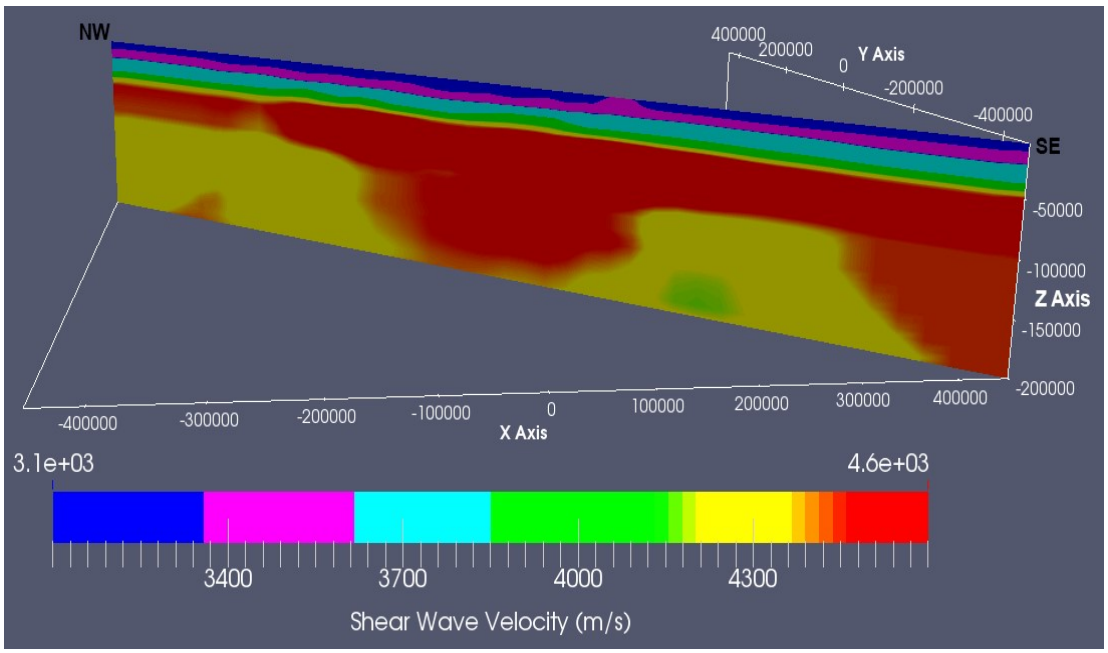

Figure 6.1: Shear-wave velocity model along the Adriatic Sea (Line CD, See Fig. 6.5), computed by Kherchouche (2017).This shows a thick lithosphere beneath the central Adriatic Sea that extends up to 180km in depth.

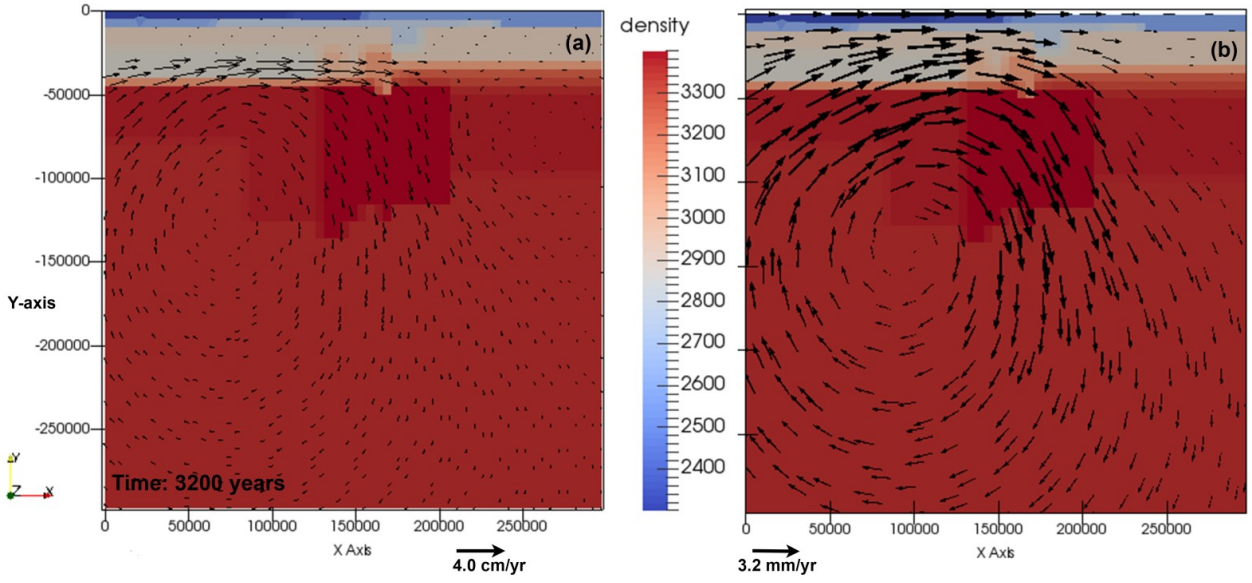

Figure 6.2: Density model and snap shot of the flow field at 3200 years after the full relaxation of lithospheric lid, considering the a) viscosity values from Aoudia et al. (2007), and b) simple 2-layer visocsity model.

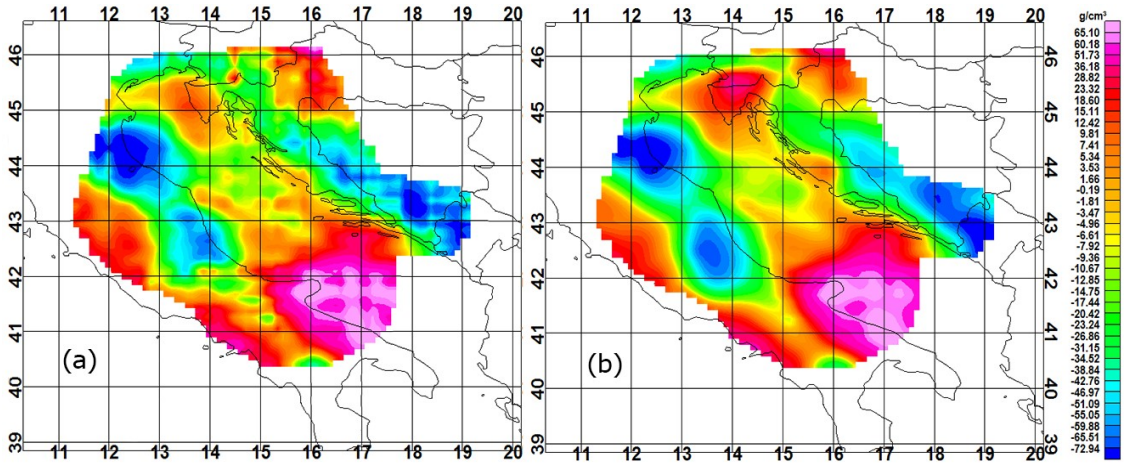

Figure 6.3: a) observed Bougher anomalies and b) calculated bougher anomalies from the converted density data.

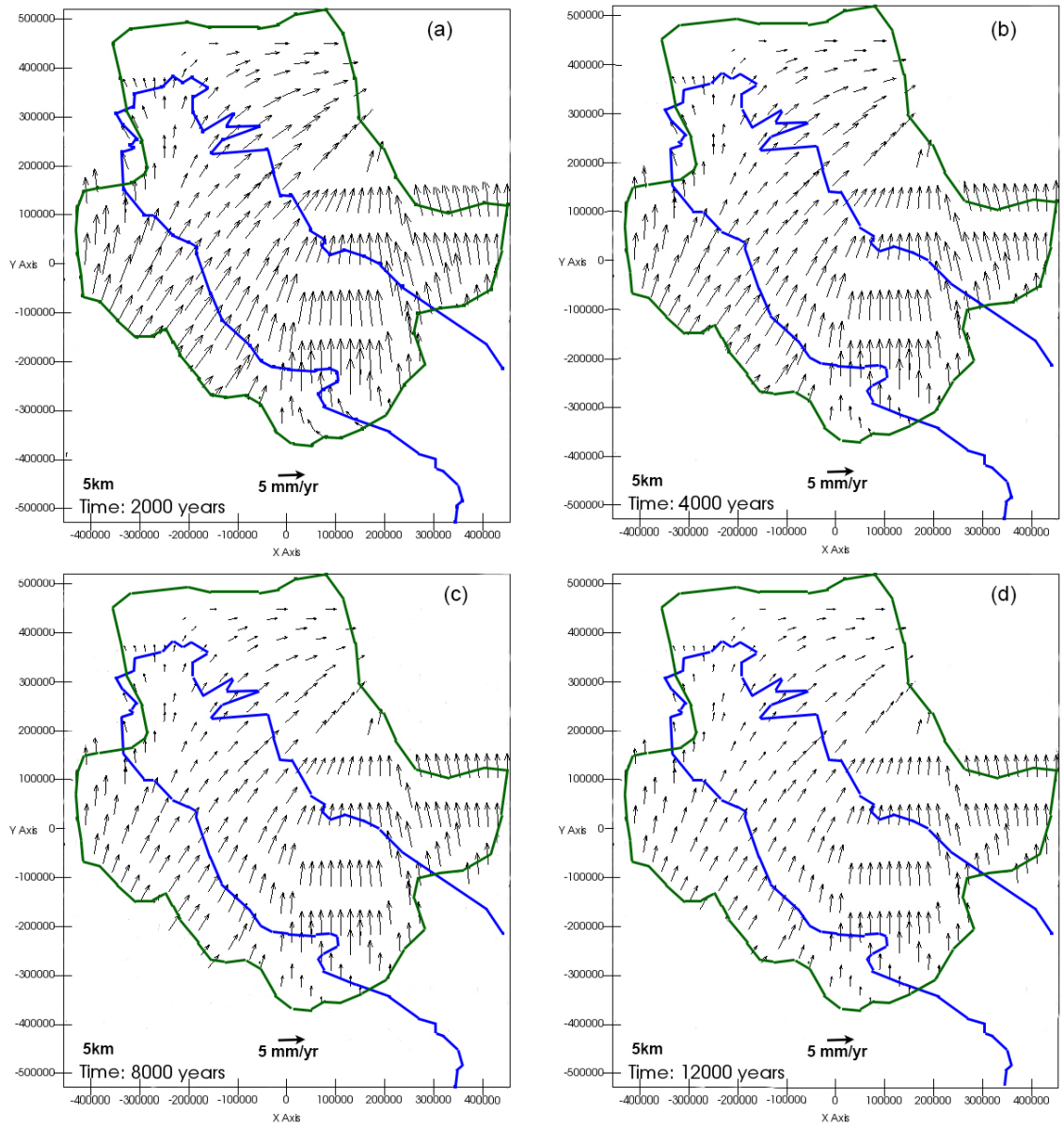

Figure 6.4: Snap shot of flow field at 5km depth after different relaxation times: a) 2000 years, b) 4000 years, c) 8000 years, and d) 12000 years. Green and blue polygons show the boundary of the study area (as resolved by the ambient noise tomography of Kerchouche (2017) and Adriatic Sea respectively.

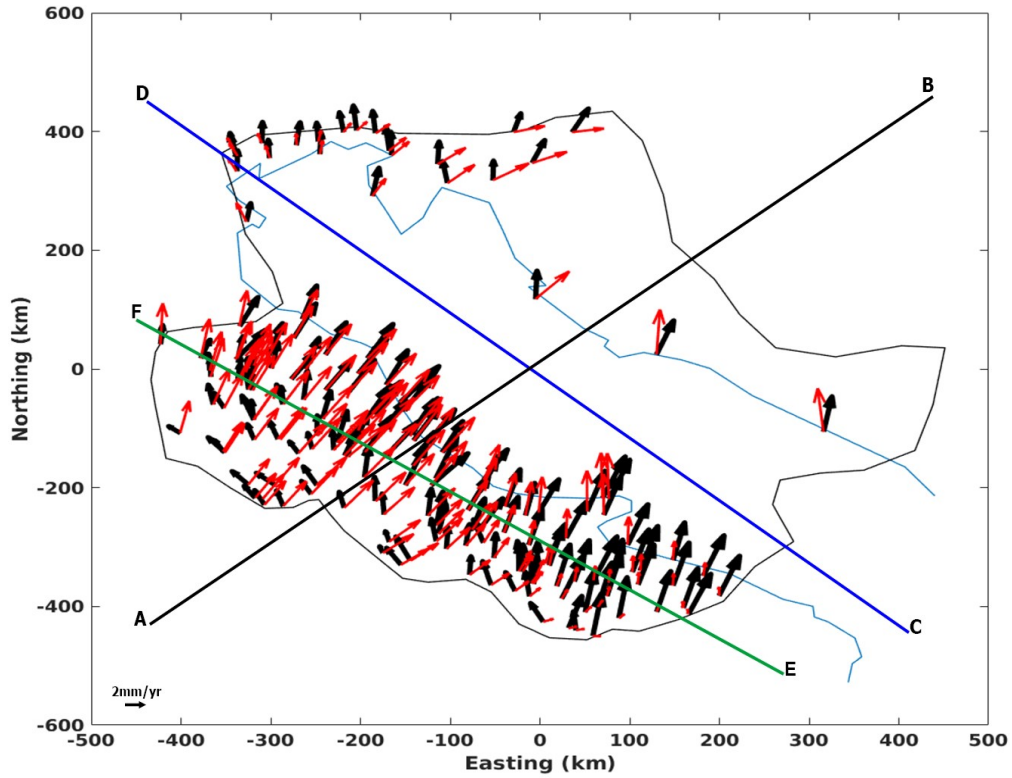

Figure 6.5: Black and red arrows show the observed GPS and predicted displacement field respectively. Light blue curve denotes the boundary of Adriatic Sea and black curve denotes the boundary of study region. Line CD and AB are the cross-sections along and across the Adriatic Sea. Line EF is the cross section along the Apennines. The model fails to predict the GPS sites along the western part of the Italian Peninsula as these are mainly affected by the Africa-Eurasia motion (Metois et al., 2015).

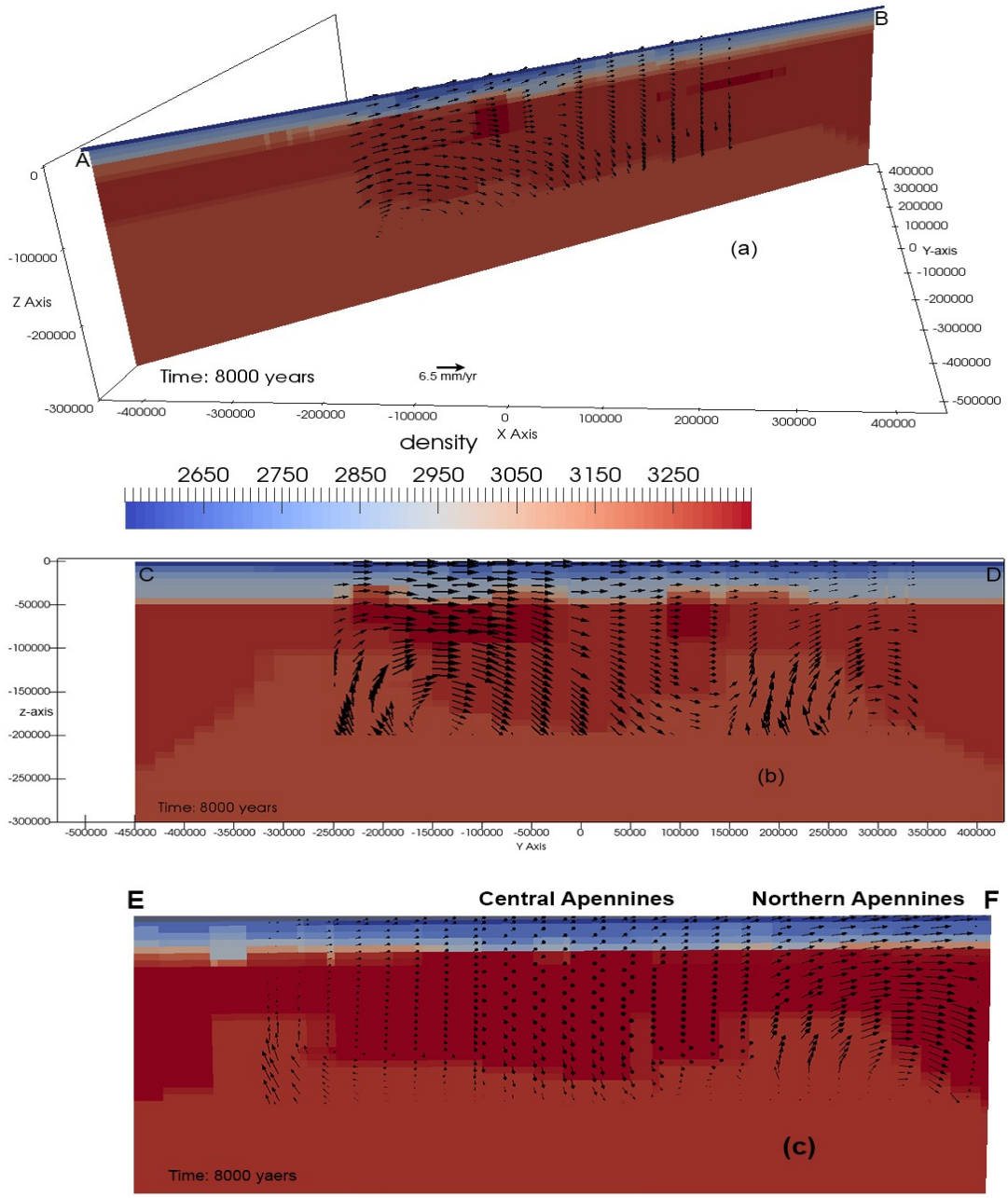

Figure 6.6: Cross Sections AB, CD and EF depict the flow field due to density contrast between lithosphere and asthenosphere crossing a) Apennines, Adriatic Sea and Dinarides, b) Apennines, and c) Adriatic Sea. The positions of the cross sections are shown in figure 6.5.

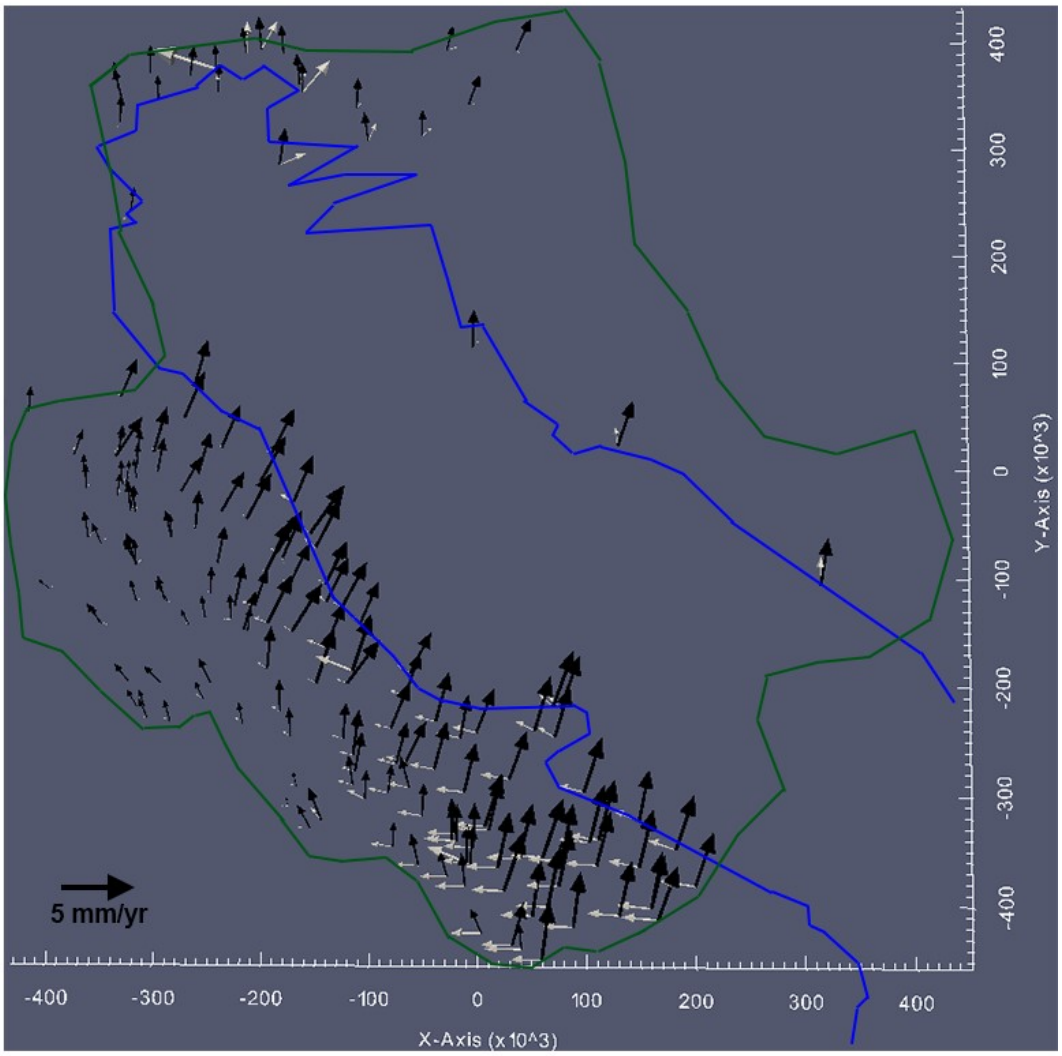

Figure 6.7: Snap shot of the predicted geodetic velocity field due to density variation up to 50 km depth after the relaxation of lithosphere. We assume the same constant density for both lithosphere and asthenosphere. Black and white arrows show the observed GPS and predicted geodetic velocity field respectively. Light blue curve denotes the boundary of Adriatic Sea and green curve denotes the boundary of study region.

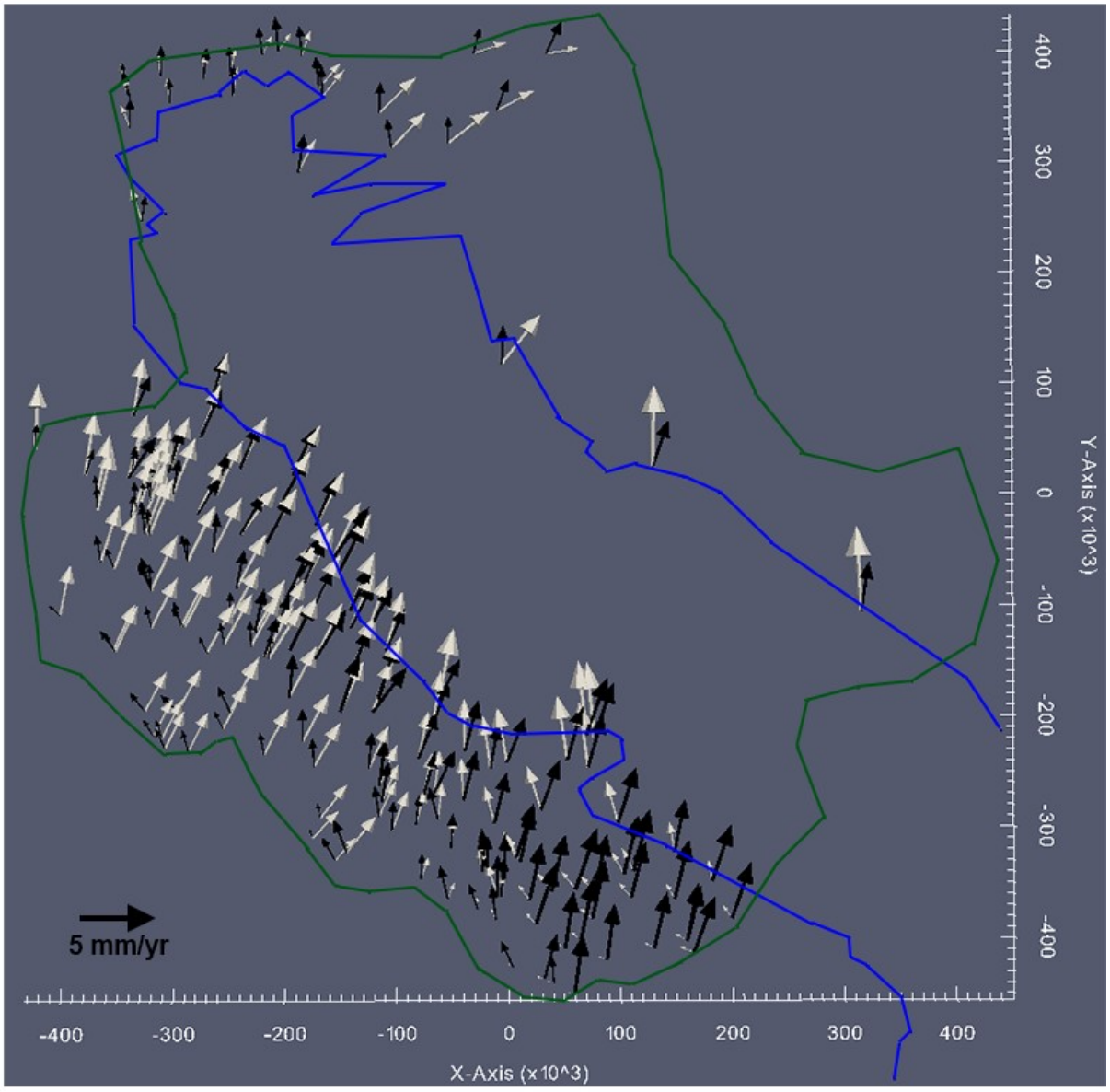

Figure 6.8: Snap shot of the predicted geodetic velocity field due to density contrast of the order of 50kg/m^3 between lithosphere and asthenosphere after the relaxation of lithosphere. We assume a constant density ~2700kg/m^3 up to 50km depth, 3300 kg/m^3 for lithosphere, and 3250 kg/m^3 for asthenospshere. Black and white arrows show the observed GPS and predicted geodetic velocity field respectively. Light blue curve denotes the boundary of Adriatic Sea and green curve denotes the boundary of study region.

References:

1. Aagaard, B. T., M. G. Knepley, and C. A.Williams (2013). A domain decomposition approach to implementingfault slip in finite-element models of quasi-static and dynamic crustal deformation, Journal of GeophysicalResearch: Solid Earth, 118, doi: 10.1002/jgrb.50217.
2. Aagaard, B.T, M.G. Knepley, C. Williams (2016), PyLith User Manual, Version 2.1.4. Davis, CA: Computational Infrastructure of Geodynamics. URL: geodynamics.org/cig/software/pylith/pylith_manual-2.1.4.pdf.
3. Anderson H.A., Jackson J.A. Active tectonics of the Adriatic region. Geophys J R Astron Soc1987a; 91:937-983.
4. Andrews, D. (1976), Rupture velocity of plane strain shear cracks, J. Geophys. Res., 81(32), 5679–5687.
5. Anzidei, M. et al., 2009. Coseismic deformation of the destructive April 6, 2009 L'Aquila earthquake (central Italy) from GPS data, Geophys. Res. Lett., 36, L17307, doi:10.1029/2009GL039145.
6. Aoudia, A., Active faulting and seismological studies for earthquake hazard assessment, Ph.D. thesis, 153 pp., Univ. of Trieste, October 1998.
7. Aoudia, A., Ismail-Zadeh, A.T., Romanelli, F., 2007. Buoyancy-driven deformation and contemporary tectonic stress in the lithosphere beneath Central Italy. Terra Nova19, 490–495.
8. Aoudia, A., Sarao, A., Bukchin, B., Suhadolc, P., 2000. The 1976 Friuli (NE Italy) thrust faulting earthquake: a reappraisal 23 years later. Geophys. Res. Lett. 27 (4), 573–576.
9. Aoyama, H., M. Takeo, and S. Ide (2002), Evolution mechanisms of an earthquake swarm under the Hida Mountains, central Japan, in 1998, J. Geophys. Res., 107(B8), 2174, doi:10.1029/2001JB000540.

10. Avouac, J. P., Ayoub, F., Leprince, S., Konca, O. And Helmberger, D. V. (2006), The 2005, Mw 7.6 Kashmir earthquake: sub-pixel correlation of ASTER images and seismic waveforms analysis, Earth Planet. Sci. Lett., 249, 514–528, doi:10.1016/j.epsl.2006.06.025.
11. Barzaghi, R., Betti, B., Borghi, A., Sona, G., Tornatore, V., 2002. The Italian quasi-geoidITALGEO99. Bollettino di Geodesia e Scienze Affini 1, 33–51.
12. Bajc, J., Aoudia, A., Sarao, A., Suhadolc, P., 2001. The 1998 Bovec–Krn mountain (Slovenia) earthquake sequence. Geophys. Res. Lett. 28 (9), 1839–1842.
13. Barbot, S., and Y. Fialko, Fourier-domain Green's function for an elastic semi-infinite solid under gravity, with applications to earthquake and volcano deformation, Geophys. J. Int., 182(2), 568–582, doi:10.1111/j.1365- 246X.2010.04655.x, 2010a.
14. Barbot, S., and Y. Fialko, A unified continuum representation of postseismic relaxation mechanisms: semianalytic models of afterslip, poroelastic rebound and viscoelastic flow, Geophys. J. Int., 182(3), 1124–1140, doi:10.1111/j.1365-246X.2010.04678.x, 2010b.
15. Barbot, S., Y. Fialko, and Y. Bock, Postseismic Deformation due to the Mw 6.0 2004 Parkfield Earthquake: Stress-Driven Creep on a Fault with Spatially Variable Rate-and-State Friction Parameters, J. Geophys. Res., 114(B07405), doi: 10.1029/2008JB005748, 2009a.
16. Barbot, S., Y. Fialko, and D. Sandwell, Three-Dimensional Models of Elasto-Static Deformation in Heterogeneous Media, with Applications to the Eastern California Shear Zone, Geophys. J. Int., 179(1), 500–520, 2009b.
17. Benedetti, L., P. Tapponnier, G. C. P. King, B. Meyer, and I. Manighetti (2000), Growth folding and active thrusting in the Montello region, Veneto, northern Italy, *J. Geophys. Res.*, 105(B1), 739–766.
18. Bennett, R. A., et al. (2012), Syn-convergent extension observed using the RETREAT GPS network, Northern Apennines Italy, J. Geophys. Res., 117, B04408, doi:10.1029/2011JB008744.
19. Benoit, M. H., M. Torpey, K. Liszewski, V. Levin, and J. Park (2011), P and S wave upper mantle seismic velocity structure beneath the northern Apennines: New evidence for the

end of subduction, *Geochem. Geophys. Geosyst.*, 12, Q06004, doi:10.1029/2010GC003428.

20. Biggs, J., T. Wright, Z. Lu, et al. (2007), Multi-interferogram method for measuring inter-seismic deformation: Denali Fault, Alaska, Geophys. J. Int., 170, 1165–1179.
21. Borghi, A., Aoudia, A., Riva, R.E.M., Barzaghi, R., 2009. GPS monitoring andearthquake prediction: a success story towards a useful integration. Tectonophysics 465 (1–4), 177–189.
22. Bouchon, M., Karabulut, H., Aktar, M., Ozalaybey, S., Schmittbuhl, J. & Bouin, M.P., 2001. Extended nucleation of the 1999 Mw 7.6 Izmit earthquake, Science 331, 877. doi:10.1126/science.1197341.
23. Bouchon, M., Karabulut, H., Aktar, M., Ozalaybey, S., Schmittbuhl, J. & Bouin, M.P., 2011. Extended nucleation of the 1999 Mw 7.6 Izmit earthquake, Science, 331, 877–880.
24. Bouchon, M., Durand, V., Marsan, D., Karabulut, H. & Schmittbuhl, J., 2013. The long precursory phase of most large interplate earthquakes, Nature Geoscience 6, 299-302. doi:10.1038/ngeo1770
25. Brodsky, E.E. & Lay, T., 2014. Recognizing Foreshocks from the 1 April 2014 Chile Earthquake, Science 344, 700. doi:10.1126/science.1255202.
26. Burrato, P., M. E. Poli, P. Vannoli, A. Zanferrari, R. Basili, and F. Galadini (2008), Sources of Mw 5+ earthquakes in northeastern Italy and western Slovenia: An up dated view based on geological and seismological evidence, Tectonophysics, 453(1-4),157–176.
27. Camassi, R., Caracciolo, C.H., Castelli, V. et al., The 1511 Eastern Alps earthquakes: a critical update and comparison of existing macroseismic datasets,J Seismol (2011) 15: 191. doi:10.1007/s10950-010-9220-9.
28. Catalli, F., Cocco, M., Console, R. And Chiaraluce, L. (2008), Modeling seismicity rate changes during the 1997 UmbriaMarche sequence (central Italy) through rate and state dependent model, J. Geophys. Res., 113, B11301, doi:10.1029/ 2007JB005356
29. Cattania, C., S. Hainzl, L.Wang, F. Roth, and B. Enescu (2014), Propagation of Coulomb stress uncertainties in physics-based aftershock models, J. Geophys. Res. Solid Earth, 119, 7846–7864. doi:10.1002/2014JB011183.

30. Cattania, C., S. Hainzl, L. Wang, B. Enescu, And F. Roth (2015), Aftershock triggering by postseismic stresses: a study based on Coulomb rate-and-state models, J. Geophys. Res. Solid Earth, 120, 2388–2407, doi:10.1002/2014JB011500.
31. Cheloni, D., N. D'Agostino, and G. Selvaggi (2014), Interseismic coupling, seismic potential, and earthquake recurrence on the southern front of the Eastern Alps (NE Italy), Journal of Geophysical Research: Solid Earth, 119(5), 4448–4468, doi:10.1002/2014JB010954.
32. Chen, X., & Shearer, P.M., 2013. California foreshock sequences suggest aseismic triggering process, Geophys. Res. Lett., 40, doi:10.1002/grl.50444.
33. Chiaraluce, L., et al. (2004), Complex normal faulting in the Apennines thrust-and-fold belt: The 1997 seismic sequence in central Italy, Bull. Seismol. Soc. Am., 94(1), 99 – 116.
34. Chiaraluce, L., 2012. Unravelling the complexity of Apenninic extensional fault systems: a review of the 2009 L'Aquila earthquake (Central Apennines, Italy), J. Struct. Geol. 42, 2–18, doi:10.1016/j.jsg.2012.06.007.
35. Chiaraluce L., Valoroso L., Piccinini D., Di Stefano R., De Gori P.The anatomy of the 2009 L'Aquila normal fault system (central Italy) imaged by high resolution foreshock and aftershock locations. J. geophys. Res. 2011;116. doi:10.1029/2011JB008352.
36. Cirella, A., Piatanesi, A., Cocco, M., Tinti, E., Scognamiglio, L., Michelini, A., Lomax, A. & Boschi, E., 2009. Rupture history of the 2009 L'Aquila (Italy) earthquake from non-linear joint inversion of strong motion and GPSdata,Geophys.Res.Lett.,36,L19304,doi:10.1029/2009GL039795.
37. Cocco, M., Hainzl, S., Catalli, F., Enescu, B., Lombardi, A. M. and Woessner, J. (2010), Sensitivity study of forecasted aftershock seismicity based on Coulomb stress calculation and rateand state-dependent frictional response, J. Geophys. Res., 115, B05307, doi:10.1029/2009JB006838.
38. D'Agostino, N. & McKenzie, D.P., 1999. Convective support of longwavelength topography in the Apennines (Italy), Terranova, 11(5), 234–238.
39. D'Agostino, R., Giuliani, R., Mattone, M. & Bonci, L., 2001. Active crustal extension in the central Apennines (Italy) inferred from GPS measurements in the interval 1994–1999,

Geophys. Res. Lett., 28, 2121–2124.

40. D'Agostino, N., D. Cheloni, S. Mantenuto, G. Selvaggi, A. Michelini, and D. Zuliani (2005), Strain accumulation in the southern Alps (NE Italy) and deformation at the northeastern boundary of Adria observed by CGPS, *Geophys. Res. Lett.*, 32, L19306, doi:10.1029/2005GL024266.
41. D'Agostino, N., A. Avallone, D. Cheloni, E. D'Anastasio, S. Mantenuto, and G. Selvaggi (2008), Active tectonics of the Adriatic region from GPS and earthquake slip vectors, Journal of Geophysical Research (Solid Earth), 113(B12), B12413, doi: 10.1029/2008JB005860.
42. D'Agostino, N., et al. (2011), Evidence for localized active extension in the central Apennines (Italy) from global positioning system observations, Geology, 39, 291–294, doi:10.1130/G31796.1.
43. D'Agostino, N., Cheloni, D., Fornaro, G., Giuliani, R. & Reale, D., 2012. Space-time distribution of afterslip following the 2009 L'Aquila earthquake, J. geophys. Res., 117, B02402, doi:10.1029/2011JB008523.
44. Day, S. M. (1982), Three-dimensional simulation of spontaneous rupture: The effect of nonuniform prestress, Bull. Seismol. Soc. Am., 72(6A), 1881–1902.
45. Daley, D. J. and Vere-Jones, D. (2003), An Introduction to the Theory of Point Processes, Vol. I: Elementary Theory and Methods, 2nd ed., Springer, New York.
46. DeVries, P. M. R., P. G. Krastev, and B. J. Meade (2016), Geodetically constrained models of viscoelastic stress transfer and earthquake triggering along the North Anatolian fault, Geochem. Geophys. Geosyst., 17, 2700–2716, doi:10.1002/2016GC006313.
47. Dieterich, J. A constitutive law for rate of earthquake production and its application to earthquake clustering. J. Geophys. Res.99, 2601−2618 (1994).
48. Dieterich, J. H., Cayol, V. and Okubo, P. (2000), The use of earthquake ratechanges as a stress meter at Kilauea volcano, Nature, 408, 457–460.
49. Duan, B., and D. D. Oglesby (2005), Multicycle dynamics of nonplanar strike-slip faults, Journal of Geophysical Research,110(B12), B03304, doi:10.1029/2004JB003298.
50. Dewey J.F., Helman M.L., Turco E., Hutton D.H.W., Knott S.D. "Kinematics of the western

Mediterranean." In Alpine Tectonics, M. P. Coward, D. Dietrich, R. G. Park eds.,Geological Society Special Publication, 45:265-284, 1989.

51. Felzer, K. R., Abercrombie, R. E. And Ekstrom, G. (2003), Secondary aftershocks and their importance for aftershock forecasting, Bull. Seismol. Soc. Am., 93(4), 1433–1448.
52. Fialko, Y., D. Sandwell, D. Agnew, M. Simons, P. Shearer, and B. Minster (2002), Deformation on nearby faults induced by the 1999 Hector Mine earthquake, Science, 297, 1858–1862, doi:10.1126/science.1074671.
53. Fialko, Y. (2006), Interseismic strain accumulation and the earthquake potential on the southern San Andreas Fault system, Nature, 441,968–971, doi:10.1038/nature04797.
54. Fitzko, F., Suhadolc, P., Aoudia, A., Panza, G.F., 2005. Constraints on the location and mechanism of the 1511 Western-Slovenia earthquake from active tectonics and modeling of macroseismic data. Tectonophysics 404, 77.
55. Freed, A. M. & Lin, J. Delayed triggering of the 1999 Hector Mine earthquake by viscoelastic stress transfer. Nature411, 180−183 (2001).
56. Foroutan, M., Aoudia, A. (2017), New evidence of a surface displacement on the Rasa fault from the LIDAR data. (manuscript in preparation).
57. Ganas, A., Gosar, A., and Drakatos, G.: Static stress changes due to the 1998 and 2004 Krn Mountain (Slovenia) earthquakes and implications for future seismicity, Nat. Hazards Earth Syst. Sci., 8, 59-66, doi:10.5194/nhess-8-59-2008, 2008.
58. Gardner, J. K., And Knopoff, L. (1974), Is the sequence of earthquakes in Southern California, with aftershocks removed, Poissonian?, Bull. Seismol. Soc. Am., 64(5), 1363–1367.
59. Gosar A, Šebela S, Košťák B, Stemberk J (2011) On the state of the TM 71 extensometer monitoring in Slovenia: seven years of micro-tectonic displacement measurements. Acta Geodyn Geomater 8(4):389–402.
60. Gualandi, A., Serpelloni, E. & Belardinelli, M.E., 2014. Space–time evolution of crustal deformation related to the Mw 6.3, 2009 L'Aquila earthquake (central Italy) from principal component analysis inversion of GPS position time-series, Geophys. J. Int., 197(1), 174–191.

61. Hainzl, S., Enescu, B., Cocco, M., Woessner, J., Catalli, F., Wang, R. and Roth, F. (2009), Aftershock modeling based on uncertain stress calculations,J. Geophys.Res., 114, B05309, doi: 10.1029/2008JB006011, 2009.
62. Hainzl, S., Steacy, S. And Marsan, D. (2010), Seismicity models based on Coulomb stress calculations, Community Online Resource for Statistical Seismicity Analysis, doi:10.5078/corssa32035809.
63. Hardebeck, J. L. And Hauksson, E. (2001), Crustal stress field in southern California and its implications for fault mechanisms, J. Geophys. Res., 106 (B10), 21, 859–821, 882.
64. Harris, R. A. And Simpson, R. W. (1992), Changes in static stress on southern California faults after the 1992 landers earthquake. Nature, 360, 251–254
65. Harris, R. A., Simpson, R. W. & Reasenberg, P. A. Influence of static stress changes on earthquake locations in southern California. Nature375, 221−224 (1995).
66. Harris, R. A. (1998), Introduction to special section: stress triggers, stressshadows, and implication for seismic hazard. J. Geophys. Res., 103, 24 347-24, 358.
67. Harris, R. & Segall, P. 1987. Detection of a locked zone at depth on the Parkfield, California segment of the San Andreas fault, J. Geophys. Res., 92, 7945–7962.
68. Hartzell, S., Pengcheng, L., Mendoza, C., Chen, J., and Larson, K.M. (2007), Stability and uncertainty of finite-fault slip inversions: Application to the 2004 Parkfield, California, earthquake, Bull. Seismol. Soc. Am., 97, 1911–1934.
69. Hauksson, E. Crustal structure and seismicity distribution adjacent to the Pacific and North America plate boundary in southern California. J. Geophys. Res. 105, 13875–-13903 (2000).
70. Helmstetter, A. and Shaw, B. E. (2006), Relation between stress heterogeneity and aftershock rate in the rate-and-state model, J. Geophys. Res., 111, B07304, doi:10.1029/2005JB004077.
71. ICEF, Annals of Geophysics, 54, 4 (2011), doi:10.4401/ag-5350
72. Jackson, J. Living with earthquakes: know your faults. Journal of Earthquake Engineering , 5, Special Issue 1, 5-123 (2001).

73. Jonsson, S., Zebker, H., Segall, P. & Amelung, F., 2002. Fault slip distribution of the 1999 MW 7.1 Hector Mine earthquake, California, estimated from satellite radar and GPS measurements, Bull. seism. Soc. Am., 92,1377–1389.
74. Jouanne, F., Awan, A., Madji, A., PeCher, A., Latif, M., Kausar, A., Mugnier, J. L., Khan, I. And Khan, N. A. (2011), Postseismic deformation in Pakistan after the 8th October 2005 earthquake: Evidence of afterslip along a flat north of the Balakot-Bagh thrust, J. Geophys. Res., 116, B07401, 22 pp. doi:10.1029/ 2010JB007903.
75. Kagan, Y. Y. (2004), Short-term properties of earthquake catalogs and models of earthquake source, Bull. Seismol. Soc. Am., 94 (4), 1207–1228.
76. Kato, A., Igarashi, T., Tsuruoka, H., Nakagawa, S. & Hirata, N., 2012. Propagation of Slow Slip Leading Up to the 2011 Mw 9.0 Tohoku-Oki Earthquake, *Science* 335, 705. doi:10.1126/science.1215141.
77. Kerchouche, R. (2017), High resolution ambient noise tomography of central Mediterranean region, PhD thesis.
78. King, G. C. P., Stein, R. S. And Lin, J. (1992), Change in failure stress on the southern San Andreas fault system caused by the 1992 magnitude = 7.4 Landers earthquake. Science, 258, 1328–1332
79. King, G. C. P., and M. Cocco (2001), Fault interaction by elastic stress changes: New clues from earthquake sequences, Adv . Geophys., 44,1–38.
80. King, G. C., R. S. Stein, and J. Lin (1994), Static stress changes and the triggering of earthquakes, Bull. Seismol. Soc. Am., 84(3), 935–953.
81. Lin, J. & Stein,R.S., 2004. Stress triggering in thrust and subduction earthquakes and stress interaction between the southern San Andreas and nearby thrust and strike-slip faults, J. Geophys. Res. 109, B02303. doi:10.1029/2003JB002607.
82. Lindsey, E. O., and Y. Fialko (2013), Geodetic slip rates in the southern San Andreas Fault system: Effects of elastic heterogeneity and fault geometry, J. Geophys. Res. Solid Earth, 118, 689–697, doi:10.1029/2012JB009358.
83. Le Pichon, X., Kreemer, C. & Chamot-Rooke, N. Asymmetry in elasticproperties and the evolution of large continental strike-slip faults. J. Geophys.Res. 110, B03405,

doi:10.1029/2004JB003343 (2005).

84. Lorenzo-Mart_ın, F., F. Roth, and R. Wang (2006), Elastic and inelastic triggering of earthquakes in the North Anatolian fault zone, Tectonophysics,424(3), 271–289.
85. Lucente F.P., De Gori P., Margheriti L., Piccinini D., Di Bona M., Chiarabba C., Agostinetti N.P.Temporal variation of seismic velocity and anisotropy before the 2009 M_w 6.3 L'Aquila earthquake, Italy. Geology 2010;38:1015-1018.
86. Ludwig, W.J., Nafe, J.E., Drake, C.L., 1970. Seismic refraction. In: Maxwell, A.E. (Ed.), NewConcepts of Sea Floor Evolution. Wiley-Interscience, New York, pp. 53–84.
87. Mallman, E. P. and Zoback, M. D. (2007), Assessing elastic Coulomb stress transfer models using seismicity rates in southern California and southwestern Japan, J. Geophys. Res., 112, B03304, doi:10.1029/2005JB004076.
88. Marsan, D. (2006), Can coseismic stress variability suppress seismicity shadows? Insights from a rate-and-state friction model, J. Geophys. Res., 111, B06305, doi:10.1029/2005JB004060.
89. McGarr, A. (1988), On the State of Lithospheric Stress in the Absence of Applied Tectonic Forces, J. Geophys. Res., 93(B11), 13609–13617, doi:10.1029/JB093iB11p13609.
90. Mei, S., Bai, W., Hiraga, T., Kohlstedt, D.L., 2002. Influence of melt on the creep behavior of olivine-basalt aggregates under hydrous conditions. Earth and Planetary Science Letters 201, 491–507.
91. Metois, M., N. D'Agostino, A. Avallone, N. Chamot-Rooke, A. Rabaute, L. Duni,N. Kuka, R. Koci, and I. Georgiev (2015), Insights on continental collisional processes from GPS data: Dynamics of the peri-Adriatic belts, Journal of Geophysical Research:Solid Earth, 120(12), 8701–8719, doi:10.1002/2015JB012023.
92. Moulin, A., Benedetti, L., Gosar, A., Rupnik, P. J., Rizza, M., Bourlès, D., & Ritz, J. F. (2014). Determining the present-day kinematics of the Idrija fault (Slovenia) from airborne LiDAR topography. Tectonophysics.
93. Moulin, A., et al. (2016), The Dinaric fault system: Large-scale structure, rates of slip, and Plio-Pleistocene evolution of the transpressive northeastern boundary of the Adria microplate, Tectonics, 35, 2258–2292, doi:10.1002/2016TC004188.

94. Nocquet, J.M. and Calais, E., 2004. Geodeticmeasurements of crustal deformation in Western Mediterranean and Europe. Pure Appl. Geophys., 161, 661–681.
95. Nur, A. & Booker, J. R. Aftershocks caused by pore fluid flow? Science175, 885−887 (1972).
96. Ogata, Y. (1998), Space-time point-process models for earthquake occurrences, Ann. Inst. Stat. Math., 50, 379–402.
97. Ogata, Y. (1992), Detection of precursory relative quiescence before great earthquakes through a statistical model, J. Geophys. Res., 97, 19845–19871.
98. Okada, Y., 1985. Surface deformation due to shear and tensile faults in a half-space. Bulletin of the Seismological Society of America, 75, n.4, 1135-1154.
99. Okada, Y., Internal deformation due to shear and tensile faults in a half-space, Bull. Seismol. Soc. Am, 82(2), 1018-1040, 1992.
100. Parsons, T., and D. S. Dreger (2000), Static-stress impact of the 1992 Landers earthquake sequence on nucleation and slip at the site of the 1999 M57.1 Hector Mine earthquake, southern California, Geophys. Res. Lett., 27(13), 1949–1952.
101. Parsons, T., Ogata, Y., Zhuang, J. and Geist, E. L. (2012), Evaluation of static stress change forecasting with prospective and blind tests, Geophys. J. Int., 188, 1425–1440, doi: 10.1111/j.1365-246X.2011.05343.x.
102. Parsons, T., Yeats, R. S., Yagi, Y. and Hussain, A. (2006), Static stress changefrom the 8 October, 2005 M = 7.6 Kashmir earthquake, Geophys. Res. Lett., 33, L06304, doi:10.1029/2005GL025429.
103. Panza, G.F., Peccerillo, A., Aoudia, A., Farina, B., 2007. Geophysical and petrological modeling of the structure and composition of the crust and upper mantle incomplex geodynamic settings: The Tyrrhenian Sea and surroundings. Earth Science Reviews 80, 1–46.
104. Pathier, E., Fielding, E. J., Wright, T. J., Walker, R., Parsons, B. E. And Hensley, S. (2006), Displacement field and slip distribution of the 2005 Kashmir earthquake from SAR imagery, Geophys. Res. Lett., 33, L20310, doi:10.1029/ 2006GL027193.
105. Poljak, M., Gosar, A., Živčić, M., 2010. Active tectonics in Slovenia. GeoActa, Special

Publication, 3, pp. 15–24.

106. Pollitz, F. F., and I. S. Sacks (2002), Stress triggering of the 1999 Hector Mine earthquake by transient deformation following the 1992 Landers earthquake, Bull. Seismol. Soc. Am., 92(4), 1487–1496.

107. Piccardi, L., Gaudemer, Y., Tapponnier, P. & Boccaletti, M., 1999. Active oblique extension in the central Apennines (Italy): evidence from the Fucino region, Geophys. J. Int., 139, 499–530.

108. Reasenberg, P. A. Foreshock occurrence before large earthquakes. J. Geophys. Res.104, 4755–4768 (1999).

109. Reasenberg, P. A., and R. W. Simpson (1992), Response of regional seismicity to the static stress change produced by the Loma Prieta earthquake, Science, 255(5052), 1687–1690.

110. Ribaric V (1979) The Idrija earthquake of March 26, 1511, a reconstruction of some seismological parameters. Tectonophysics 53:315–324.

111. Rice, J. R. And Cleary, M. P. (1976), Some basic stress diffusion solutions for fluid-saturated elastic porous media with compressible constituents, Reviews of Geophysics and Space Physics, 14:227–241.

112. Savage, J.C. and Prescott, W.H. (1978). Asthenosphere readjustment and the earthquake cycle. Journal of Geophysical Research 83: doi: 10.1029/JB083iB07p03369. issn: 0148-0227.

113. Savage, J.C., Prescott, W.H, M. Lisowski, and N. King (1979), Geodolite measurements of deformation near Hollister, California, 1971–1978, J. Geophys. Res., 84(B13), 7599–7615, doi:10.1029/JB084iB13p07599.

114. Segou, M., T. Parsons And W. Ellsworth (2013), Comparative evaluation of combined physics based and statistical forecast models, Journal of Geophysical Research, v. 118, p. 6219–6240, doi:10.1002/2013JB010313.

115. Serpelloni, E., Anzidei, M., Baldi, P., Casula, G., Galvani, A., 2005. Crustal velocity and strain-rate fields in Italy and surrounding regions: new results from the analysis of permanent and non-permanent GPS networks. GJI 161, 861–880.

116. Stein, R. S., A. A. Barka, and J. H. Dieterich (1997), Progressive failure on the North

Anatolian fault since 1939 by earthquake stress triggering,Geophys. J. Int., 128(3), 594–604.

117. Stein, R.S.,The role of stress transfer in earthquake occurrence Nature, 402 (1999), pp. 605–609.

118. Stein, R.S., King, G.C., Lin, J., 1992. Change in failure stress on thesouthern San Andreas fault system caused by the 1992magnitude = 7.4 Landers earthquake. Science 258 (5086),1328–1332.

119. Stein R. S., Lin, J. And King, G. C. P. (1981), Static stress changes and the triggering of earthquakes. Bull. Seismol. Soc. Am., 84:935–953.

120. Stein, R. S. And Lisowski, M. (1983), The 1979 Homestead valley earthquake sequence California: control of aftershocks and postseismic deformation. J. Geophys. Res., 88:6477–6490.

121. Steacy, S., D. Marsan, S. S. Nalbant, and J. McCloskey (2004), Sensitivity of static stress calculations to the earthquake slip distribution, *J. Geophys. Res.*, **109**, B04303, doi:10.1029/2002JB002365.

122. Steacy, S., J. Gomberg, and M. Cocco (2005), Introduction to special section: Stress transfer, earthquake triggering, and time-dependent seismic hazard, J. Geophys. Res., 110, B05S01, doi:10.1029/2005JB003692.

123. Sugan, M., A. Kato, H. Miyake, S. Nakagawa, and A. Vuan (2014), The preparatory phase of the 2009Mw 6.3 L'Aquila earthquake by improving the detection capability of low-magnitude foreshocks, Geophys. Res. Lett., 41, 6137–6144, doi:10.1002/2014GL061199.

124. Stiphout, T., Zhuang, T. And Marsan, J. D. (2010), Seismicity Declustering, Community Online Resource for Statistical Seismicity Analysis, doi:10.3929/ethz-a-xxxxxxxxx.

125. Thatcher, W., and J. B. Rundle (1979), A model for the earthquake cycle in underthrust zones, J. Geophys. Res., 84(B10), 5540–5556, doi:10.1029/JB084iB10p05540.

126. Toda, S., Stein, R.S., Reasenberg, P.A., Dieterich, J.H., Yoshida, A., 1998. Stress transferred by the 1995 M(w)=6.9 Kobe, Japan, shock: effect on aftershocks and future earthquake probabilities. J. Geophys. Res., B Solid Earth 103 (B10), 24543–24565.

127. Toda, S., And Stein, R. S. (2003), Toggling of seismicity by the 1997 Kagoshima earthquake couplet: a demonstration of time dependent stress transfers J. Geophys. Res.,

108(B12), 2567, doi:10.1029/2003JB002527.

128. Toda, S., Stein, R.S., Richards-Dinger, K. & Bozkurt, S., 2005. Forecasting the evolution of seismicity in southern California: Animations built on earthquake stress transfer. J. Geophys. Res. 110, B05S16. doi:10.1029/2004JB003415.

129. Toda, S., Stein, R.S., Sevilgen, V., and Lin, J, Coulomb 3.3 User Guide. URL: http://usgsprojects.org/coulomb/Coulomb33of2011-1060.pdf

130. Valoroso L., Chiaraluce L., Piccinini D., Di Stefano R., Schaff S., Waldhauser F. Radiography of a normal fault system by 64,000 high-precision earthquake locations: the 2009 L'Aquila (central Italy) case study. J. geophys. Res. 2013;118:1156-1176.

131. Vičič, B. (2018), Microseismicity in the Idrija fault system, PhD thesis.

132. Wang, H., and T. J. Wright (2012), Satellite geodetic imaging reveals internal deformation of western Tibet, Geophys. Res. Lett., 39, L07,303, doi:10.1029/2012GL051,222.

133. Wells, D. L., and K. J. Coppersmith (1994), New empirical relationships among magnitude, rupture length, rupture width, rupture area and surface displacement, B. Seismol.Soc. Am., 84(4), 974–1002.

134. Woessner, J., Jonsson, S., Sudhaus, H. And Bachmann, C. (2012), Reliability of Coulomb stress changes inferred from correlated uncertainties of finite-fault source models, J. Geophys. Res., 117, B07303, doi:10.1029/2011JB009121.

135. Wright, T.J, The earthquake deformation cycle A&G (2016) 57 (4): 4.20-4.26 doi:10.1093/astrogeo/atw148.

136. Zeng, Y. (2001), Viscoelastic stress-triggering of the 1999 Hector Mine Earthquake by the 1992 Landers Earthquake, Geophys. Res. Lett.,28(15), 3007–3010.

137. Zhuang, J., Ogata, Y. and Vere-Jones, D. (2002), Stochastic declustering of time earthquake occurrences, J. Am. Stat. Assoc., 97, 369–380.

138. Zhuang, J., Ogata, Y. And Vere-Jones, D. (2004), Analyzing earthquake clustering features by using stochastic reconstruction, J. Geophys. Res., 109, B05301, doi:10.1029/2003JB002879.

139. Utsu, T. A. (1961), Statistical study on the occurrence of aftershocks, Geophys. Mag., 30, 521- 605.

List of Figures and Tables

Acknowledgements

This PhD was supported by the International Centre for Theoretical Physics (ICTP).

I would like to express my special appreciation and thanks to my advisor Dr. Abdelkrim Aoudia, you have been a tremendous mentor for me. I would like to thank you for encouraging my research and for allowing me to grow as a research scientist. Your advice on both research as well as on my career have been priceless. I would also like to thank Professor Alik Ismail-Zadeh and Dr. Alessandro Vuan for carefully reviewing the thesis. Specfically comments and suggestions by the Prof. Alik Ismail-Zadeh improved the thesis.

I had really a great time in ICTP, and I feel so lucky to have had the chance to meet with the eminent visiting researchers, colleagues and friends. I am thankful to ICTP staff for being helpful and patient whenever I struggled with Italian burocracy. During my PhD, I had a chance to collaborate the people outside ICTP. Special Thanks to Dr. Sebastian Hainzl for his valuable suggestions and comments. I am also thankful to Director of Centre for earthquake studies (CES) for giving the permission to persuade the PhD studies at University of Trieste, Italy.

I would also like to thank all of my friends who supported me in writing, and incented me to strive towards my goal. At the end I would like express appreciation to my beloved wife Faryal Arshad who spent sleepless nights with and was always my support in the moments when there was no one to answer my queries. I appreciate my two daughters for abiding my ignorance and the patience they showed during my thesis writing. Words would never say how grateful I am to both of you. I consider myself the luckiest in the world to have such a lovely and caring family, standing beside me with their love and unconditional support.